Scientific Research

International Journal of Communications, Network and System Sciences

ISSN: 1913-3715
Volume 3, Number 5, May 2010

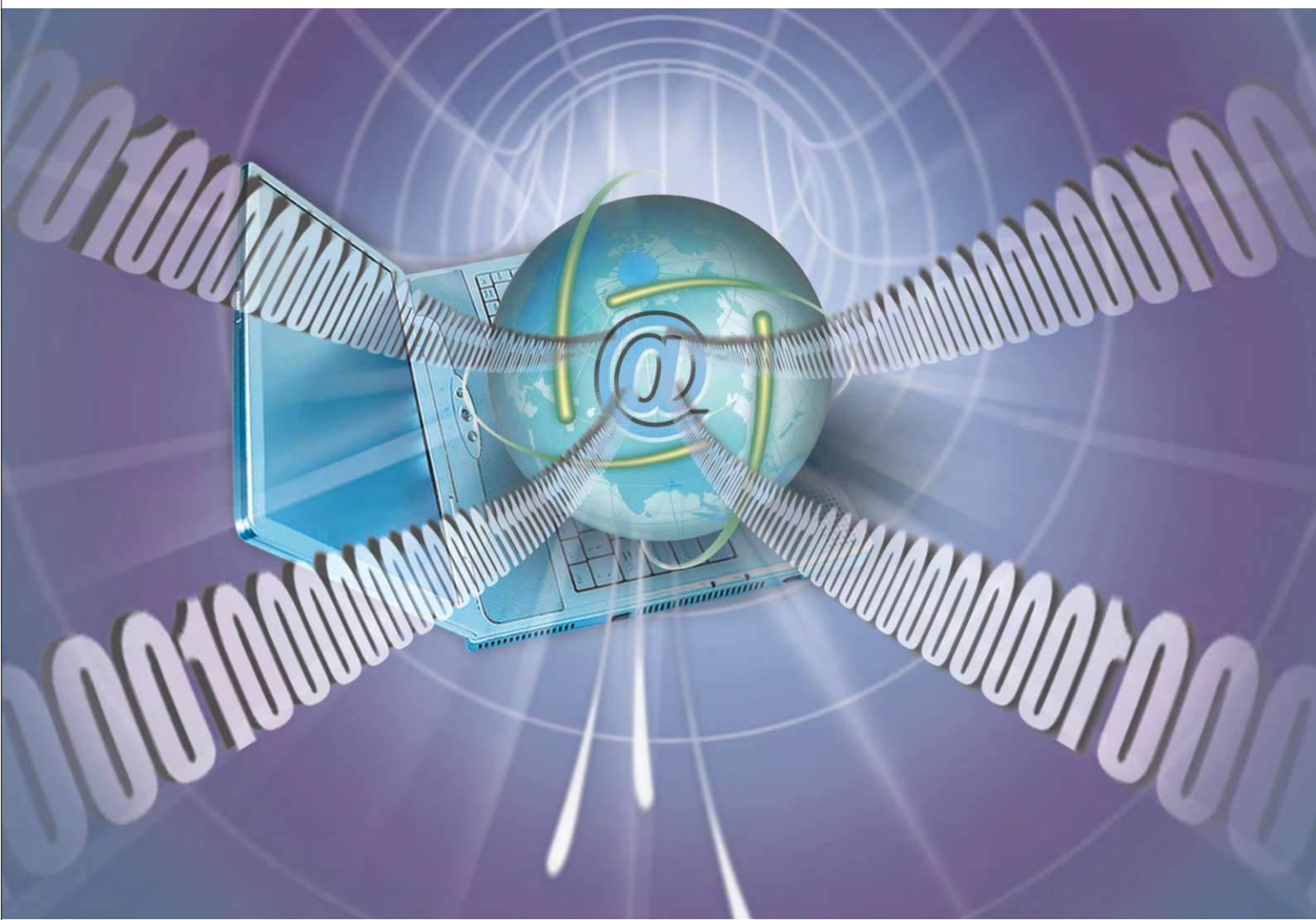

ISSN: 1913-3715
9 771913 371006 05

www.scirp.org/journal/ijcns/

JOURNAL EDITORIAL BOARD

ISSN 1913-3715 (Print) ISSN 1913-3723 (Online)
http://www.scirp.org/journal/ijcns/

Int. J. Communications, Network and System Sciences, **2010, 3, 425-493**
Published Online May 2010 in SciRes (http://www.SciRP.org/journal/ijcns/)

TABLE OF CONTENTS

Volume 3 Number 5 May 2010

International Journal of Communications, Network and System Sciences (IJCNS)

Journal Information

SUBSCRIPTIONS

The *International Journal of Communications, Network and System Sciences (*Online at Scientific Research Publishing, www.SciRP.org) is published monthly by Scientific Research Publishing, Inc., USA.

Subscription rates:

Print: $50 per issue.
To subscribe, please contact Journals Subscriptions Department, E-mail: sub@scirp.org

SERVICES

Advertisements
Advertisement Sales Department, E-mail: service@scirp.org

Reprints (minimum quantity 100 copies)
Reprints Co-ordinator, Scientific Research Publishing, Inc., USA.
E-mail: sub@scirp.org

COPYRIGHT

PRODUCTION INFORMATION

For manuscripts that have been accepted for publication, please contact:
E-mail: ijcns@scirp.org

Int. J. Communications, Network and System Sciences, **2010, 3, 425-429**
doi:10.4236/ijcns.2010.35055 Published Online May 2010 (http://www.SciRP.org/journal/ijcns/)

Scientific Research

A/D Restrictions (Errors) in Ultra-Wideband Impulse Radios

Giorgos Tatsis[1], Constantinos Votis[1], Vasilis Raptis[1], Vasilis Christofilakis[1,2], Panos Kostarakis[1]
[1]*Physics Department, University of Ioannina, Ioannina, Greece*
[2]*Siemens Enterprise Communications, Enterprise Products Development, Athens, Greece*
E-mail: {*gtatsis, kvotis, vraptis*}*@grads.uoi.gr*
basilios.christofilakis@siemens-enterprise.com, kostarakis@uoi.gr
Received February 4, 2010; *revised March* 6, 2010; *accepted April* 20, 2010

Abstract

Ultra-Wideband Impulse Radio (UWB-IR) technologies, although are relatively easy in transmission but they present difficulties in reception, in fact the reception of such waveform is a quite complicated matter. The main reason is that in fully digital receiver the received waveform must be sampled at a rate of several GHz. This paper focuses on the impact of the Analog to Digital (A/D) conversion stage that is used to sample the received waveform. More specifically we focus on the impact of the two main parameters that affect the performance of the Software Defined Radio (SDR) system. These parameters are the bit resolution and the time jittering. The influence of these parameters is deeply examined.

Keywords: UWB, Impulse Radio, ADC, Jitter Error, Quantization Error

1. Introduction

UWB transmission has recently received great attention in academia and industry for applications in wireless communications. A UWB system is defined as any radio system that has a 10 dB fractional bandwidth larger than 20% of its center frequency, or has a 10 dB bandwidth larger than 500 MHz. It is expected that many approaches used for short-range wireless communications will be revaluated and a new industrial sector with high data rate will be formed. Fully digital receiver for UWB-IR requires the use of A/D conversion and SDR techniques as described below. The RF waveform received from the antenna is directly digitized from the antenna via an A/D conversion stage. Then the digital information derived from the UWB waveform is handled and processed by a DSP. However, this process, introduce new signal distortions, due to the new uncertainties introduced, that are the jitter error and the quantization error. The latter comes exclusively from the bit resolution of the A/D converter, while time jittering comes merely from the aperture jitter of the ADC, and from clock jitter of the sampling circuitry [1,2]. In this paper we examine the impact of those two parameters on the bit error rate performance of an UWB-IR fully digital receiver. In UWB-IR systems a pulse train, consisting of very short pulses and occupying very large spectrum [3], is transmitted. Several modulation schemes are used such as Bi-phase, Pulse Position, On-Off keying etc. [4]. In this paper we choose Binary Pulse Position Modulation (BPPM). We consider transmission through indoor multipath environment [5], in the presence of white Gaussian noise. The performance of the system is evaluated by the bit error probability (BEP) in terms of jitter and quantization noise. An expression of BEP is derived and numerically results are presented.

2. Analog to Digital Conversion

During the A/D conversion additional noise is produced at the output of the A/D converter due to two main reasons: Quantization and Jitter error. The first is illustrated in **Figure 1 (a)** and it is a result of the difference between the analog, continuous input signal and the digitized output of the ADC. The finite ADC resolution gives the form of the stairs-like signal. If an ADC has a bit resolution of N bits, it means that the output signal is coded at 2^N different binary numbers, from 0 to 2^N-1. Let assume that the input signals peak to peak amplitude (V_{pp}) is the same with the ADC full-scale voltage range. Then the corresponding quantization step is $Q = V_{pp} / 2^N$. An amplitude value at the input is mapped to the nearest N bit binary number and the

absolute difference between input-output can be from zero to $Q/2$, thus the quantization error is from $-Q/2$ to $Q/2$. We assume that the input signal can take any random value within a quantization step, with equal probability. Therefore the distribution of quantization error is uniform and its probability density function $f(x)$, is shown in **Figure 1(b)**. Obviously, it has a mean of zero and it is easy to prove that the standard deviation of quantization error is $\sigma_q = Q/\sqrt{12}$, as follows,

$$\sigma_q^2 = \int_{-\infty}^{+\infty} x^2 f(x)dx = \frac{1}{Q}\int_{-\frac{Q}{2}}^{+\frac{Q}{2}} x^2 dx = \frac{2}{Q}\int_0^{\frac{Q}{2}} x^2 dx = \frac{2}{Q}\frac{Q^3}{24} = \frac{Q^2}{12}$$

The second error that concerns our study is called jitter error and it is a result of the non infinite timing precision of the sampling procedure and the ADC imperfections. The fact is that there is an uncertainty at the sampling time which causes an uncertainty at the input voltage of the signal. This effect is shown in **Figure 2**. Let the input signal at an A/D converter be $V(t)$. We focus at the time t_1, corresponding at a multiplicate of sampling period. Due to jitter effect the sample taken by the ADC is the one at the time $t_1 + \Delta t_j$, where Δt_j is a random variable, assuming normally distributed with zero mean and standard deviation σ_j. The corresponding voltage error is then, $\Delta V_j = V(t_1 + \Delta t_j) - V(t_1)$. By rewriting this expression we have,

$$\Delta V_j = V(t_1 + \Delta t_j) - V(t_1) = \left[\frac{V(t_1 + \Delta t_j) - V(t_1)}{\Delta t_j}\right]\Delta t_j \quad (1)$$

For small Δt_j we can approximate the expression in the brackets with the first derivative of $V(t)$ [6], and obtaining,

$$\Delta V_j \approx \left[\frac{dV(t)}{dt}\right]_{t=t_1} \Delta t_j = \Delta t_j V'(t_1) \quad (2)$$

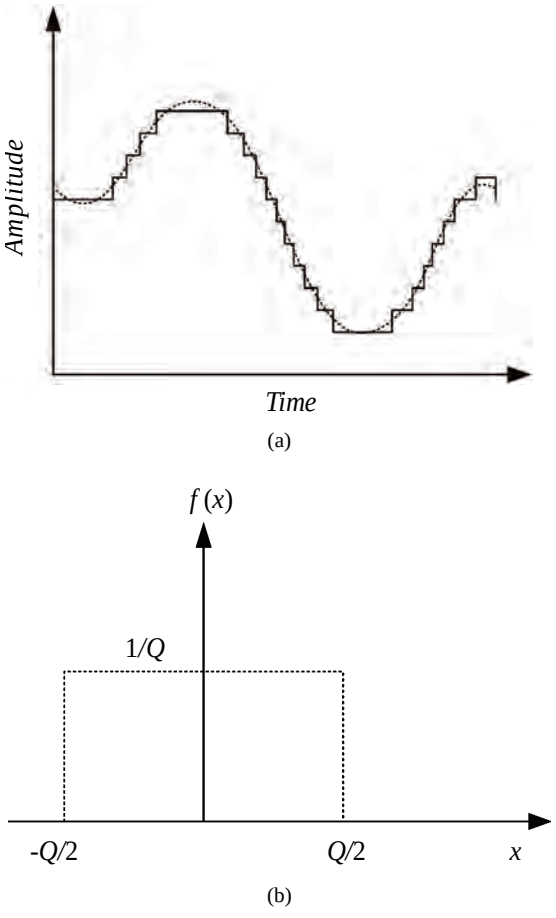

Figure 1. (a) Digitization of an analog continuous signal (dotted line) to discrete and quantized signal (normal line); (b) Uniform distribution $f(x)$ of quantization error x.

3. Signal Model Description

The transmitted pulses have the form of a Gauss monocycle, *i.e.* the first derivative of a standard Gauss pulse. **Figure 3** shows a schematic representation of the BPPM modulated transmitted signal. The bit period is T_f (frame period) and the time offset Δ represents the modulation index. Time is divided into frames, the period of

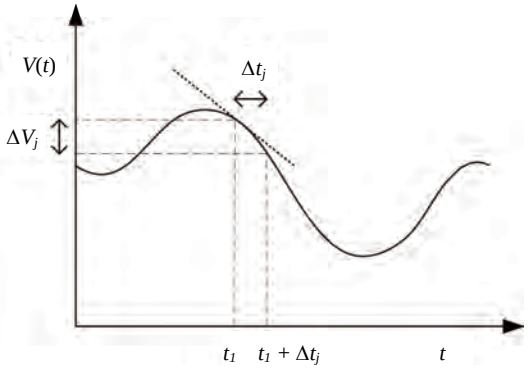

Figure 2. Jitter error effect.

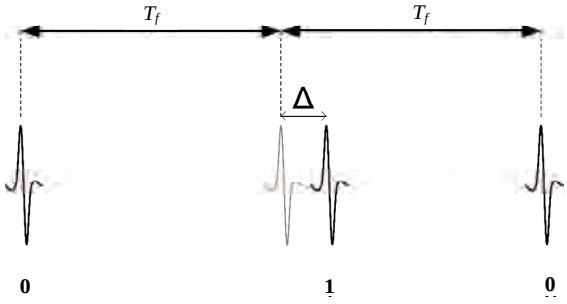

Figure 3. BPPM signaling.

the frames is T_f. We determine the symbol by its position within each frame. A logic "0" is a pulse at the beginning of the frame, while a logic '1' is delayed by a small amount of time Δ. The modulated pulses waveform $s(t)$ is expressed by Equation 3 below,

$$s(t) = \sum_{j=0}^{N-1} \sqrt{E_b} w(t - jT_f - b_j \Delta) \quad (3)$$

where, $w(t)$ is the pulse shape (first derivative of a Gaussian pulse) normalized to have total energy $\int_{-\infty}^{+\infty} |w(t)|^2 dt = 1$, E_b is the energy per bit, T_f is the frame period, b_j is the j-th bit, Δ is the BPPM modulation index, N is the total number of transmitted pulses. σ_w is related to the pulse width with the relationship $T_p = 2\pi\sigma_w$, where T_p represents the width of the pulse. The modulation index Δ is chosen to satisfy the orthogonality of the transmitted symbols, *i.e.*, $\int_{-\infty}^{+\infty} w(t)w(t-\Delta)dt = 0$. We choose Δ greater than the pulse duration, *i.e.*, $\Delta > T_p$.

4. Theoretical Analysis of Error Probability

In order to derive an expression for the probability of error, we consider the transmit and receive system model shown in **Figure 4**. The transmitted signal, $s(t)$, described above, propagates through a multipath channel with impulse response $h(t)$. Then it is converted from analog to digital using an A/D converter. As mentioned above the input signal is sampled at the ADC frequency and quantized with corresponding ADC resolution. For the detection of the symbols, a matched filtering technique is used. The matched filter is constructed by two correlators. The received signal is correlated with the expected symbols and the output is the difference of those. The output is sampled every frame period.

We assume perfect channel estimation and synchronization. From this point, the analysis continuous for the first frame period, *i.e.*, $0 \le t \le T_f$. We use vector notation, which represents the sampled versions of the signals.

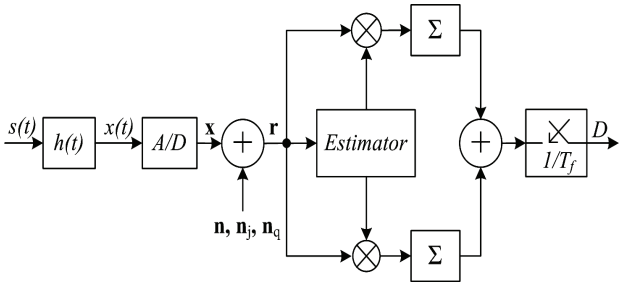

Figure 4. System transmission-reception model.

All the vectors has length, $N_f = T_f \cdot f_s$, where T_f is the frame period and f_s is the sampling frequency. The templates for the two symbols ($\mathbf{x}_0$, $\mathbf{x}_1$) are the transmitted symbols for '0' and '1' respectively after the channel, $\mathbf{n}$ is Gaussian process, representing total additive noise, with a mean value of zero and a double side power spectral density, $N_0/2$.

The channel impulse response, corresponding to the IEEE 802.15.3a model [5] for indoor multipath environments, is given by $h(t) = \sum_{l=0}^{L-1} \alpha_l \delta(t - \tau_l)$, where L is the total resolvable channel paths, α_l, τ_l are the gain coefficient and time delay, respectively, for the corresponding l path. Thus the transmitter signal after the channel is expressed as follows,

$$x(t) = (s * h)(t) = \sum_{l=0}^{L-1} a_l s(t - \tau_l) \quad (4)$$

where (*) denotes convolution.

The received discrete signal $\mathbf{r}$ is given in Equation 5 below,

$$\mathbf{r} = \mathbf{x} + \mathbf{n} + \mathbf{n}_j + \mathbf{n}_q \quad (5)$$

where, $\mathbf{n} \sim N(0, \sigma_n^2)$, $\sigma_n^2 = N_0/2$ is the total additive noise at the receiver, $\mathbf{n}_j$ is the noise vector due to jitter error and by using Equation 2. we have: $\mathbf{n}_j \sim N(0, \sigma_{jit}^2)$, $\sigma_{jit}^2 = \sigma_j^2 (\mathbf{x}')^{\mathrm{T}} \mathbf{x}'$ and $\mathbf{n}_q$ is the noise term due to quantization noise *i.e.* $\mathbf{n}_q \sim U(-\frac{Q}{2}, \frac{Q}{2})$, $\sigma_q = \frac{Q}{\sqrt{12}}$.

The derivative $\mathbf{x}'$ is calculated from Equation 3 and Equation 4, as follows,

$$\begin{aligned} \frac{d}{dt}x(t) &= \frac{d}{dt}\sum_{l=0}^{L-1} a_l s(t - \tau_l) \\ &= \sum_{j=0}^{N-1}\sum_{l=0}^{L-1} \sqrt{E_b} \frac{d}{dt} w(t - jT_f - b_j\Delta - \tau_l) \end{aligned} \quad (6)$$

and by taking the discrete (sampled) vector. The waveform $w(t)$ as mentioned before is the first derivative of a gauss monopulse, thus $\frac{d}{dt}w(t)$ is the second derivative of the pulse. To obtain an expression for the probability of error on symbol detection, we must first define the decision metric at the output of the correlators in **Figure 4** at time $t = T_f$. For simplicity we consider the transmission of a '0' and in the same way we can derive an expression for the '1'. The decision metric is then,

$$\begin{aligned} D_0 &= \mathbf{r}_0^{\mathrm{T}} (\mathbf{x}_0 - \mathbf{x}_1) = (\mathbf{x}_0 + \mathbf{n} + \mathbf{n}_j + \mathbf{n}_q)^{\mathrm{T}} (\mathbf{x}_0 - \mathbf{x}_1) \\ &= \mathbf{x}_0^{\mathrm{T}} (\mathbf{x}_0 - \mathbf{x}_1) + (\mathbf{n} + \mathbf{n}_j + \mathbf{n}_q)^{\mathrm{T}} (\mathbf{x}_0 - \mathbf{x}_1) \\ &= \mathbf{x}_0^{\mathrm{T}}\mathbf{x}_0 - \mathbf{x}_0^{\mathrm{T}}\mathbf{x}_1 + (\mathbf{n} + \mathbf{n}_j + \mathbf{n}_q)^{\mathrm{T}} (\mathbf{x}_0 - \mathbf{x}_1) \\ &= R_{xx}(0) - R_{xx}(\Delta) + (\mathbf{n} + \mathbf{n}_j)^{\mathrm{T}} (\mathbf{x}_0 - \mathbf{x}_1) + \mathbf{n}_q^{\mathrm{T}} (\mathbf{x}_0 - \mathbf{x}_1) \end{aligned}$$

and we obtain,

$$D_0 = R_{xx}(0) - R_{xx}(\Delta) + N_n + N_q \quad (7)$$

where, $R_{xx}(\tau)$ is the autocorrelation function of vector $\mathbf{x}$ at time τ, $N_n = \left(\mathbf{n} + \mathbf{n}_j\right)^{\mathrm{T}} \left(\mathbf{x}_0 - \mathbf{x}_1\right)$ is a gaussian random process including thermal noise and jitter noise *i.e.*, $N_n \sim N(0, \sigma_{g1}^2)$, $\sigma_{g1}^2 = (\sigma_n^2 + \sigma_{jit}^2)\left(\mathbf{x}_0 - \mathbf{x}_1\right)^{\mathrm{T}} \left(\mathbf{x}_0 - \mathbf{x}_1\right)$, and $N_q = \mathbf{n}_q^{\mathrm{T}} \left(\mathbf{x}_0 - \mathbf{x}_1\right)$ is the noise term due to quantization which is a summation of N_f terms of uniformly distributed random variables. Because of the fact that N_f is usually a sufficiently large number we may use the central limit theorem [7], and approximate this term with a Gaussian process with variance σ_{g2}^2 *i.e.*,

$$N_q \sim N(0, \sigma_{g2}^2),\ \sigma_{g2}^2 = \sigma_q^2 \left(\mathbf{x}_0 - \mathbf{x}_1\right)^{\mathrm{T}} \left(\mathbf{x}_0 - \mathbf{x}_1\right)$$

Therefore the decision metric is a Gaussian r.v. with mean $R_{xx}(0) - R_{xx}(\Delta)$ and standard deviation $\sqrt{\sigma_{g1}^2 + \sigma_{g2}^2}$, thus the probability of error is expressed as follows:

$$P_e = Q\left(\frac{R_{xx}(0) - R_{xx}(\Delta)}{\sqrt{\sigma_{g1}^2 + \sigma_{g2}^2}}\right) \quad (8)$$

5. Numerical Results

After the above analysis we calculate the error probability numerically using simulation program to evaluate Equation 8 and by averaging over 1000 channel realizations corresponding to IEEE 802.15.3a model CM1. The parameters that used are: width of the pulses $T_p = 200$ psec, modulation index $\Delta = 1$nsec, frame period $T_f = 100$ nsec, sampling frequency $f_s = 20$ GHz, yielding a channel time resolution of 50 psec. **Figure 5** shows the bit error probability (BEP) as a function of signal to noise ratio with 6 bit ADC resolution and with different number of jitter standard deviation. We can see that jitter is a significant factor to the performance especially when noise has lower power. Beyond 10 dB of signal to noise ratio, jitter is the main cause of performance degradation.

Figure 6 shows the error probability as a function of jitter standard deviation. On top of the graph we set the bit resolution of A/D at 4 bits and the curves correspond to several signal to noise ratios. Again we can see that in cases of higher SNR, the error probability has strong dependence on jitter. In the graph at the bottom, we set SNR to 10 dB and we change the bit resolution of ADC. It is interesting to notice that an increase of bit resolution more than 4 bits doesn't improve performance. The dependence of error probability of bit resolution is shown

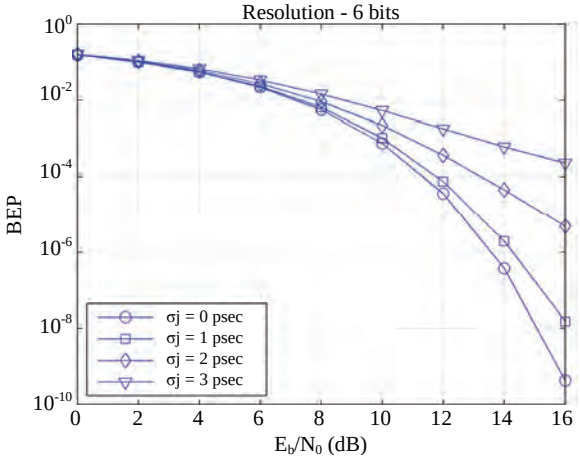

Figure 5. Bit error probability as a function of signal to noise ratio (E_b/N_0) for different values of jitter standard deviation (psec), with 6 bit ADC resolution

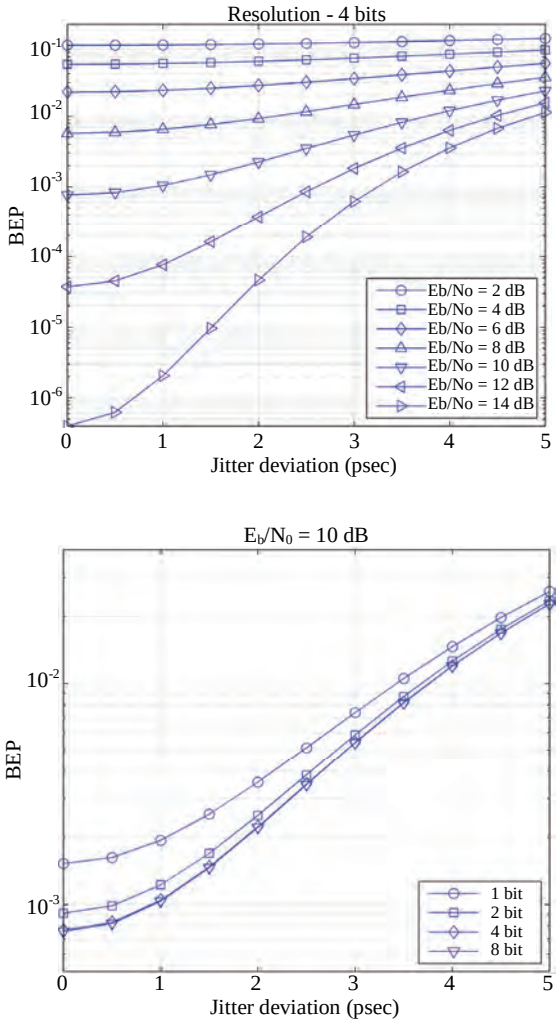

Figure 6. Bit error probability as a function of jitter standard deviation (psec), varying signal to noise ratio, with 4 bit ADC resolution (top graph) and varying ADC resolution with E_b/N_0=10dB (bottom graph).

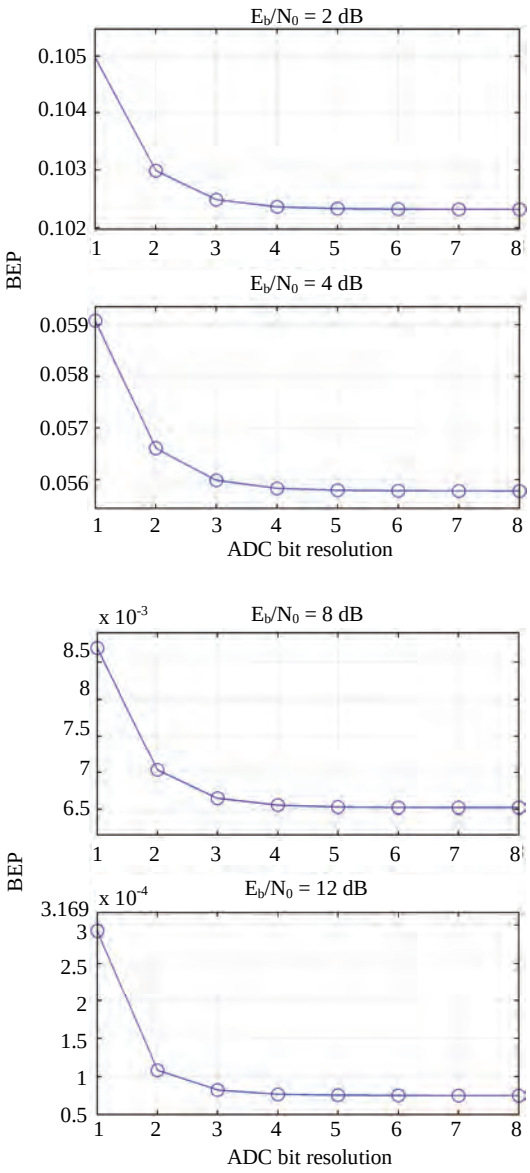

Figure 7. Bit error probability as a function of ADC bit resolution with 1psec jitter, and with different values of signal to noise ratio (E_b/N_0).

in **Figure 7**, with jitter standard deviation at 1 psec and varying SNR. In all cases there is a limit at bit resolution and it is obvious that a use of 4 bits is adequate to lead to a sufficient performance.

6. Conclusions

In the present paper we have studied the impact of the two parameters that affect the performance of the digitizing stage. These parameters are the jitter error and the quantization error. The error probability dependence from both parameters was investigated and presented. Both of them are critical to error performance of Ultra-Wideband Impulse Radio systems. Jitter error plays an important role especially when additive noise is not very strong. Quantization error is also a significant factor for the BEP improvement for bit resolution below 4 bits. For more than 4 bits of ADC resolution the improvement is negligible. From the above study in order to assure low BEP, the jitter must be kept as low as possible (2-3 psec) and the ADC resolution above 4 bits.

7. Acknowledgements

This research project (PENED) is co-financed by E. U. - European Social Fund (80%) and the Greek Ministry of Development-GSRT (20%).

8. References

[1] V. N. Christofilakis, A. A. Alexandridis, P. Kostarakis and K. P. Dangakis, "Software Defined Radio Implementation Aspects Related to the ADC Performance," *Proceedings of the 6th International Multiconference on Circuits, Systems, Communications and Computers*, Crete, 7-11 July 2002, pp. 3231-3239.

[2] R. H. Walden, "Analog-to-Digital Converter Survey and Analysis," *IEEE Journal on Selected Areas in Communications*, Vol. 17, No. 4, April 1999, pp. 539-550.

[3] X. Shen, M. Guizani, R. C. Qiu and T. Le-Ngoc, "Ultra-Wideband Wireless Communication and Networks," John Wiley & Sons, Malden, 2006.

[4] I. Güvenc and H. Arslan, "On the Modulation Options for UWB Systems," *Proceedings of IEEE Conference on Military Communication*, Boston, Vol. 2, 2003, pp. 892-897.

[5] J. R. Foerster, M. Pendergrass and A. F. Molisch, "A Channel Model for Ultrawideband Indoor Communication," *Proceedings of International Symposium on Wireless Personal Multimedia Communication*, Yokosuka, October 2003.

[6] A. Fort, M. Chen, R. W. Brodersen, C. Desset, P. Wambacq and L. V. Biesen, "Impact of Sampling Jitter on Mostly-Digital Architectures for UWB Bio-Medical Applications," *Proceedings of IEEE International Conference on Communications*, Glasgow, 24-28 June 2007, pp. 5769-5774.

[7] A. Papoulis and S. U. Pillai, "Probability, Random Variables and Stochastic Process," McGraw-Hill, New York, 2002.

Int. J. Communications, Network and System Sciences, **2010, 3, 430-433**
doi:10.4236/ijcns.2010.35056 Published Online May 2010 (http://www.SciRP.org/journal/ijcns/)

Scientific Research

Outage Performance of Opportunistic Amplify-and-Forward Relaying over Asymmetric Fading Environments

Sudhan Majhi[1,2,3], Youssef Nasser[1,2,3], Jean François Hélard[1,2,3]
[1]*European University of Brettany, Rennes, France*
[2]*Institut National des Sciences Appliquees, Rennes, France*
[3]*Institute of Electronics and Telecommunications of Rennes, Rennes, France*
E-mail: {*sudhan.majhi, youssef.nasser, jean-francois.helard*}*@insa-rennes.fr*
Received February 16, 2010; *revised March* 21, 2010; *accepted April* 22, 2010

Abstract

This letter analyzes the outage probability of opportunistic amplify-and-forward relaying over asymmetric and independent but non-identically distributed (i.n.d) fading environments. The work investigates the scenarios where cooperative nodes are located at different geographical locations. As a result, the different signals are affected by different i.n.d fading channels, one may undergo Rician fading distribution and others may undergo Rayleigh fading distribution. In this letter, a lower bound of the outage probability for various asymmetric fading environments is derived at high SNR by applying the initial value theorem. The analytical model is validated through Monte-Carlo simulation results.

Keywords: Outage Probability, Opportunistic Relaying, Amplify-and-Forward Relaying, Rayleigh and Rician Fading Channels, Asymmetric Fading Channels, Independent and Non-Identically Distributed

1. Introduction

Cooperative relaying is a promising technology for future wireless communications. It can benefit most of the leverages of multiple input multiple output (MIMO) without using the conventional MIMO schemes [1]. Among the cooperative techniques, the opportunistic relaying, in which only one relay (R) node forwards the source's (S) data to the destination (D) has shown its efficiency compared to other techniques [2].

The outage performance of opportunistic amplify-and-forward (AF) relaying over a symmetric fading environment is widely investigated in [1,3,4]. However, in practice, cooperative nodes are usually located in different geographical location environments and at different distances with respect to S and D. Therefore, one link could be either in line-of-sight (LOS) situation or in non-LOS (NLOS) situation. For example, the fixed relay nodes used for forwarding source's data to a specific region (e.g. tunnel, behind the building) often use directional antenna, so the R-D link is usually in a LOS situation. However, we cannot assume such a situation in all transmission environments especially when D is in a deep shadowing region with respect to S. The outage performance analysis of opportunistic relaying for mixed and i.n.d fading environments is, therefore, of practical importance.

The asymmetric fading channel is introduced in [5]. However, the authors of this work assume additive white Gaussian noise (AWGN) channel of the R-D link. In [6], an approximation of the outage performance over asymmetric fading channel, *i.e.*, Rayleigh and Rician, is given. However, to the best knowledge of the authors, no closed-form expression is provided. In this letter, the analytical model of the outage probability of opportunistic AF relaying over asymmetric and i.n.d fading environments is given. Then, the lower bound of the outage probability for high SNR values is deduced and verified through Monte-Carlo simulations.

2. System Model and SNR Evaluation

In this framework, we consider a general 2-hop AF relaying network consisting of S, m relays, R_i, $i=1,2,...,m$ and D. We assume that D performs maximum ratio combining at the receiving side. The equivalent instantaneous end-to-end signal-to-noise ratio (SNR) for opportunistic

AF relaying is given as [3]:

$$SNR_d = \frac{P_s\left|h_{sd}\right|^2}{N_{sd}} + \max_i \frac{\dfrac{P_s\left|h_{sr_i}\right|^2}{N_{sr_i}}\dfrac{P_s\left|h_{r_id}\right|^2}{N_{r_id}}}{\dfrac{P_s\left|h_{sr_i}\right|^2}{N_{sr_i}} + \dfrac{P_s\left|h_{r_id}\right|^2}{N_{r_id}} + 1} \quad (1)$$

where $\left|h_{ab}\right|^2$ represents the channel gain of the a-b link, P_a is the power transmitted by the node a. As mentioned in [3], we assume that AWGN variance is $N_{ab} = 1/\gamma_0$, $\forall a,b$ where γ_0 is proportional to the system SNR.

For simplicity reasons, we use different notations of the random variables of the different fading distributions. For the Rayleigh fading, let $\gamma_{ab} = P_a\left|h_{ab}\right|^2$ be the instanttaneous signal power and for the Rician fading, the instantaneous signal power is denoted as ξ_{ab}. The probability density function (PDF) of γ_{ab} and ξ_{ab} are expressed respectively as:

$$f_{\gamma_{ab}}(x) = \frac{1}{\overline{\gamma}_{ab}} e^{-x/\overline{\gamma}_{ab}} \quad (2)$$

$$f_{\xi_{ab}}(\xi) = \frac{K_{ab}+1}{\overline{\xi}_{ab}} e^{-\xi(K_{ab}+1)/\overline{\xi}_{ab} - K_{ab}} I_0\left(\sqrt{\frac{4K_{ab}(K_{ab}+1)\xi}{\overline{\xi}_{ab}}}\right) \quad (3)$$

where, $\overline{\gamma}_{ab} = E\{\gamma_{ab}\}$ $\overline{\xi}_{ab} = E\{\xi_{ab}\}$ and K_{ab} is the Rician factor. $E\{.\}$ holds for expectation value.

The upper bound of the instantaneous SNR of (1) for the opportunistic AF relaying is defined as:

$$SNR_{ub} = P_s\left|h_{sd}\right|^2\gamma_0 + \max_i\left(\min\left(P_s\left|h_{sr_i}\right|^2, P_s\left|h_{r_id}\right|^2\right)\right) \quad (4)$$

This instantaneous SNR value will be used in the following section to evaluate the outage probability.

3. Analysis of Outage Probability

In this section, we provide the lower bound of the outage probability of opportunistic AF relaying for different channels given in **Figure 1**.

3.1. Asymmetric Channel I

***Theorem* 1:** If S-D link is Rayleigh fading channel and S-R and R-D links are Rician fading channels, then the lower bound of the outage probability over asymmetric channel I is:

$$p_{out}^I = \frac{1}{(m+1)\overline{\gamma}_{sd}} \prod_{i=1}^{m}\left(\frac{(K_{sr_i}+1)}{\overline{\xi}_{sr_i} e^{K_{sr_i}}} + \frac{(K_{r_id}+1)}{\overline{\xi}_{r_id} e^{K_{r_id}}}\right)\gamma^{m+1} \quad (5)$$

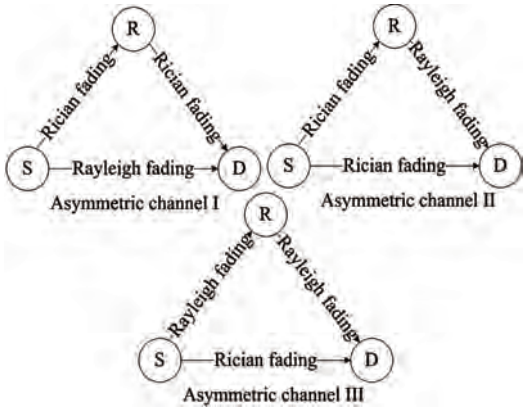

Figure 1. Different asymmetric fading channels of a cooperative network.

Proof: By using $\gamma_{sd} = P_s\left|h_{sd}\right|^2$, $\xi_{sr_i} = P_s\left|h_{sr_i}\right|^2$ and $\xi_{r_id} = P_s\left|h_{r_id}\right|^2$ in [4], the outage probability over the asymmetric channel I can be written as:

$$p_{out}^I = Pr[\gamma_{ub}^I < \gamma] \quad (6)$$

where SNR_{ub} is derived to $\gamma_{ub}^I = \gamma_{sd} + \xi_{max}$, $\gamma = \left(2^{2R}-1\right)/\gamma_0$, $\xi_{max} = \max\left(\xi_1,\xi_2,...,\xi_m\right)$ and $\xi_i = \min\left(\xi_{sr_i},\xi_{r_id}\right)$.

The cumulative distribution function (CDF) of the random variable ξ_i over i.n.d is given as:

$$\begin{aligned} F_{\xi_i}(\gamma) &= 1-\left(1-Pr[\xi_{sr_i}<\gamma]\right)\left(1-Pr[\xi_{r_id}<\gamma]\right) \\ &= 1-Q_1\left(\sqrt{2K_{sr_i}}, \sqrt{\frac{2(K_{sr_i}+1)\gamma}{\overline{\xi}_{sr_i}}}\right)\times \\ &\quad Q_1\left(\sqrt{2K_{r_id}}, \sqrt{\frac{2(K_{r_id}+1)\gamma}{\overline{\xi}_{r_id}}}\right) \end{aligned} \quad (7)$$

where $Q_1(,)$ is the 1st order Marcum Q-function and the PDF of ξ_i is obtained by differentiating above as:

$$\begin{aligned} f_{\xi_i}(\gamma) &= \left(\sqrt{2K_{sr_i}}, \sqrt{\frac{2(K_{sr_i}+1)\gamma}{\overline{\xi}_{sr_i}}}\right) f_{\xi_{r_id}}(\gamma) + \\ &\quad Q_1\left(\sqrt{2K_{r_id}}, \sqrt{\frac{2(K_{r_id}+1)\gamma}{\overline{\xi}_{r_id}}}\right) f_{\xi_{sr_i}}(\gamma) \end{aligned} \quad (8)$$

The CDF of the random variable ξ_{max} over i.n.d fading channel can be expressed as:

$$F_{\xi_{max}}(\gamma) = \prod_{i=1}^{m} F_{\xi_i}(\gamma) \quad (9)$$

and the corresponding PDF of ξ_{max} is obtained by differentiating the above as:

$$f_{\xi_{max}}(\gamma) = \sum_{i=1}^{m} f_{\xi_i}(\gamma) \prod_{\substack{j=1 \\ j \neq i}}^{m} F_{\xi_j}(\gamma) \quad (10)$$

Since $F_{\xi_i}(0) = 0$, the $(m-1)$th order derivative of (10) at high SNR *i.e.*, at $\gamma = 0$ as $\gamma_0 \to \infty$, can be written as:

$$\frac{\partial^{m-1}}{\partial \gamma^{m-1}} f_{\xi_{max}}(\gamma)\big|_{\gamma=0} = m! \prod_{i=1}^{m} f_{\xi_i}(0) \quad (11)$$

The outage probability given in (6) is a CDF of γ_{ub}^{I}, which can be evaluated by using the initial value theorem (IVT) of the Laplace Transformation (LT). The LT of the PDF of the random variable γ_{ub}^{I} can be expressed by using Equation 15 in [3] and, then (11), as:

$$\begin{aligned} L\left\{ f_{\gamma_{ub}}^{I}(\gamma) \right\} &= \frac{1}{s^{m+1}} f_{\gamma_{sd}}(0) \frac{\partial^{m-1}}{\partial \gamma^{m-1}} f_{\xi_{max}}(\gamma)\big|_{\gamma=0} \\ &= \frac{m!}{s^{m+1}} f_{\gamma_{sd}}(0) \prod_{i=1}^{m} f_{\xi_i}(0) \end{aligned} \quad (12)$$

Since $f_{\gamma_{sd}}(0)$ and $f_{\xi_i}(0)$ are constant with respect to the variable s, the PDF of γ_{ub}^{I} is obtained by applying the inverse LT (ILT) on (12) as:

$$f_{\gamma_{ub}}^{I}(\gamma) = \gamma^{m} f_{\gamma_{sd}}(0) \prod_{i=1}^{m} f_{\xi_i}(0) \quad (13)$$

We complete the proof by integrating (13) and substituting the vale of $f_{\gamma_{sd}}(0)$ and $f_{\xi_i}(0)$.

3.2. Asymmetric Channel II

***Theorem* 2:** If S-D and S-R links are Rician fading channels and R-D link is Rayleigh fading channel, then the lower bound of the outage probability over asymmetric channel II is:

$$p_{out}^{II} = \frac{(K_{sd}+1)}{(m+1)\bar{\xi}_{sd} e^{K_{sd}}} \prod_{i=1}^{m} \left(\frac{(K_{sr_i}+1)}{\bar{\xi}_{sr_i} e^{K_{sr_i}}} + \frac{1}{\bar{\gamma}_{r_i d}} \right) \gamma^{m+1} \quad (14)$$

Proof: For the asymmetric channel II, we use $\xi_{sd} = P_s |h_{sd}|^2$, $\xi_{sr_i} = P_s |h_{sr_i}|^2$ and $\gamma_{r_i d} = P_s |h_{r_i d}|^2$. The outage probability can be expressed as:

$$p_{out}^{II} = Pr[\gamma_{ub}^{II} < \gamma] \quad (15)$$

where $\gamma_{ub}^{II} = \xi_{sd} + g_{max}$, $g_{max} = \max(g_1, g_2, ..., g_m)$ and $g_i = \min(\xi_{sr_i}, \gamma_{r_i d})$. The CDF of the random variable g_i over i.n.d fading channel can be written as:

$$F_{g_i}(\gamma) = 1 - Q_1\left(\sqrt{2K_{sr_i}}, \sqrt{\frac{2(K_{sr_i}+1)\gamma}{\bar{\xi}_{sr_i}}} \right) \times \left(1 - F_{\gamma_{r_i d}}(\gamma)\right) \quad (16)$$

where $F_{\gamma_{r_i d}}(\gamma)$ is the CDF of the random variable $\gamma_{r_i d}$. The corresponding PDF of g_i is expressed as:

$$\begin{aligned} f_{g_i}(\gamma) = Q_1\left(\sqrt{2K_{sr_i}}, \sqrt{\frac{2(K_{sr_i}+1)\gamma}{\bar{\xi}_{sr_i}}} \right) f_{\gamma_{r_i d}}(\gamma) + \\ \left(1 - F_{\gamma_{r_i d}}(\gamma)\right) f_{\xi_{sr_i}}(\gamma) \end{aligned} \quad (17)$$

Similarly, by using the IVT and the ILT, the PDF of γ_{ub}^{II} can be derived as:

$$f_{\gamma_{ub}}^{II}(\gamma) = \gamma^{m} f_{\xi_{sd}}(0) \prod_{i=1}^{m} f_{g_i}(0) \quad (18)$$

By integrating (18), we complete the proof.

3.3. Asymmetric Channel III

***Theorem* 3:** If S-D link is Rician fading channel and S-R and R-D link are Rayleigh fading channels, the corresponding lower bound of outage probability is:

$$p_{out}^{III} = \frac{(K_{sd}+1)}{(m+1)\bar{\xi}_{sd} e^{K_{sd}}} \prod_{i=1}^{m} \left(\frac{1}{\bar{\gamma}_{sr_i}} + \frac{1}{\bar{\gamma}_{r_i d}} \right) \gamma^{m+1} \quad (19)$$

Proof: For the asymmetric channel III, we use $\xi_{sd} = P_s |h_{sd}|^2$, $\gamma_{sr_i} = P_s |h_{sr_i}|^2$ and $\gamma_{r_i d} = P_s |h_{r_i d}|^2$. The outage probability can be written as:

$$p_{out}^{III} = Pr[\gamma_{ub}^{III} < \gamma] \quad (20)$$

where $\gamma_{ub}^{III} = \xi_{sd} + \gamma_{max}$, $\gamma_{max} = max(\gamma_1, \gamma_2, ..., \gamma_m)$ and $\gamma_i = min(\gamma_{sr_i}, \gamma_{r_i d})$. The corresponding PDF of the random variable γ_i is given by:

$$f_{\gamma_i}(\gamma) = \left(1 - F_{\gamma_{sr_i}}(\gamma)\right) f_{\gamma_{r_i d}}(\gamma) + \left(1 - F_{\gamma_{r_i d}}(\gamma)\right) f_{\gamma_{sr_i}}(\gamma) \quad (21)$$

Again by using the IVT and ILT, the PDF of γ_{ub}^{III} is obtained as:

$$f_{\gamma_{ub}}^{III}(\gamma) = \gamma^{m} f_{\xi_{sd}}(0) \prod_{i=1}^{m} f_{\gamma_i}(0) \quad (22)$$

By integrating (22), we complete the proof.

Similarly, the outage probability of other possible asymmetric channels can be derived by using the above procedure. The upper bound of the outage probability of the opportunistic AF relaying can be derived simply by using the above method and Equation 8 in [7].

4. Numerical Examples

In this section, analytical and Monte-Carlo simulation results are presented. Since the channels are i.n.d, we set different means for different S-Ri/Ri-D links. In the

Rician fading channel, the Rician factor K_{ab} is uniformly distributed in [2,3] and the mean $\overline{\gamma}_{ab}$ of the NLOS components are uniformly distributed in [0,1]. The LOS components are derived for a given K_{ab} and $\overline{\gamma}_{ab}$.

It is clear from (5), (14) and (19) that the outage probability over Rician fading channel is obtained by substituting $1/\overline{\gamma}_{sd} = (K_{sd}+1)e^{K_{sd}} / \overline{\xi}_{sd}$ in (5) and the outage probability over Rayleigh fading channel is obtained by substituting $K_{sd} = 0$ in (19). **Figure 2** shows the lower bound of the outage probability over the symmetric and asymmetric fading environments. Due to the presence of LOS signal, the outage performance over Rician fading channel outperforms all other scenarios. Inversely, due to the absence of direct signal, the Rayleigh fading channel has poorer outage performance than the other scenarios.

The opportunistic relaying provides better outage performance than without cooperation. It implies that the outage performance of opportunistic relaying depends mainly on cooperative links (S-R and R-D links). For this reason, asymmetric channel I provides better outage performance than the asymmetric channel II and asymmetric channel III due to the presence of LOS signal inboth S-R and R-D links.

We also note that asymmetric channel II provides better outage performance than asymmetric channel III. Since S-D and R-D links undergo the same fading in both scenarios, the LOS component existing in S-R link of scenario II highly improves the outage performance. It is clear from the above discussion that S-R is a dominating link, therefore, it is better to localize the opportunistic relay node in LOS environment with respect to S in order to improve the overall outage performance. Finally, the Monte-Carlo simulation results provided in **Figure 2** shows that the analytical outage probabilities are a tight bound at medium and high SNR regime.

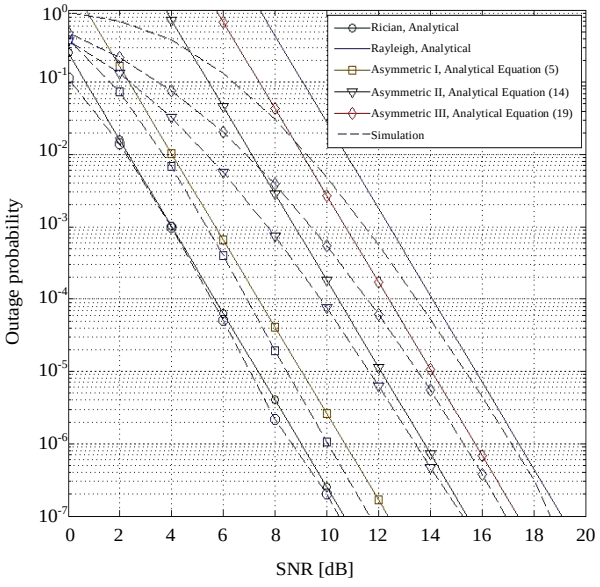

Figure 2. The outage probability over asymmetric channel I, asymmetric channel II and asymmetric channel III. Due to the high SNR approximation for the analysis, analytical results converge with Monte-Carlo simulation results at medium and high SNR regime.

5. Conclusions

In this letter, the outage performance of opportunistic AF relaying over asymmetric and i.n.d fading environments has been investigated. A lower bound of the outage probability has been derived and validated through Monte-Carlo simulation results. We show that the outage performance is better when the relay is in LOS situation with respect to the source rather than to the destination.

6. Acknowledgements

The authors would like to thank the European IST-FP7 WHERE project and the European Network of Excellence NEWCOM++ for support of this work.

7. References

[1] J. N. Laneman, D. N. C. Tse and G. W. Wornell, "Cooperative Diversity in Wireless Networks: Efficient Protocols and Outage Behavior," *IEEE Transactions of Information Theory*, Vol. 50, No. 12, 2004, pp. 3062-3080.

[2] Y. Zhao, R. Adve and T. J. Lim, "Outage Probability at Arbitrary SNR with Cooperative Diversity," *IEEE Communications Letters*, Vol. 9, No. 8, 2005, pp. 700-703.

[3] Y. Zhao, R. Adve and T. J. Lim, "Symbol Error Rate of Selection Amplify-and-For- ward Relay Systems," *IEEE Communications Letters*, Vol. 10, No. 11, 2006, pp. 757-759.

[4] A. Bletsas, H. Shin and M. Z. Win, "Cooperative Communication with Outage Optimal Opportunistic Relaying," *IEEE Transactions on Wireless Communications*, Vol. 6, No. 9, 2007, pp. 3450-3459.

[5] M. Katz and S. Shamai, "Relaying Protocols for two Colocated Users," *IEEE Transactions on Information Theory*, Vol. 52, No. 6, 2009, pp. 2329-2344.

[6] H. Suraweera, G. Karagiannidis and P. Smith, "Performance Analysis of the Dual-Hop Asymmetric Fading Channel," *IEEE Transactions on Wireless Communications Letters*, Vol. 8, No. 6, 2009, pp. 2783-2788.

[7] K.-S. Hwang, Y.-C. Ko and M.-S. Alouini, "Performance Analysis of Incremental Opportunistic Relaying over Identically and Non-Identically Distributed Cooperative Paths," *IEEE Transactions on Wireless Communications*, Vol. 8, No. 4, April 2009, pp. 1953-1961.

Int. J. Communications, Network and System Sciences, **2010, 3, 434-440**
doi:10.4236/ijcns.2010.35057 Published Online May 2010 (http://www.SciRP.org/journal/ijcns/)

Scientific Research

Measurements of Balun and Gap Effects in a Dipole Antenna

Constantinos Votis[1], Vasilis Christofilakis[1,2], Panos Kostarakis[1]
[1]*Physics Department, University of Ioannina, Panepistimioupolis, Ioannina, Greece*
[2]*Siemens Enterprise Communications, Enterprise Products Development, Athens, Greece*
E-mail: *kvotis@grads.uoi.gr, basilios.christofilakis@siemens-enterprise.com, kostarakis@uoi.gr*
Received February 12, 2010; *revised March* 15, 2010; *accepted April* 18, 2010

Abstract

In the present paper, design and analysis of a 2.4 GHz printed dipole antenna for wireless communication applications are presented. Measurements on return loss and radiation pattern of this antenna configuration are included in this investigation. The printed dipole is combined with the feeding structure of a microstrip via-hole balun and is fabricated on an FR-4 printed-circuit-board substrate. Two inevitable discontinuities are introduced by this antenna architecture in the form of right-angle bends in the microstrip feed line and in the dipole's gap, respectively. The impact of mitering these bends in the reflection coefficient, resonance bandwidth and radiation pattern of antenna has been investigated by means of simulation and experiment.

Keywords: Printed Dipole, Integrated Balun, S-Parameters, Radiation Pattern

1. Introduction

The microstrip antenna architecture, in general, offers inherent narrow bandwidth and quite low gain. These limitations do not provide wide usage of these antennas in wireless applications systems. Besides, the evolution of wireless communications leads to more compact and small equipment that demanding antennas with smaller size and profile. Hence, the scientific community has started to investigate methods to improve this antenna architecture and provide better quality of services on wireless communication systems. In this way, many research activities were based on the printed dipole antenna because it has low profile, simple structure and omnidirectional radiation pattern. In order to develop this antenna configuration a printed dipole antenna with integrated balun and microstrip line as feeding structure was proposed [1-3]. Based on these considerations, we design and fabricate a 2.4-GHz printed dipole antenna with integrated microstrip balun. This antenna design offers all the advantages of printed circuits and the corresponding geometry characteristics have been in detail studied and investigated [4-5]. In order to improve the bandwidth and the gain of this architecture we study and investigate the impact on variations of the *l* and *w* geometrical parameters on antenna performance. The first corresponds to the right angle bend in the microstrip balun and the second affects the dipole's arms. Details of the structure and design process are presented in the next section (Section 2). The corresponding simulated and measured results are presented and discussed in Section 3. The paper concludes in Section 4.

2. Design Process and Structure

The geometry and design parameters of the 2.4 GHz printed dipole antenna are drawn in **Figure 1**. It is a modified antenna design that was introduced by the corresponding literature [1-4].

This printed dipole antenna was etched on Fr4 substrate with thickness h = 1.5 mm and permittivity ε_r = 4.4. The ground plane of the microstrip line and the dipole strips were printed at the bottom layer. A microstrip via-hole balun acts as an unbalance-to-balance transformer from the coaxial line to the printed dipole strip. The lengths of the dipole—arm strips and the microstrip balun are approximately a quarter—wavelength [4-6]. Based on matching techniques theory, the integrated balun affects the current flow at each dipole—arm, because of cancellation of the current flow to ground on the outside part of the outer conductor in corresponding coaxial line. In fact, the balun configuration ensures that the currents which flow the dipole arms become quite identical without eliminating the radiation efficiency [6].

The structure parameters of the proposed dipole for 2.4 GHz frequency point are listed as follows:

Dipole strips: length L_1 = 20.8 mm, width W_1 = 6 mm, dipole gap: g_1 = 3 mm;

Microstrip balun: length L_2 = 32 mm, L_3 = 16 mm, L_4 = 3 mm, L_5 = 3 mm, width W_2 = 3 mm, W_3 = 5 mm, W_4 = 3 mm, gap g_2 = 1mm;

Via radius: r = 0.375 mm;

Ground plane: length L_6 = 12 mm, width W_5 = 17 mm;

Side of microstrip bend: *l* variable;

Side of dipole strip bend: *w* variable.

Accurate dimensions of each part of dipole and integrated balun have numerically been computed and investigated [4,5,7]. These parameters were specified to achieve desired performance of the printed dipole antenna in the frequency of 2.4 GHz. Both simulated and experimental results introduce this performance. The prototype printed dipole antenna is shown in **Figure 2**.

This prototype dipole on which the discontinuities are not investigated (*l* and *w* unchanged) has frequency resonance at about 2.45 GHz and an efficient bandwidth for wireless applications at 2.4 GHz – ISM band.

An interesting approximation for these discontinuities is proposed. As already mentioned, the right—angle bends at the microstrip feed line and at the strip arms of the printed dipole are inevitable discontinuities and can cause degradation in circuit performance. This is due to the fact that such discontinuities introduce parasitic reactances which can lead to phase and amplitude errors, input and output mismatch and possibly spurious coupling [8]. Based on discontinuities' forms, microwave engineering theory has proposed thoughts to face the difficulties. One approach in order to eliminate this effect is to compensate the discontinuity directly, by chamfering or mitering the conductor. That way, the excess capacitance at the bend is reduced [8]. It is generally known that the optimum value of the miter length depends on the characteristic impedance and the bend angle. This is the purpose of the proposed procedure. The variation's impact of the corresponding parameters l and w on return loss, resonance bandwidth and radiation pattern have been investigated. About resonance bandwidth definition is specified as the frequency range in which return loss is less than –10 dB.

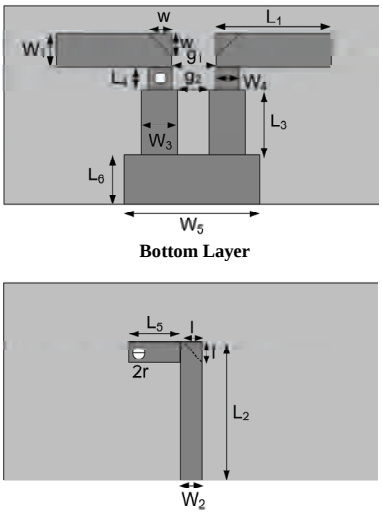

Figure 1. Geometry of printed dipole antenna with integrated microstrip balun.

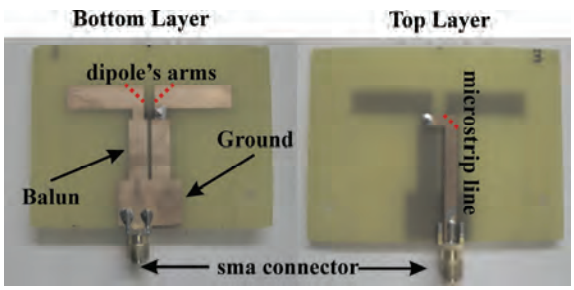

Figure 2. Prototype printed dipole.

These variations on the values of the l and w parameters introduce geometrical modifications in the prototype dipole architecture so as to obtain the corresponding different printed dipole antennas. Therefore, based on the prototype antenna design (**Figure 2**) sixteen different printed dipole antennas have been designed and implemented. Each of them has different value of *l* and *w* parameter. Both these values are ranged from 0 mm to 3 mm, respectively. The return loss and radiation pattern of the corresponding printed dipole antenna in each case were investigated.

3. Results and Discussion

The defined variations of *l* and *w* parameters in the prototype printed dipole cause an interesting amount of simulated and measured results. More precisely, the return loss measurements are presented in four groups of printed dipole antennas. Each of them corresponds to four dipoles that have the same value of w parameter, but also have different value of *l* parameter, ranging from 0 mm to 3 mm. The corresponding simulated results are presented in **Figures 3**, **4**, **5** and **6** respectively.

These curves provide that the return loss characteristics of the printed dipole are affected only by the value of l parameter. In fact, the resonance of them is independent of the value of *l* and *w* parameters. Moreover, in the frequency range of the resonance bandwidth the form of the curve becomes quite more flat as the value of *l* parameter increases. On the other hand, the length of w geometrical parameter does not affect the form of these curves. These observations are also indicated by the corresponding experimental results.

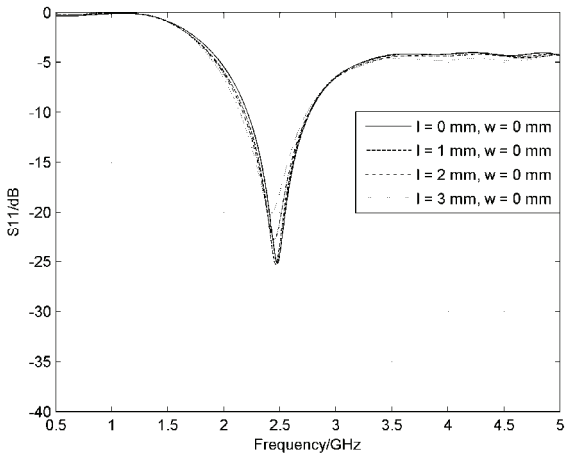

Figure 3. Simulated return loss of the printed dipole antenna for 4 *l* parameter values and for *w* parameter equals to 0 mm.

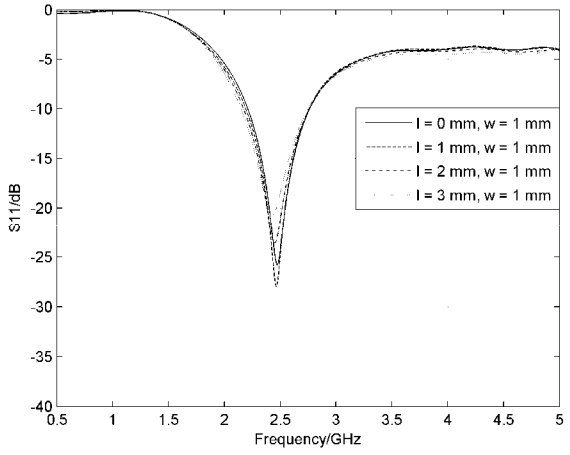

Figure 4. Simulated return loss of the printed dipole antenna for 4 *l* parameter values and for *w* parameter equals to 1 mm.

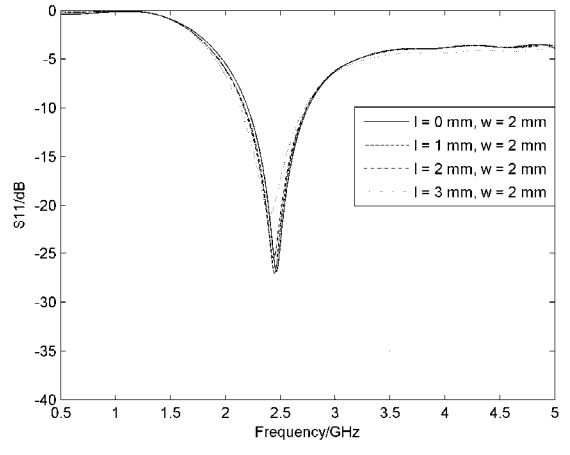

Figure 5. Simulated return loss of the printed dipole antenna for 4 *l* parameter values and for *w* parameter equals to 2 mm.

These are provided by a Network Analyzer and are also presented in **Figures 7**, **8**, **9** and **10**, respectively.

From these curves a relatively good agreement between the simulated and measured return loss was observed. For each value of *l* and *w* parameters the measured frequency point of minimum return loss is approximately 2.45GHz and the corresponding resonance bandwidth ranges from 2.20 GHz to 2.75 GHz. Another issue is that the experimental results of return loss presents a resonance point on frequency range of 4 GHz. This result is not in good agreement with the simulation results. This difference may be due to effects of coaxial–to–microstrip transition, included in the measurements but not taken into account in the simulated results. In addition, the impact of l and w parameters seems not to have important interest in the frequency range of 4 GHz.

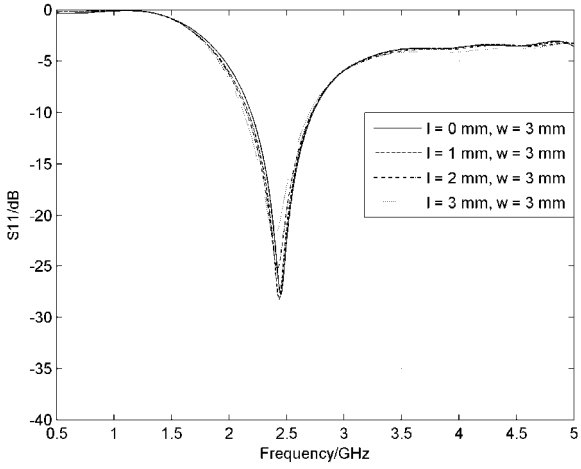

Figure 6. Simulated return loss of the printed dipole antenna for 4 *l* parameter values and for *w* parameter equals to 3 mm.

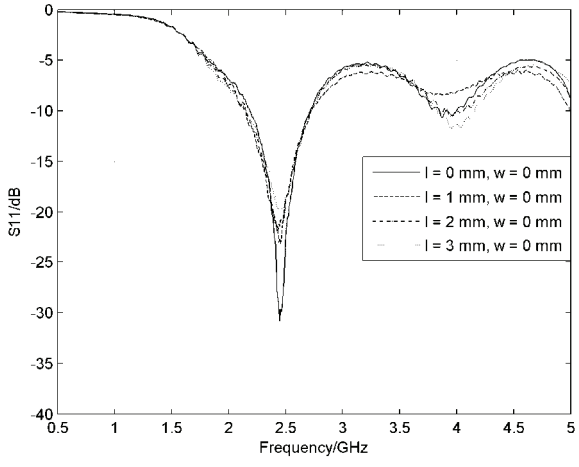

Figure 7. Measured return loss of the printed dipole antenna for 4 *l* parameter values and for *w* parameter equals to 0 mm.

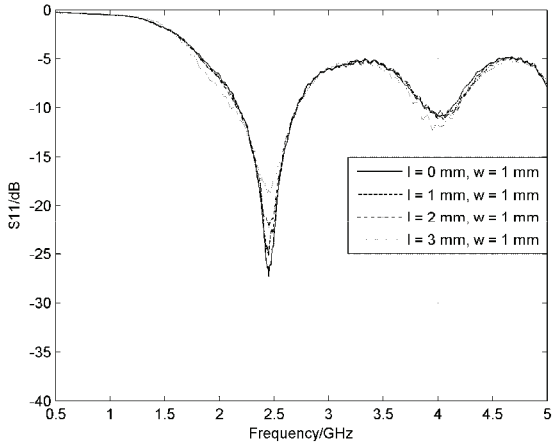

Figure 8. Measured return loss of thfde printed dipole antenna for 4 *l* parameter values and for *w* parameter equals to 1 mm.

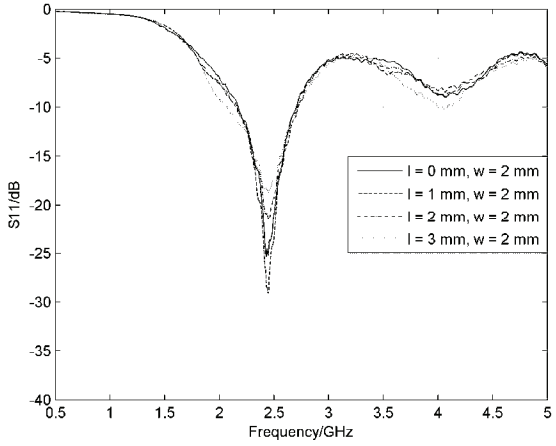

Figure 9. Measured return loss of the printed dipole antenna for 4 *l* parameter values and for *w* parameter equals to 2 mm.

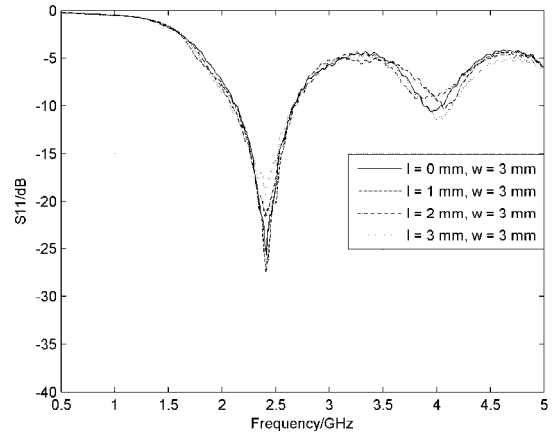

Figure 10. Measured return loss of the printed dipole antenna for 4 *l* parameter values and for *w* parameter equals to 3 mm.

On the other hand, both simulated and experimental return loss results indicate that as the value of l parameter increases, the shape of the corresponding curve becomes flat for wider frequency range but the frequency point of minimum remains quite stable, simultaneously. This observations shows that return loss may be demonstrated for a specific frequency range as parameter *l* is adjusted. Therefore, for better operation of printed dipole antenna at frequency point of interest, some of its geometric characteristics have to be modified. Both simulated and measured results indicate that a value of *l* parameter may be considered to be important to achieve efficient return loss measurements for the printed dipole antenna design. Instead, this observation for the w parameter does not exist. Return loss and resonance bandwidth seem to be independent of w parameter variation. **Figures 11** and **12** present the simulated and experimental results of return loss for *l* = 0 mm and w variation from 0 mm to 3 mm with step 1 mm. These curves confirm the corresponding independence.

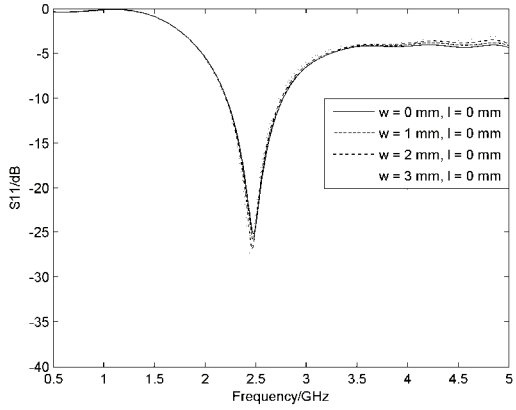

Figure 11. Simulated return loss of the printed dipole antenna for 4 *w* parameter values and for *l* parameter equals to 0 mm.

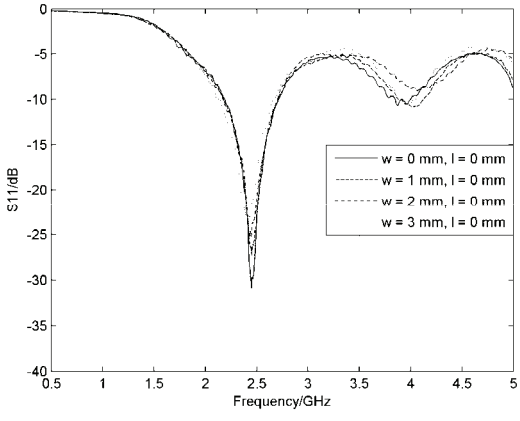

Figure 12. Measured return loss of the printed dipole antenna for 4 *w* parameter values and for *l* parameter equals to 0 mm.

Based on these criteria, the proposed investigation of *l* and *w* parameter offers a way to implement printed dipole antenna elements with the same geometric characteristics and without declinations between them on the return loss characteristics. This observation provides an attractive solution on antenna array implementations at modern wireless applications which are constituted by a specific number of usually same antenna elements. In fact, it is observed that as the resonance bandwidth becomes more flat and uniform, the agreement between the corresponding return loss figures of geometrically identical dipoles become more practicable and realized. From this, it is also provided that the *l* parameter is proposed to approximate the value of 2 mm, as an optimum value for better performance. These observations are also reinforced by the unchanged frequency range of the resonance bandwidth in each case.

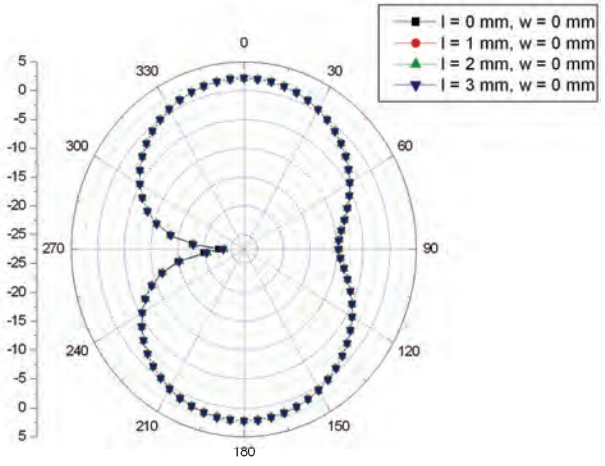

(a)

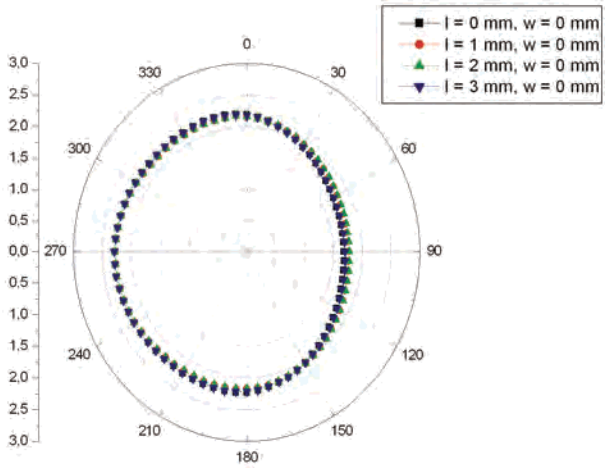

(b)

Figure 13. Simulation: Printed dipole antenna radiation patterns for 4 *l* parameter values and for *w* parameter equals to 0 mm, (a) E – plane, (b) H - plane.

Besides, the radiation patterns of printed dipole antennas as *l* and *w* parameters vary are also presented. **Figures 13**, **14**, **15** and **16** show these radiation diagrams

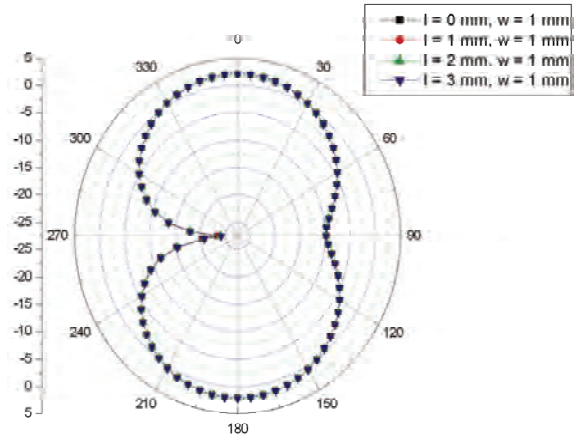

(a)

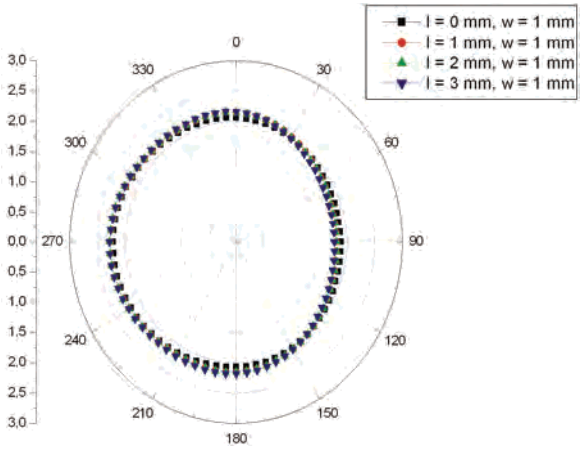

(b)

Figure 14. Simulation: Printed dipole antenna radiation patterns for 4 *l* parameter values and for *w* parameter equals to 1 mm, (a) E – plane, (b) H - plane.

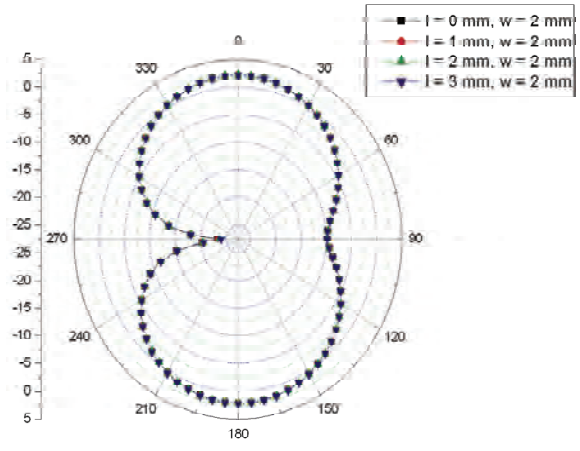

(a)

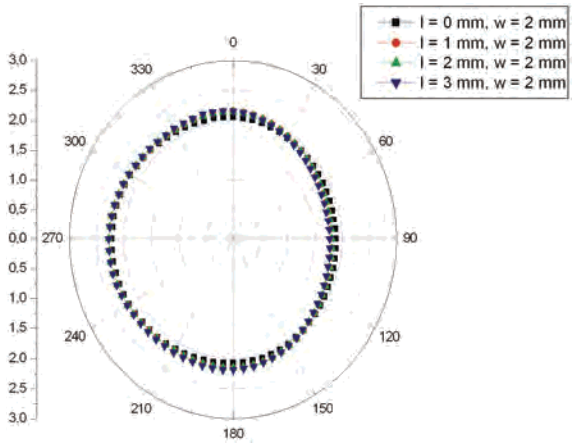

(b)

Figure 15. Simulation: Printed dipole antenna radiation patterns for 4 *l* parameter values and for *w* parameter equals to 2 mm, (a) E – plane, (b) H - plane.

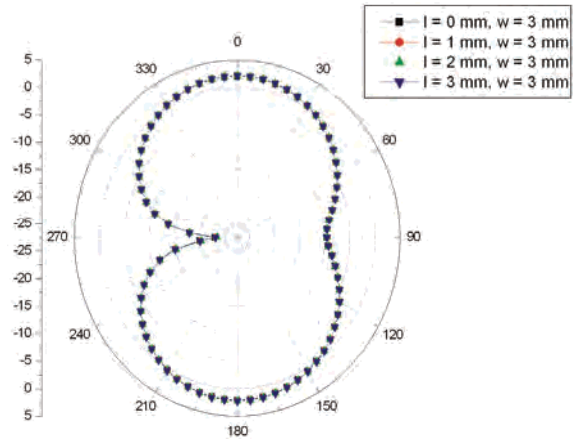

(a)

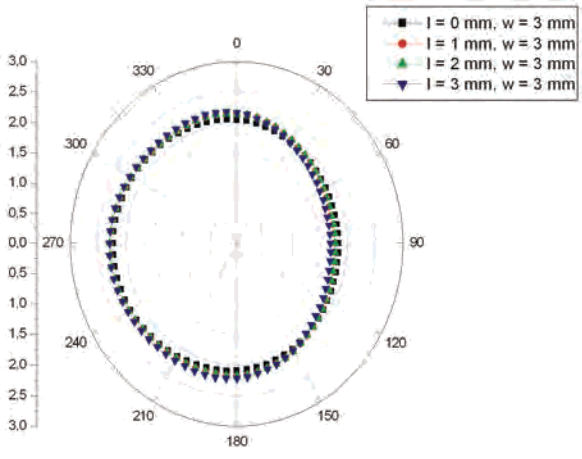

(b)

Figure 16. Simulation: Printed dipole antenna radiation patterns for 4 *l* parameter values and for *w* parameter equals to 3 mm, (a) E – plane, (b) H - plane.

at 2.45 GHz. Each of them corresponds to a defined value of w parameter and four different values of *l* parameter, too. From these figures, the corresponding results do not indicate differences as the radiation element remains the same (*w* = constant), so the values of *l* and *w* parameters do not affect the radiation characteristics of printed dipole antenna.

4. Conclusions

A printed dipole antenna with integrated balun is studied and investigated. The complete structure has implemented, simulated and experimentally measured for several values of *l* and *w* parameters. Good agreement between simulated and measured results on return loss and resonance bandwidth has been achieved. Simulated radiation pattern has also been specified for each value of l and w parameters. Return loss seems to be affected by the variation of *l* parameter, but resonance bandwidth and radiation diagram do not depend on it. Moreover, the w parameter variation on dipole's geometry does not provide changes on reflection coefficient values and polar curves of radiation pattern. A proposed value of *l* parameter is also specified for identical return loss characteristics among printed dipole antennas with similar geometry characteristics. In general, as the value of *l* increases, the return loss of the antenna becomes more flat for wider frequency range. This effect is crucial for innovator wireless communication engineering and especially antenna array design.

5. Acknowledgements

This research project (PENED) is co-financed by E. U.-European Social Fund (80%) and the Greek Ministry of Development-GSRT (20%).

6. References

[1] D. Edward and D. Rees, "A Broadband Printed Dipole with Integrated Balun," *Microwave Journal*, Vol. 30, No. 5, 1987, pp. 339-344.

[2] N. Michishita, H. Arai, M. Nakano, T. Satoh and T. Matsuoka, "FDTD Analysis for Printed Dipole Antenna with Balun," *Asia Pacific Microwave Conference*, Sydney, 2000, pp. 739-742.

[3] G. S. Hilton, C. J. Railton, G. J. Ball, A. L. Hume and M. Dean, "Finite–Difference Time–Domain Analysis of a Printed Dipole Antenna," 19*th International IEEE Antennas and Propagation Conference*, Eindhoven, 1995, pp. 72-75.

[4] H.-R. Chuang and L.-C. Kuo, "3-D FDTD Design Analysis of a 2.4 GHz Polarization–Diversity Printed Dipole Antenna with Integrated Balun and Polarization–

Switching Circuit for Wlan and Wireless Communication Application," *IEEE Transactions on Microwave Theory and Techniques*,Vol. 51, No. 2, 2003, pp. 374-381.

[5] C. Votis, V. Christofilakis and P. Kostarakis, "Geometry Aspects and Experimental Results of a Printed Dipole Antenna," *International Journal Communications, Network and System Sciences*, Vol. 3, No. 2, 2010, pp. 97-100.

[6] C. A. Balanis, "Antenna Theory Analysis and Design," Wiley Interscience, New York, 1997

[7] R. Garg, P. Bhartia, I. Bahl and A. Ittipiboon, "Microstrip Antenna Design Handbook," Artec House, Canton, 2001.

[8] D. M. Pozar, "Microwave Engineering," Wiley, New York, 1998.

Int. J. Communications, Network and System Sciences, **2010, 3, 441-445**
doi:10.4236/ijcns.2010.35058 Published Online May 2010 (http://www.SciRP.org/journal/ijcns/)

The Performance Improvement of BASK System for Giga-Bit MODEM Using the Fuzzy System

Ki-Hwan Eom[1], Kyo-Hwan Hyun[1], Kyung-Kwon Jung[2]
[1]*Department of Electronic Engineering, Dongguk University, Seoul, Korea*
[2]*Department of Electronic Engineering, Hanlim University, Chuncheun, Korea*
E-mail: *kihwanum@dongguk.edu*
Received August 21, 2009; *revised December* 15, 2009; *accepted March* 17, 2010

Abstract

In this paper we propose an automatic bandwidth control method for the performance improvement of Binary Amplitude Shift Keying (BASK) system for Giga-bit Modem in millimeter band. To improve the performance of the BASK system with a fixed bandwidth, the proposed method is to adjust a bandwidth of low pass filter in receiver using the fuzzy system. The BASK system consists of a high speed shutter of the transmitter and a counter and a repeater of receiver. The repeater consists of four stage converters, and a converter is constructed with a low pass filter and a limiter. The inputs to the fuzzy system are the reminder and integral of remainder of counter, and output is a bandwidth. We used a Viterbi algorithm to find the optimum detection from output of the counter. Simulation results show that the proposed system improves the performance compared to the fixed bandwidth.

Keywords: BASK, Giga-Bit MODEM, Bandwidth, Low Pass Filter, Fuzzy System

1. Introduction

The 60 GHz band still being free and unlicensed, a large bandwidth, for example of the order of 1 GHz, and easily be used. In digital modulation of the 60 GHz band, a problem is ISI (Inter Symbol Interference) [1]. Digital base band signals often are rectangular pulse train. When rectangular pulses are passed through a band limited channel, the pulses will spread in time, and the pulse for each symbol will smear into the time intervals of succeeding symbols. This causes ISI and leads to an increased probability of the receiver making an error in detecting a symbol. There are many methods to minimize ISI as likelihood sequence estimation, whitened matched filters and decision-feedback equalization [2]. One approach to minimizing ISI is to use pulse shaping techniques. The most popular pulse shaping filter used in mobile communications is the raised cosine filter. However, the maximum value of the RF waveform and raised cosine filtered pulses do not always match [2-4]. Also, in Heterodyne method, IF process is given gain of receiver, but an increase in analog conversion steps, the more the price will also increase. The BASK system consists of a high speed shutter and a mixer of the transmitter, and a counter and a repeater of the receiver for solves these problems. The high speed shutter of the transmitter is introduced for pulse shaping, which can minimize ISI. Using repeater for improve SNR and make rectangular pulse train. The repeater consists of few stage converters. A converter is constructed with a low pass filter and a limiter.

In this paper propose an automatic bandwidth control method for performance improvement of BASK system. Propose method is that adjust a bandwidth of low pass filter in receiver using the fuzzy logic system. The fuzzy logic system is normally used to formulate human knowledge, but here we create the membership functions and the fuzzy rule base by means of the simulation results. The inputs of the fuzzy logic system are the reminder and integral of remainder of counter, and output is bandwidth. We use 8 bit counter and Viterbi algorithm with soft decision. Rule base inference was accomplished using the max-min inference procedure. Defuzzification of the bandwidth output was achieved the center of gravity computation. In order to verify the effectiveness of the proposed method, simulations were performed by fixed bandwidth and BER.

2. BASK System with a Fixed Bandwidth

In millimeter wave band, BASK system with a fixed

bandwidth of Giga-bit MODEM without IF process using high speed shutter for pulse shaping of input signal and minimize ISI in the transmitter, and using repeater for improve SNR and make rectangular pulse train in receiver. **Figure 1** shows the block diagram of BASK system with a fixed bandwidth.

In the transmitter, RCS is raised cosine signal generator. The transmitter uses a high speed shutter that can truncate the side lobe of the raised cosine filter. A shutter performs switching window. The output of a shutter is given by

$$h_s(t) = \begin{cases} \sigma(t)\dfrac{\sin(\alpha\pi t / T_s)}{\pi t} & , \quad n = 1 \\ 0 & , \quad n = 0 \end{cases} \tag{1}$$

Where $\sigma(t)$ is a gain for the symbol period, α is the roll off factor, t is the time, T_S is the symbol period, and n is the state of the symbol. A shutter function is to make a constant envelope.

The receiver uses a repeater without IF (Intermediate Frequency) that consists of two stage converters. A converter is constructed with the LPF and the limiter. Design parameters of converters are bandwidth of the LPF (BLPF) and stiffness of the limiter (SL: Stiffest Limiter). The theoretical solution is given by

$$y_i(t) = SL(\mathbf{G}x_i(t)) \tag{2}$$

Where $\mathbf{G}x_i(t)$ is the input of the limiter, $y_i(t)$ is the output of the converter, SL is a transfer function of the limiter. The block diagram of a converter is shown in **Figure 2**.

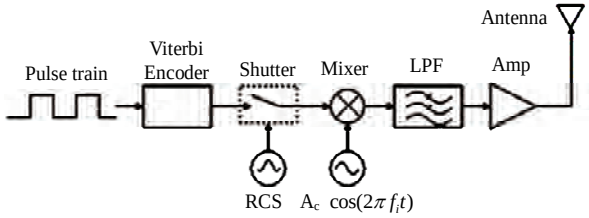

(a) The transmitter

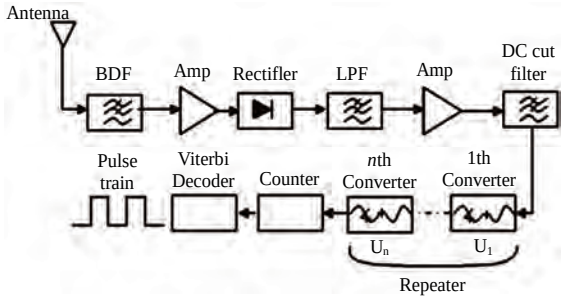

(b) The receiver

Figure 1. The block diagram of BASK system with a fixed bandwidth.

The repeater can improve signal-to-noise ratio (SNR), and make rectangular pulse train.

3. Proposed Method

The block diagram of proposed automatic bandwidth control is shown in **Figure 3**.

The proposed method is that adjust the bandwidth of low pass filter in receiver using a fuzzy logic system. The output of counter in receiver depends on the pattern sequence deeply, so we need the controls for the ranges of bandwidth to improve the performance of the system. The inputs to the fuzzy logic system are the remainder and integral of remainder of counter, and output is a bandwidth. In order to create the membership functions and fuzzy rule base, we simulated on reminder and integral of reminder of counter. The simulation results of the reminder and integral reminder of 8 bit counter is shown in **Figure 4**.

In **Figure 4**, we can study that the sum of reminder jumps if a big reminder happens in negative or positive. Therefore we apply the bandwidth control using the fuzzy logic system due to such situations.

The inputs are fuzzified according to the input membership functions and output membership functions in **Figures 5** and **6**.

The fuzzy rule-base consists of a total of 15 rules. The

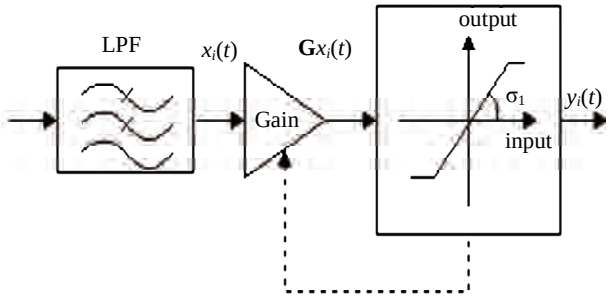

Figure 2. The block diagram of a converter.

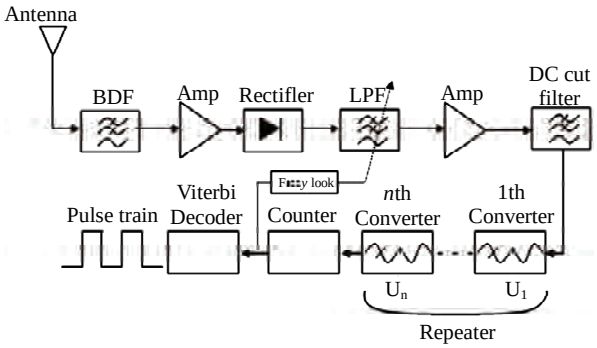

Figure 3. The block diagram of proposed bandwidth control system.

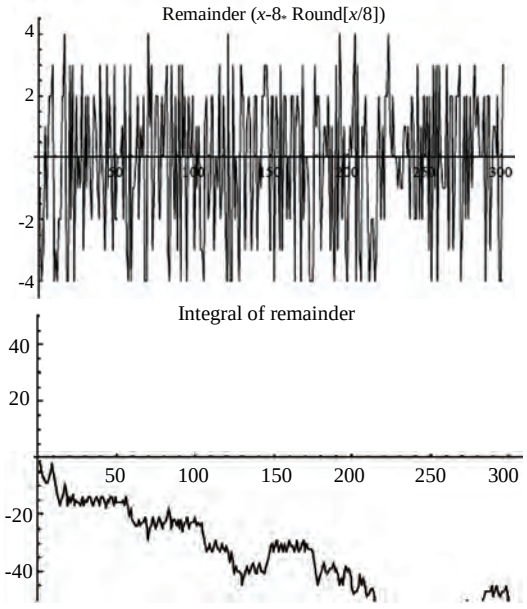

(a) Narrow bandwidth

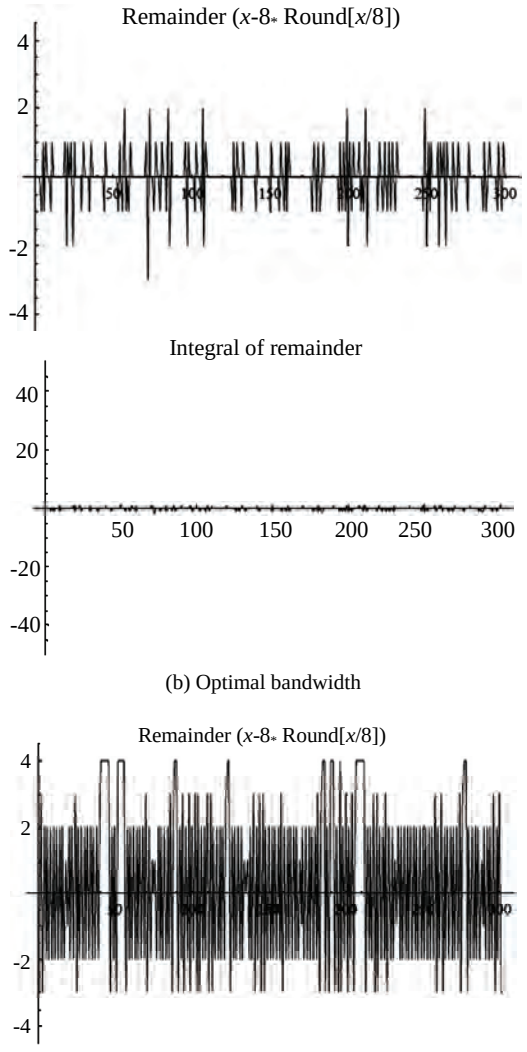

(b) Optimal bandwidth

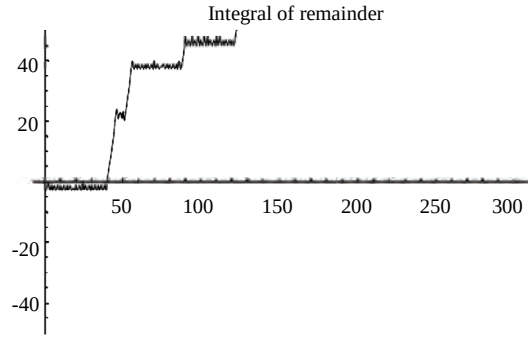

(b) Broad bandwidth

Figure 4. Simulation of counter for bandwidth control.

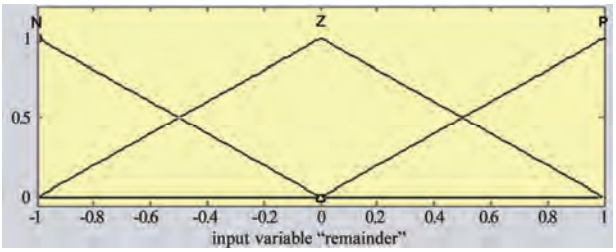

(a) Remainder

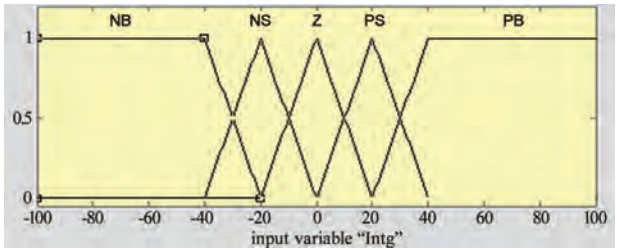

(b) Integral of remainder

Figure 5. The membership function of fuzzy input.

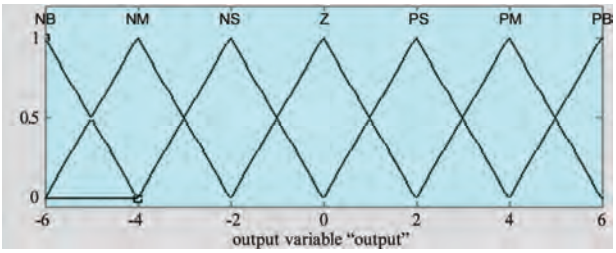

Figure 6. The membership function of fuzzy output.

input/output fuzzy relation is chosen on the basis of the simulation results as shown in **Table 1**.

In **Table 1**, R and IR are remainder and integral of remainder. Linguistic Variables are NB (Negative Big), NM (Negative Medium), NS (Negative Small), N (Negative), Z (Zero), P (Positive), PS (Positive Small), PM (Positive Medium) and PB (Positive Big).

Table 1. Fuzzy rules.

R \ IR	NB	NS	Z	PS	PB
N	PB	PM	PS	Z	NS
Z	PM	PS	Z	NS	NM
P	PS	Z	NS	NM	NB

Rule base inference was accomplished using the max-min inference procedure. Defuzzification of the bandwidth output was achieved the center of gravity computation [5].

4. Simulation

In order to verify the effectiveness of the proposed method, Simulations were performed using MATLAB. The carrier frequency was 60 GHz and message data rate was 1 Gbps. In order to improve SNR, it is better to change angle of limiter as $\theta_1 < \theta_2 < \theta_3 < \theta_4$, and these parameters are not required exact value. Viterbi algorithm parameters are constrain length k = 7, coding rate = 1/2, and generator polynominals for octal codes are 171, 133 [6].

Figure 7 shows the average BER for the signal prior to repeater and the signal posterior to repeater using Viterbi algorithm.

In **Figure 7**, SNR of non-shutter, the non-repeater, and the repeater is 31 dB, 30 dB, and 22 dB respectively when the BER is 10^{-3}.

Figure 8 shows the average BER for the fixed bandwidth and automatically controlled bandwidth by fuzzy logic system.

In **Figure 8**, the proposed automatic bandwidth control method by fuzzy logic system is improved the SNR about 8 dB at BER of 10^{-3} against the case of fixed bandwidth.

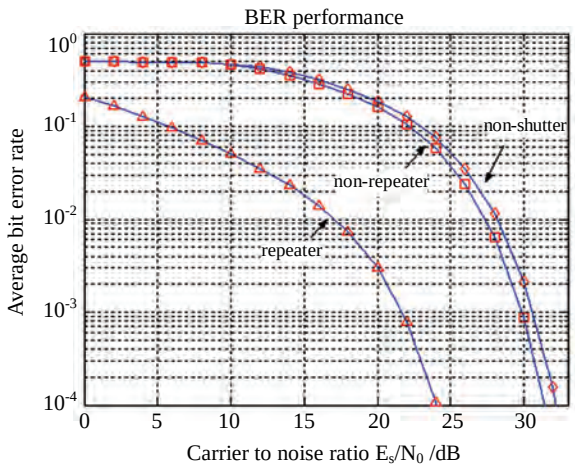

Figure 7. BER performance for the repeater.

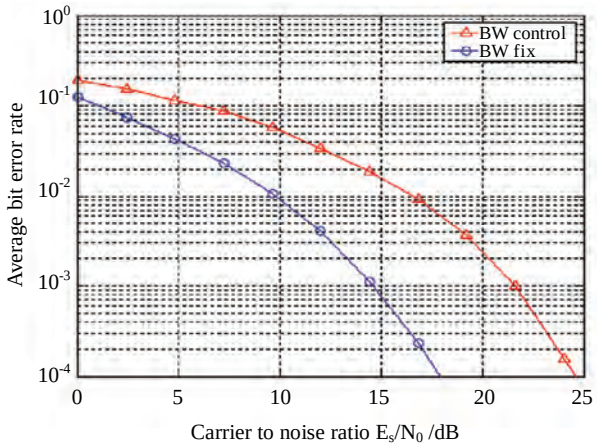

Figure 8. Simulation of BER performance.

5. Conclusions

In this paper proposed a method for improving the performance of the BASK system for automatically tuning the bandwidth of LPF. The BASK system was constructed a high speed shutter of transmitter and a repeater of receiver. The shutter was introduced for pulse shaping to improve the intersymbol interference and the repeater consists of few stage converters, and a converter was constructed with a low pass filter and a limiter. Proposed method was using fuzzy logic system. Fuzzy inputs were remainder and integral of remainder of counter. Output was bandwidth. In order to verify the effectiveness of the proposed method, simulations were performed by fixed bandwidth and BER. The simulation results are summarized as follows:

- Fuzzy System has 2 inputs, 1 output, 15 the number of fuzzy rules. So that can be configured simply.
- SNR of non-shutter, the non-repeater, and the repeater is 31 dB, 30 dB, 22 dB, respectively at BER of 10^{-3}.
- The proposed method is improved the SNR about 8 dB at BER of 10^{-3} against the case of fixed bandwidth.

6. References

[1] V. R. M. Thyagarajan, R. H. M. Hafez and D. D. Falconer, "Broadband Indoor Wireless Communication in (20 ~ 60) GHz Band: Signal Strength Considerations," *Universal Personal Communication*, Vol. 2, October 1993, pp. 894-899.

[2] T. S. Rappaport, "Wireless Communications," 2nd Edi-

tion, Prentice Hall, New Jersey, 2002.

[3] E. Lindskog and A. Paulraj, "A Transmit Diversity Scheme for Channels with Intersymbol Inference," *Proceedings of IEEE International Conference on Communications*, New Orleans, Vol. 1, June 2000, pp. 307-311.

[4] S. Haykin, "Communication Systems," 4th Edition, John Wiley Inc., Canada, 2000.

[5] R. Johnston, "Fuzzy Logic Control," *GEC Journal of Research*, Vol. 11, No. 2, 1994, pp. 99-109.

[6] M. Hosemann, R. Habendorf and G. P. Fettweis, "Hardware-Software Codesign of A 14.4 Mbit - 64 State - Viterbi Decoder for An Application-Specific Digital Signal Processor," *Proceedings of IEEE Workshop on Signal Processing Systems* 2003, Seoul, 27-29 August 2003, pp. 45-50.

Int. J. Communications, Network and System Sciences, **2010, 3, 446-452**
doi:10.4236/ijcns.2010.35059 Published Online May 2010 (http://www.SciRP.org/journal/ijcns/)

Analysis and Comparison of Time Replica and Time Linear Interpolation for Pilot Aided Channel Estimation in OFDM Systems

Donglin Wang
Department of Electrical and Computer Engineering, University of Calgary, Calgary, Canada
Email: *dowang@ucalgary.ca*
Received March 10, 2010; *revised April* 11, 2010; *accepted May* 12, 2010

Abstract

This paper analyzes and compares two time interpolators, *i.e.*, time replica and time linear interpolator, for pilot aided channel estimation in orthogonal frequency division multiplexing (OFDM) systems. The mean square error (MSE) of two interpolators is theoretically derived for the general case. The equally spaced pilot arrangement is proposed as a special platform for these two time interpolators. Based on this proposed platform, the MSE of two time interpolators at the virtual pilot tones is derived analytically; moreover, the MSE of per channel estimator at the entire OFDM symbol based on per time interpolator is also derived. The effectiveness of the theoretical analysis is demonstrated by numerical simulation in both the time-invariant frequency-selective channel and the time varying frequency-selective channel.

Keywords: OFDM, Channel Estimation, Time Replica, Time Linear Interpolation, Virtual Pilots

1. Introduction

Orthogonal frequency division multiplexing (OFDM) [1-3] has been widely used in high-speed wireless communication systems, such as broadband wireless local area networks (WLANs) [4], wireless metropolitan area networks (WMANs) [5] and worldwide interoperability for microwave access (WIMAX) [6], due to its advantages of transforming frequency-selective fading channels into a set of parallel flat fading sub-channels and eliminating inter-symbol interference [7].

Channel estimation is one of the most essential tasks in compensating distortion from channels and performing coherent detection in OFDM systems. Estimation is usually performed by using pilot tones [8, 9] and is based on inserting known pilot tones in each OFDM symbol, where interpolation in time-frequency grid [10] plays an important role in the estimation process. The usage of virtual pilot tones [11-13] and time interpolation can reduce the redundancy and guarantee a higher transmission bit rate. Among time interpolation methods, time replica [14, 15] is widely used in time-invariant or slow time-varying channel, which is simple to implement and also efficient for subcarrier usage; time linear interpolation [16-18] is widely used in slow or fast time-varying channel, because it is simple to realize and usually can give a satisfactory performance. However, some interesting questions are raised as follows: 1) what kind of time-varying channel is slow enough to utilize time replica? 2) Conversely, what kind of time-varying channel is so fast that we have to employ time linear interpolation instead of time replica? And 3) how much does time linear interpolation perform better than time replica by for a time-invariant channel?

To answer these questions above, this paper analyzes and compares the performances of time replica and time linear interpolator in both the time-invariant frequency-selective channel and the time varying frequency-selective channel. The MSE of both time interpolators is theoretically derived for the general cases. The equal spaced pilot arrangement is employed as a special platform for both time interpolators, where the positions of virtual pilot tones in one OFDM symbol correspond to those of pilot tones of its last and next OFDM symbols. Channel state information (CSI) [19] at pilot tones is estimated by least square (LS) estimator. CSI at virtual pilot tones in one OFDM symbol is obtained by either of time interpolators, where time replica is to completely replicate the CSI at pilot tones of its last OFDM symbol while time linear interpolator is to linearly interpolate values by using the estimated CSI at the corresponding pilot tones of both its last and next OFDM symbols. CSI at data

tones is finally obtained by frequency linear interpolation [20].

This paper is organized as follows. In Section 2, the MSEs of two interpolators, *i.e.*, time replica and time linear interpolation, are theoretically derived for the general case. In Section 3, the equally spaced pilot arrangement is proposed as a special platform for analyzing these two time interpolators. In Section 4, based on the proposed platform, the MSE of two time interpolators at the virtual pilot tones is derived analytically; moreover, the MSE of channel estimators at the entire OFDM symbol based on these two time interpolators is also derived, respectively. Numerical results are reports in Section 5, followed by conclusion in Section 6.

Notation: $|\mathbf{g}|^2$ denotes the modulus. $\|\mathbf{g}\|^2$ is the 2-norm operation. $E_k\{\mathbf{g}\}$ is the expectation operation on k. $E_{k,l}\{\mathbf{g}\}$ means the expectation on both k and l. $Var_k\{\mathbf{g}\}$ means the variance on k. $d_{m-i,m+j}(k)$ denotes the variation of the CSI of the kth tone from the $(m-i)$th OFDM symbol to the $(m+j)$th OFDM symbol. $d_m(k)$ denotes the variation of the CSI of the kth tone from the mth OFDM symbol to the $(m+1)$th OFDM symbol. $e_m^R(k)$ and $e_m^L(k)$ are the channel estimation errors of the mth OFDM symbol at the kth tone where time replica or time linear interpolation are employed for CSI estimation at the virtual pilot tones, respectively.

2. MSE of Two Time Interpolators

Assume that each OFDM symbol has N subcarriers where pilots occupy P subcarriers. Denote the set of pilot tones by I_P. By LS estimation, the CSI at pilot tones in the m^{th} OFDM symbol can be obtained as

$$\hat{H}_m(k)=\frac{Y_m(k)}{X_m(k)} \tag{1}$$

where $X_m(k)$ and $Y_m(k)$ are the transmitted and received pilots of the mth OFDM symbol, respectively. Assuming the pilot tones $X_m(k)=1$ for convenience of analysis, we have

$$\hat{H}_m(k)=H_m(k)+W_m(k) \tag{2}$$

where $H_m(k)$ represents the true value and $W_m(k)$ is a complex-valued sample of additive white Gaussian noise (AWGN) process at the mth OFDM symbol, $W_m(k)\sim CN(0,s^2)$.

Assuming that along the time axis in **Figure 1**, the data tones in the m^{th} OFDM symbol correspond to the pilot tones in both the $(m-p)$th and the $(m+q)$th OFDM symbol, the CSI at the data tones in the mth OFDM symbol can be obtained by time interpolation by using the estimated CSI at the pilot tones of both the $(m-p)$th and the $(m+q)$th OFDM symbol, which is thus called the virtual pilot tones. Denote the set of virtual tones by I_{PP}. In this section, we will analyze and compare the MSE performance of two time interpolators: time replica and time linear interpolator.

2.1. Time Replica

Time replica at the virtual pilot tones in the mth symbol is to replicate the CSI at the pilot tones in the $(m-p)$th symbol,

$$\hat{H}_m(k)=\hat{H}_{m-p}(k),\qquad k\in I_{PP}\ . \tag{3}$$

By (2) and (3), the estimation error of time replica at the kth tone can be expressed as

$$\begin{aligned} e_m^R(k)&=\hat{H}_{m-p}(k)-H_m(k)\\ &=H_{m-p}(k)-H_m(k)+W_{m-p}(k). \end{aligned} \tag{4}$$

The MSE using time replica can thus be obtained as

$$\begin{aligned} x_R&=E_k\left\{\left\|e_m^R(k)\right\|^2\right\}=E_k\left\{\left\|H_{m-p}(k)-H_m(k)\right\|^2\right\}+s^2\\ &=E_k\left\{\left\|d_{m-p,m}(k)\right\|^2\right\}+s^2. \end{aligned} \tag{5}$$

2.2. Time Linear Interpolation

However, if using time linear interpolation, the estimated CSI can be obtained as follows,

$$\hat{H}_m(k)=\frac{p}{p+q}\hat{H}_{m-p}(k)+\frac{q}{p+q}\hat{H}_{m+q}(k) \tag{6}$$

for $k\in I_{PP}$. By (2) and (6), the estimation error of time linear interpolation at the k^{th} tone can be expressed as

$$\begin{aligned} e_m^L(k)&=\frac{p}{p+q}\left(H_{m-p}(k)-H_m(k)\right)+\frac{q}{p+q}W_{m-p}(k)\\ &=\frac{p}{p+q}\left(H_{m+q}(k)-H_m(k)\right)+\frac{q}{p+q}W_{m+q}(k). \end{aligned} \tag{7}$$

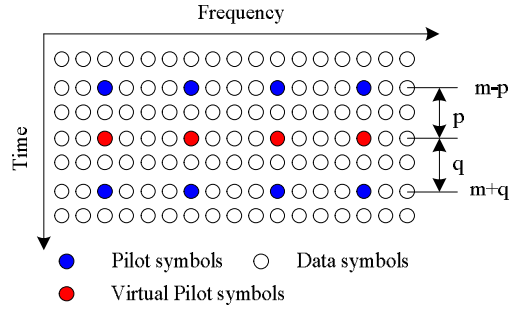

Figure 1. The virtual pilot tones in the mth OFDM symbol are time-interpolated by using the pilot tones at both the $(m-p)$th and the $(m+q)$th OFDM symbol.

Based on (7), the MSE of time linear interpolation can thus be obtained as

$$x_L = E_k\left\{\left\|e_m^L(k)\right\|^2\right\} = E_k\left\{\left\|\frac{pd_{m-p,m}(k)}{p+q} - \frac{qd_{m,m+q}(k)}{p+q}\right\|^2\right\} + \frac{p^2+q^2}{(p+q)^2}s^2. \quad (8)$$

2.3. Comparison

Subtracting (8) from (6), the difference between x_R and x_L can be expressed as

$$x_R - x_L = E_k\left\{\left\|d_{m-p,m}(k)\right\|^2\right\} + \frac{2pq}{(p+q)^2}s^2 - E_k\left\{\left\|\frac{pd_{m-p,m}(k)}{p+q} - \frac{qd_{m,m+q}(k)}{p+q}\right\|^2\right\}. \quad (9)$$

From (9), one can conclude that

1) In a time-invariant frequency-selective channel, x_L is always lower than x_R by $10\log\frac{(p+q)^2}{2pq}$ dB; while in a time-variant frequency-selective channel, the performance comparison depends on the specific channel variation;

2) Considering a real-valued channel variation, in low noise environment, when $d_{m-p,m}(k)d_{m,m+q}(k) < 0$ and $\left|d_{m,m+q}(k)\right| > \left|d_{m-p,m}(k)\right|$, $x_R < x_L$;

3) Considering a real-valued channel variation, in noisy environment, when $d_{m-p,m}(k)d_{m,m+q}(k) \geq 0$ or $d_{m-p,m}(k)d_{m,m+q}(k) < 0$ but $\left|d_{m,m+q}(k)\right| < \left|d_{m-p,m}(k)\right|$, $x_R > x_L$.

3. Special Case: Pilot Arrangement and Channel Estimators

Assume that each OFDM symbol has N subcarriers where pilots occupy P subcarriers and virtual pilots superimposed with data samples also occupy P subcarriers. **Figure 2** shows the proposed pilot arrangement as a platform, which is a special case but not loss of generality, where along frequency axis, the pilot spacing is $2L$ and the spacing between pilot and adjacent virtual pilot is L. From **Figure 2**, one can see that along time axis, the pilot spacing is 2 and the spacing between pilot and adjacent virtual pilot is 1. Also, by LS estimation, the CSI at pilot tones can be obtained by (1).

3.1. Time Interpolation at Virtual Pilot Tones

Denote the set of virtual tones by I_{PP}. The CSI at virtual pilot tones is obtained by time interpolation. In this special pilot arrangement, since the virtual pilot tones at the mth symbol corresponds to the pilot tones at the $(m-1)$th symbol, time replica at the virtual pilot tones in one symbol is to replicate the CSI at the pilot tones of its last symbol,

$$\hat{H}_m(k) = \hat{H}_{m-1}(k), \quad k \in I_{PP}. \quad (10)$$

On the other hand, if using time linear interpolation, we can get

$$\hat{H}_m(k) = \frac{\hat{H}_{m-1}(k) + \hat{H}_{m+1}(k)}{2}, \quad k \in I_{PP}. \quad (11)$$

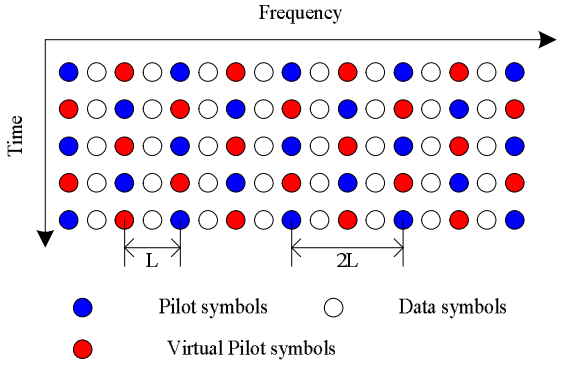

Figure 2. The proposed pilot arrangement as a special platform, where the pilot tones in one OFDM symbol correspond to the virtual pilot tones in its adjacent OFDM symbol.

3.2. Frequency Interpolation at Data Tones

Denote the set of data tones as I_D. Using frequency linear interpolation [20], the CSI at the whole OFDM symbol can be expressed as

$$\hat{H}_m(k+l) = \begin{cases} \frac{L-l}{L}\hat{H}_m(k) + \frac{l}{L}\hat{H}_m(k+L) \\ \qquad when \;\; 1 \leq k \leq 1+L(2P-2) \\ \hat{H}_m(k) \\ \qquad when \;\; k = 1+L(2P-1). \end{cases} \quad (12)$$

where $(k+l) \in I_D$, $k \in I_P \cup I_{PP}$, $1 \leq l \leq L-1$. Note that the CSI for data tones located on the right side beyond the $(1+PL)$th pilot/virtual pilot tone is decided by the edge interpolation.

4. Performance Analysis for the Special Case

This section analyzes the performance of this special case in terms of the MSEs of time interpolators and the MSEs of the corresponding channel estimators.

4.1. MSE of Time Interpolators

For this special case, the MSE of time replica in (5) becomes

$$x_R = E_k\left\{\left\|d_{m-1}(k)\right\|^2\right\} + s^2. \tag{13}$$

On the other hand, the MSE of time linear interpolation in (8) becomes

$$x_L = E_k\left\{\left\|\frac{d_{m-1}(k)-d_m(k)}{2}\right\|^2\right\} + s^2. \tag{14}$$

So, based on (13) and (14), the difference between x_R and x_L can be obtained as follows,

$$x_R - x_L = E_k\left\{\left\|d_{m-1}(k)\right\|^2\right\} + \frac{1}{2}s^2 - E_k\left\{\left\|\frac{d_{m-1}(k)-d_m(k)}{2}\right\|^2\right\}. \tag{15}$$

And, from (15), one can conclude that 1) in a time-invariant frequency-selective channel, x_L is always lower than x_R by 3 dB; in a time-variant frequency-selective channel, the performance difference depends on the specific channel variation; 2) in most situations, as the general case in (9), $x_R > x_L$, *i.e.*, time linear interpolation is better than time replica.

4.2. MSE of Channel Estimation

4.2.1. Time Replica

By LS estimation on pilot tones, time replica on virtual pilot tones and frequency interpolation on data tones, the corresponding MSE of channel estimation can be expressed as

$$x_{LRL} = \frac{P}{N}x_P + \frac{P}{N}x_R + \frac{N-2P}{N}x_{RF}, \tag{16}$$

where x_P is the MSE of LS estimation and x_{RF} is the MSE of frequency interpolation when using time replica at virtual pilot tones.

As an average of both odd and even OFDM symbols, except for the right side $(L-1)$ tones using the edge interpolation, a half of other data tones with the index $(k+l)\in I_D$ have $k\in I_P$ while $(k+L)\in I_{PP}$ for frequency linear interpolation; for the remaining data tones, $k\in I_{PP}$ while $(k+l)\in I_P$ for frequency linear interpolation. Hence, using (12), we can get x_{RF} in (17), where $e_F(k+l) = \frac{L-l}{L}H_m(k) + \frac{l}{L}H_m(k+L) - H_m(k+l)$, $k\in I_P\cup I_{PP}$, $1\le k\le 1+L(2P-2)$, and $e_F(1+L(2P\text{-}1)+l) = H_m(1+L(2P\text{-}1)) - H_m(1+L(2P\text{-}1)+l)$, are the inherent errors by frequency interpolation, x_F is the inherent MSE of frequency interpolation.

By substituting (17) into (16), x_{LRL} can be expressed as the following (18),

$$\begin{aligned} x_{RF} &= E_{k,l}\left\{\left\|\hat{H}_m(k+l) - H_m(k+l)\right\|^2\right\} = \\ &\frac{1}{2}\left(1-\frac{L-1}{N-2P}\right)E_{k,l}\left\{\left\|e_F(k+l)+\frac{L-l}{L}W_m(k)+\frac{l}{L}d_{m-1}(k)\right\|^2\right\} \\ &+\frac{1}{2}\left(1-\frac{L-1}{N-2P}\right)E_{k,l}\left\{\left\|e_F(k+l)+\frac{l}{L}W_m(k)+\frac{L-l}{L}d_{m-1}(k)\right\|^2\right\} \\ &+\frac{L-1}{N-2P}E_l\left\{\left\|e_F(1+L(2P-1)+l)\right\|^2\right\} = x_F \\ &+\frac{2L-1}{6L}\left(1-\frac{L-1}{N-2P}\right)s^2 \\ &+\frac{2L-1}{6L}\left(1-\frac{L-1}{N-2P}\right)E_k\left\{\left\|d_{m-1}(k)\right\|^2\right\}, \end{aligned} \tag{17}$$

$$\begin{aligned} x_{LRL} &= \frac{P}{N}x_P + \frac{P}{N}x_R + \frac{N-2P}{N}x_F \\ &+\frac{(2L-1)(N-2P-L+1)}{6NL}\left[s^2 + E_k\left\{\left\|d_{m-1}(k)\right\|^2\right\}\right]. \end{aligned} \tag{18}$$

4.2.2. Time Linear Interpolation

By LS estimation on pilot tones, time linear interpolation on virtual pilot tones and frequency interpolation on data tones, the MSE of channel estimation can be expressed as

$$x_{LLL} = \frac{P}{N}x_P + \frac{P}{N}x_R + \frac{N-2P}{N}x_{LF}, \tag{19}$$

where x_{LF} is the MSE of frequency interpolation when using time linear interpolation at virtual pilot tones. Using (12), x_{LF} can be obtained as shown in (20).

Substituting (20) into (19), x_{LLL} can be expressed as the following (21),

$$\begin{aligned} x_{LF} &= E_{k,l}\left\{\left\|\hat{H}_m(k+l) - H_m(k+l)\right\|^2\right\} = \\ &\frac{1}{2}\left(1-\frac{L-1}{N-2P}\right) \\ &E_{k,l}\left\{\left\|e_F(k+l)+\frac{L-l}{L}W_m(k)+\frac{l}{L}\frac{d_{m-1}(k)-d_m(k)}{2}\right\|^2\right\} \\ &+\frac{1}{2}\left(1-\frac{L-1}{N-2P}\right) \\ &E_{k,l}\left\{\left\|e_F(k+l)+\frac{l}{L}W_m(k)+\frac{L-l}{L}\frac{d_{m-1}(k)-d_m(k)}{2}\right\|^2\right\} \\ &+\frac{L-1}{N-2P}E_l\left\{\left\|e_F(1+L(2P-1)+l)\right\|^2\right\} = \end{aligned}$$

$$x_F + \frac{2L-1}{6L}\left(1-\frac{L-1}{N-2P}\right)s^2 + \frac{2L-1}{6L}\left(1-\frac{L-1}{N-2P}\right)E_k\left\{\left\|\frac{d_{m-1}(k)-d_m(k)}{2}\right\|^2\right\}. \quad (20)$$

$$x_{LLL} = \frac{P}{N}x_P + \frac{P}{N}x_R + \frac{N-2P}{N}x_F + \frac{(2L-1)(N-2P-L+1)}{6NL}\left[s^2 + E_k\left\{\left\|\frac{d_{m-1}(k)-d_m(k)}{2}\right\|^2\right\}\right]. \quad (21)$$

4.2.3. Comparison

Subtracting (21) from (18), the difference between x_{LRL} and x_{LLL} can be obtained as

$$x_{LRL} - x_{LLL} = \frac{P}{2N}s^2 + \left(\frac{P}{N} + \frac{(2L-1)(N-2P-L+1)}{6NL}\right) \times \left[E_k\left\{\|d_{m-1}(k)\|^2\right\} - E_k\left\{\left\|\frac{d_{m-1}(k)-d_m(k)}{2}\right\|^2\right\}\right]. \quad (22)$$

From (22), one can notice that

1) Since $N >> P$, $\frac{P}{2N}s^2$ is negligible and the differential MSE using (22) is approximately independent with noise;

2) In a time-invariant frequency-selective channel, x_{LRL} is approximately equal to x_{LLL}; while in a time-variant frequency-selective channel, the performance comparison depends on the specific channel variation;

3) Considering a real-valued channel variation, in low noise environment, when $d_m(k)d_{m-1}(k) < 0$ and $|d_m(k)| > |d_{m-1}(k)|$, $x_{LRL} < x_{LLL}$;

4) $|x_{LRL} - x_{LLL}| < |x_R - x_L|$.

5. Numerical Results

The OFDM system under consideration is with N = 512 subcarriers, and $2L$ = 8 equispaced pilot tones in each symbol. The length of cyclic prefix is 32. The interpolation distances $p = q = 1$. The modulation is QPSK. The pilot tones are all 1. For $0 \le j \le 63$, in the odd OFDM symbols, the pilot is inserted at the $(1+8j)$th tone; while in the even OFDM symbols, the pilot is inserted at the $(5+8j)$th tone. The six-ray multipath Rayleigh fading channel is considered. The average power delay profile is selected as

$$l_l = \exp(-l) \Big/ \sum_{l=0}^{5} l_l, \quad 0 \le l \le 5. \quad (23)$$

Figure 3 shows the MSE performance of time interpolator and channel estimation in the time-invariant frequency-selective channel, where one can see that time linear interpolator generating less noise has a 3 dB lower MSE than time replica at the virtual pilot tones. However, for the corresponding channel estimation at the whole OFDM tones, time linear interpolator performs similarly to time replica due to a negligible noise.

Figure 4 shows the MSE performance in a time varying channel where the parameters are $E_k\{d_{m-1}(k)\} = 0.001$, $Var_k\{d_{m-1}(k)\} = 10^{-6}$, $E_k\{d_m(k)\} = -0.002$, and $Var_k\{d_m(k)\} = 10^{-6}$, respectively. For interpolation at virtual pilot tones, when $SNR \le 25$ dB, time linear interpolator performs better than time replica due to better noise reduction; when SNR > 25 dB, time replica, which guarantees a more accurate interpolation in a low noise environment, performs better than linear interpolator. While for the corresponding channel estimation, when $SNR \le 25$ dB, time linear interpolator performs very similarly to time replica due to better noise reduction; when SNR > 25 dB, time replica also performs better than time linear interpolator.

Figure 5 shows the MSE performance in the time varying channel where the parameters are $E_k\{d_{m-1}(k)\}$

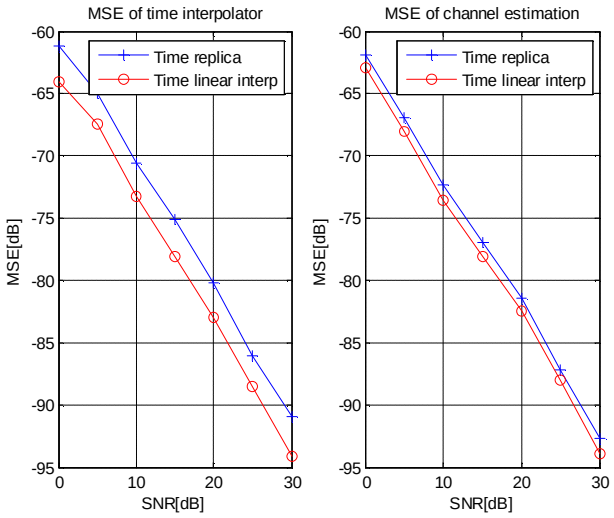

Figure 3. MSE of time interpolator and channel estimation in time-invariant frequency-selective channel.

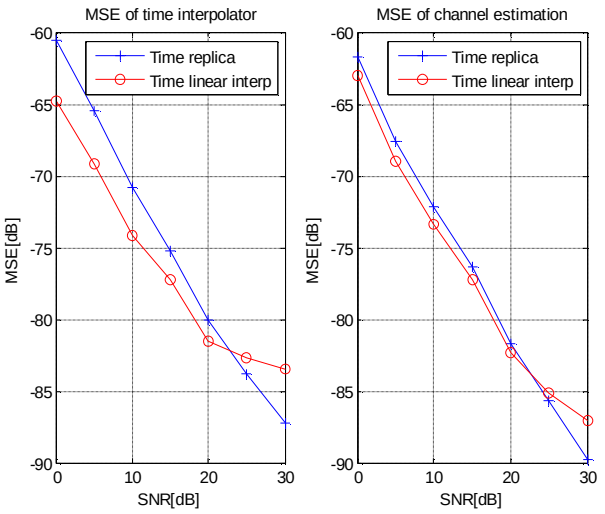

Figure 4. MSE of time interpolator and channel estimation in time-variant frequency-selective channel, where the expectation is equal to $E_k\{d_{m-1}(k)\} = 0.001$, the variance is equal to $Var_k\{d_{m-1}(k)\} = 10^{-6}$, the expectation $E_k\{d_m(k)\} = -0.002$, and variance $Var_k\{d_m(k)\} = 10^{-6}$, respectively, $0 \le k \le 512$.

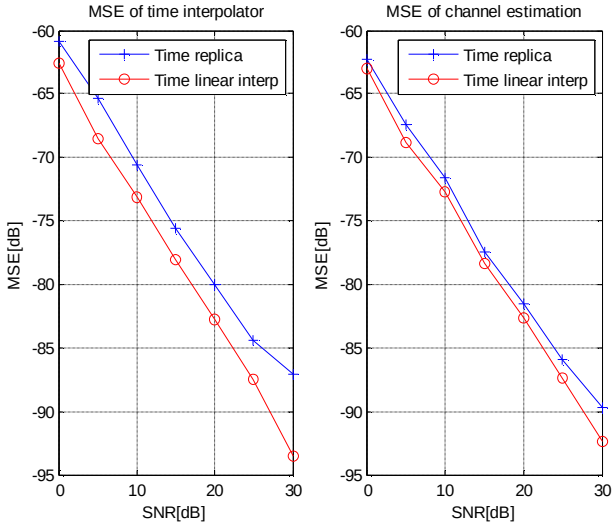

Figure 5. MSE of time interpolator and channel estimation in time-variant frequency-selective channel, where the expectation is equal to $E_k\{d_{m-1}(k)\} = 0.001$, the variance is equal to $Var_k\{d_{m-1}(k)\} = 10^{-6}$, the expectation $E_k\{d_m(k)\} = 0.002$, and variance $Var_k\{d_m(k)\} = 10^{-6}$, respectively, $0 \le k \le 512$.

$= 0.001$, $Var_k\{d_{m-1}(k)\} = 10^{-6}$, $E_k\{d_m(k)\} = 0.002$, and $Var_k\{d_m(k)\} = 10^{-6}$, respectively. Time linear interpolator always performs better than time replica for both interpolation at the virtual pilot tones and the corresponding channel estimation at the entire tones.

6. Conclusions

Time replica and time linear interpolation were analyzed and compared, especially under our proposed pilot arrangement. The MSEs of both time interpolators were derived analytically for both interpolations at the virtual pilot tones and their corresponding channel estimation at the entire OFDM symbol. Numerical simulation results were demonstrated to reach an agreement with theoretical analysis. From the given results, one can see that, in a time-invariant frequency-selective channel, when the interpolation distances $p = q = 1$, time linear interpolator has a 3 dB lower MSE than replica at the virtual pilot tones while they provide a similar performance at the entire OFDM symbol. Moreover, one can also see that, in a time varying frequency-selective channel, time linear interpolator outperforms time replica except the case, in a low noise environment, the CSI variation from the last OFDM symbol to the present symbol is negative to and has a smaller absolute value than that from the present symbol to the following symbol.

7. Acknowledgements

The author would like to thank all the anonymous reviewers of the paper. The critical comments by all the reviewers have helped us to improve the quality of our paper.

8. References

[1] M. Engels, "Wireless OFDM Systems," Kluwer Academic Publishers, New York, 2002.

[2] L. Hanzo, "OFDM and MC-CDMA: a Primer," John Wiley & Sons, Inc., Hoboken, 2006.

[3] H. Schulze, "Theory and Applications of OFDM and CDMA: Wideband Wireless Communications," John Wiley & Sons, Inc., Hoboken, 2005.

[4] B. Bing, "Wireless Local Area Networks: The New Wireless Revolution," Wiley-Interscience, New York, 2002.

[5] S. Methley, "Essentials of Wireless Mesh Networking," Cambridge University Press, Cambridge, 2009.

[6] M. Ma, "Current Technology Developments of Wimax Systems," Springer Verlag, New York, 2009.

[7] C. Pandana, Y. Sun and K. J. R. Liu, "Channel-Aware Priority Transmission Scheme Using Joint Channel Estimation and Data Loading for OFDM Systems," *IEEE Transactions on Signal Processing*, Vol. 53, No. 8, August 2005, pp. 3297-3310.

[8] R. Negi and J. Cioffi, "Pilot Tone Selection for Channel Estimation in a Mobile OFDM System," *IEEE Transactions on Consumer Electrononics*, Vol. 44, No. 3, August 1998, pp. 1122-1128.

[9] W. Zhang, X.-G. Xia and P. C. Ching, "Clustered Pilot Tones for Carrier Frequency Offset Estimation in OFDM Systems," *IEEE Transactions on Wireless Communications*, Vol. 6, No. 1, 2007, pp. 101-109.

[10] X. D. Dong, W.-S. Lu and A. C. K. Soong, "Linear Interpolation in Pilot Symbol Assisted Channel Estimation for OFDM," *IEEE Transactions on Wireless Communications*, Vol. 6, No. 5, May 2007, pp. 1910-1920.

[11] I. Budiarjo, I. Rashad and H. Nikookar, "On the Use of Virtual Pilots with Decision Directed Method in OFDM Based Cognitive Radio Channel Estimation Using 2x1-D Wiener Filter," *Proceedings of IEEE International Conference on Communications*, Beijing, May 2008, pp. 703-707.

[12] Q. F. Huang, M. Ghogho and S. Freear, "Pilot Design for MIMO OFDM Systems with Virtual Carriers," *IEEE Transactions on Signal Processing*, Vol. 57, No 5, May 2009, pp. 2024-2029.

[13] J. H. Zhang, W. Zhou, H. Sun and G.Y. Liu, "A Novel Pilot Sequences Design for MIMO OFDM Systems with Virtual Subcarriers," *Proceedings of Asia-Pacific Conference on Communications*, Perth, 2007, pp. 501-504.

[14] R. Prasad, "OFDM for Wireless Communications Systems," Artech House, Boston, 2004.

[15] A. R. S. Bahai, "Multi-Carrier Digital Communications," Springer Verlag, New York, 2004.

[16] K. Jihyung, P. Jeongho and H. Daesik, "Performance Analysis of Channel Estimation in OFDM Systems," *IEEE Signal Processing Letters*, Vol. 12, No. 1, January 2005, pp. 60-62.

[17] P. Jeongho, K. Jihyung, P. Myonghee, K. Kyunbyoung, K. Changeon and H. Daesik, "Performance Analysis of Channel Estimation for OFDM Systems with Residual Timing Offset," *IEEE Transactions on Wireless Communications*, Vol. 5, No. 7, July 2006, pp. 1622-1625.

[18] H. Myeongsu, Y. Takki, K. Jihyung and K. Kyungchul, "OFDM Channel Estimation With Jammed Pilot Detector Under Narrow-Band Jamming," *IEEE Transactions on Vehicular Technology*, Vol. 57, No. 3, May 2008, pp. 1934-1939.

[19] A. Rosenzweig, Y. Steinberg and S. Shamai, "On Channels with Partial Channel State Information at the Transmitter," *IEEE Transactions on Information Theory*, Vol. 51, No. 5, May 2005, pp. 1817-1830.

[20] S. Coleri, M. Ergen, A. Puri and A. Bahai, "Channel Estimation Techniques Based on Pilot Arrangement in OFDM Systems," *IEEE Transactions on Broadcasting*, Vol. 48, No. 3, September 2002, pp.223-229.

Int. J. Communications, Network and System Sciences, **2010, 3, 453-461**
doi:10.4236/ijcns.2010.35060 Published Online May 2010 (http://www.SciRP.org/journal/ijcns/)

ASIP Solution for Implementation of H.264 Multi Resolution Motion Estimation

Fethi Tlili, Akram Ghorbel
CITRA'COM Research Laboratory, Engineering School of Communications(*SUP'COM*), *Tunis, Tunisia*
E-mail: *fethi.tlili@supcom.rnu.tn*
Received March 19, 2010; *revised April* 20, 2010; *accepted May* 15, 2010

Abstract

Motion estimation is the most important module in H.264 video encoding algorithm since it offer the best compression ratio compared to intra prediction and entropy encoding. However, using the allowed features for inter prediction such as variable block size matching, multi-reference frames and fractional pel search needs a lot of computation cycles. For this purpose, we propose in this paper an Application Specific Instruction-set Processor (ASIP) solution for implementing inter prediction. An exhaustive full and fractional pel combined with variable block size matching search are used. The solution, implemented in FPGA, offers both performance and flexibility to the user to reconfigure the search algorithm.

Keywords: Motion Estimation, Half Pel, Quarter Pel, ASIP

1. Introduction

The fast growth of digital transmission services has created a great interest in digital transmission of image and video signals. These signals require very high bit rates in order to guarantee good video quality. Therefore, compression is used to reduce the amount of data needed for representing such signals. Compression is achieved by exploiting spatial and temporal redundancies in signals [1].

H.264 video coding standard currently allows an approximately 2:1 advantage in terms of bandwidth savings over MPEG-2, and it has the potential to allow further bandwidth savings of 3:1 and beyond. In other words, an H.264 coded stream needs roughly half of bit-rates to provide the same quality got by an MPEG-2 encoder. It also includes a video coding layer, which efficiently represents the video content independently of the targeted application. A network adaptation layer which formats the video data and provides header information in a manner appropriate to a particular transport layer is used. Finally, in order to decrease the decoder complexity, several application-targeted profiles and levels are defined which enable its successful use in different video applications and markets [2].

Despite the fact that it has kept the same coding aspect as previous standards based mainly on prediction, transform and entropy encoding, H.264 has introduced some key feature modules that have increased considerably the coding efficiency as well as more flexibility in most of the coding process.

However, H.264 is also a substantially more complex standard than MPEG-2; and both the H.264 encoders and decoders are much more demanding in terms of computations and memory than their MPEG-2 counterparts [3]. This, coupled with the substantial amount of research needed to properly implement and optimize the entire relevant H.264 features, makes the development of high-quality H.264 encoders a daunting task.

In addition to the complexity added by H.264 standard, low power consumption, high performance and scalability are the major constraints imposed to designers in the development of video encoders and decoders [4]. In fact, with the diversity of configurations supported by this standard in terms of resolutions and applications, scalable architectures for video encoders are much appreciated by service providers. In this context, neither hardware implementation solutions are efficient since they lack flexibility, nor software solutions present good performance since processors are no longer satisfying the high computational processing tasks [5].

To meet all these constraints, processor characteristics can be customized to match the application profile. Customization of a processor for a specific application holds the system cost down, which is particularly important for embedded consumer products manufactured in high volume. Application Specific Instruction set Processors (ASIPs) are in between custom hardware architectures

offering good processing performance and commercial programmable DSP processors with high programmability possibilities. They offer good programmability and performance level but are targeted to a certain class of applications as to limit the amount of hardware area and power needed [6].

This paper is organized as follows: Section 2 presents a complexity analysis of the different encoder's modules followed by the description of motion estimation standardized by H.264. In Section 3, we will present the proposed algorithm for multi resolution motion estimation. Section 4 presents the proposed ASIP solution. In Section 5 we will present implementation results. Finally, we enclose the paper by Section 6 in which we will conclude this work.

2. H.264 Video Encoder Study

2.1. Main Innovations of H.264

To achieve the required performance, H.264 allows some key features that ensure good coding efficiency. The main innovations of this standard are:

- Intra prediction process.
- Tree structured motion estimation, weighted prediction, multiple resolution search.
- Spatial in loop deblocking filter.
- Integer DCT like Transform.
- Efficient Macro Block Field Frame coding
- CABAC which provides a reduction in bit-rate from 5% to 15% over CAVLC.

2.2. Complexity Analysis of H.264 Video Encoder

In order to analyze the complexity of the H.264 encoding procedure, some profiling tasks were done on the several modules of the encoder mentioned above. For this reason, some implementations were performed on single chip DSP using CIF resolution in baseline profile to get the most accurate results since we have to avoid inter-chip communication that can bother the profiling results. **Figure 1** presents the profiling results of UBVideo encoder implemented on DM642 DSP of Texas Instruments [7].

We can see that the most consuming video tasks are motion search which is using about 30% of the processing time while the intra prediction, motion compensation and encoding (including transform, quantization and entropy encoding) are using only 23% of the system resources. Motion search includes only the best matching search while all load and store tasks are included in data transfer task which is using about 32% of system resources. The remaining 15% of the resources are used by other tasks such as rate control, video effect detection and bitstream formatting.

Hence, we can see that motion estimation is a bottle-neck for video encoding algorithms which is taking most of system resources. However, motion estimation is the most important module in the compression procedure due to its efficiency. In this context, some video encoders are using FPGA solutions for implementing motion estimators as hardware accelerators since DSPs cannot handle the processing required by such tasks.

3. Proposed Motion Estimation Implementation

3.1. H.264 Motion Estimation

Luminance component of each macro-block (16 × 16 samples) may be split up in 4 ways: 16 × 16, 16 × 8, 8 × 16 or 8 × 8 as shown in **Figure 2**. Each of the sub-divided regions corresponds to a macro-block partition. If the 8 × 8 mode is chosen, each of the four 8 × 8 macro-block partitions within the macro-block may be split in a further 4 ways: 8 × 8, 8 × 4, 4 × 8 or 4 × 4 as presented in **Figure 3**. Partitions and sub-partitions give rise to a large number of possible combinations within each macro-block. This method of partitioning macro-blocks into motion compensated sub-blocks of varying size is known as tree structured motion compensation.

In addition to the variable block size matching, H.264 defines multi resolution search process in order to provide better quality especially for non translational motion and aliasing caused by camera noise. Experimental analysis shows that the half and quarter-sample-accuracy

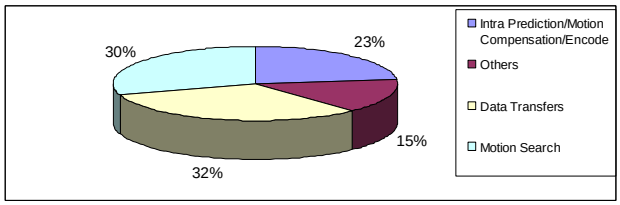

Figure 1. UbVideo encoder profile.

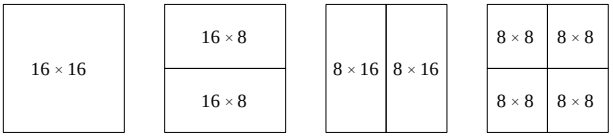

Figure 2. Macro-block partition.

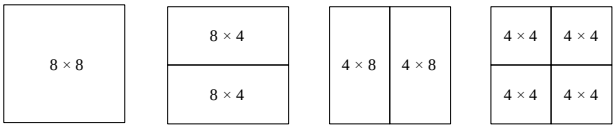

Figure 3. Macro-block sub partition.

motion search adopted by H.264/AVC provide a coding gain of 2 dB compared with MPEG-2 and H.263, which corresponds to a bit-rate savings of up to 30% [8]. Half pel search is performed on pixels interpolated using a 6 tap low pass filter. Furthermore, a quarter pel resolution search is established using a bi-liner filter applied on half pel interpolated pixels.

3.2. Proposed Motion Estimation Algorithm

The first step of the proposed ME algorithm consists in full pel resolution search. Current MB is searched in a predefined search area in the reference frame. In order to avoid unused computations and data load, the search is performed on 4 × 4 partitions base of the MB. For each 4 × 4 block, we search for the best matching position in the reference area. Every 4 × 4 block is independently parsed in all reference area. After that, a merging process is started in order to determine the best partition to be used for the current MB based on the best position which is stored relative to the top left pixel of the 4 × 4 block. The merging process is first used to determine if the current MB can be coded in partitions above than 4 × 4. So, we compare the best positions of adjacent blocks for all 8 × 8 partitions: if all blocks have the same best position, current sub partition is 8 × 8, otherwise, it could be 8 × 4, 4 × 8 or 4 × 4. If 8 × 8 mode is selected, a best position of the top left pixel is stored.

After that, we determine the MB prediction type that can be 16 × 16, 16 × 8, 8 × 16 or 8 × 8. A merging process similar to the previous one is also used: if all 8 × 8 sub partitions have the same type and the same best position, MB prediction type is 16 × 16; otherwise it could be 16 × 8, 8 × 16 or 8 × 8. After fixing the MB prediction type, a motion vector is stored for each partition. Obviously, the more we use sub partitions, more data to be transferred increases. We note that at least 40% of inter prediction data is used to code motion vectors. For this reason, it is better to use bigger partitions when possible. So, a prediction cost can be added by making conditions for the merge process based on tolerance of one or two pixels in the best positions: for example, if two 8 × 8 blocks have the best positions displaced of 1 pixel, we can decide to merge them into one 16 × 8 partition.

After searching for the best matching and the best partition, we start fractional pel search. According to the best position, for each MB partition we interpolate the possible 8 half pixels positions around the selected partition as shown in **Figure 4**. The interpolation is equivalent to an up-sampling of the frame pixels using 6 tap low pass filter.

After that, a further search is performed in quarter pel accuracy using another interpolation process. Based on the best position obtained in half pel search, we generate pixels of all the 8 possible positions around the best location. We note that motion vectors are multiplied by 4 in order to mention to the decoder if it has to interpolate pixels for motion compensation or not.

4. Proposed ASIP Solution

4.1. Analysis of the Proposed Motion Estimation Algorithm

In our work, we will adopt instruction selection methodology based on hardware architecture: first the hardware architecture is fixed containing selected functional units (FU) and then, instruction set architecture is determined according to the FUs. For this purpose, proposed algorithm is analyzed in order to pick up the most complex modules. These modules will be implemented in independent hardware blocks (dedicated FUs).

Proposed algorithm is composed mainly of 3 parts: full pel search, half pel interpolation and its associated search and finally quarter pel search with its final search.

In full pel search, the MB parses the whole reference area and 4 × 4 SADs are computed. In this step, the most complex process is the SAD computation since it includes difference computation, absolute value determination and accumulation. In [9], an analysis was performed on a motion estimation algorithm using SAD as a distortion measure; we found that SAD computation is using more than 97% of system resources.

In addition, sub pel motion estimation is also complex. In fact, the interpolation process for half pel is using 6-tap filter. Half samples are calculated through a 6-tap Wiener filter in both horizontal and vertical dimensions. The interpolation is processed as represented in **Figure 5**: dashed pixels correspond to full pixels in an 8x8 bloc. Non dashed pixels are half pixels that are calculated. For example, to interpolate half pixel 'b', we use E, F, G, H, I and J as full pixels. Calculation process is done as follows: b = Clip1 (((E − 5 × F + 20 × G + 20 × H − 5 × I + J) + 16) >> 5); clip function is used to provide result in the interval [0 , 255]: if result is less than 0 we affect 0 to 'b' and if it is more than 255 we affect 255 to 'b'. The same calculation process is done for vertical rows as 'h'.

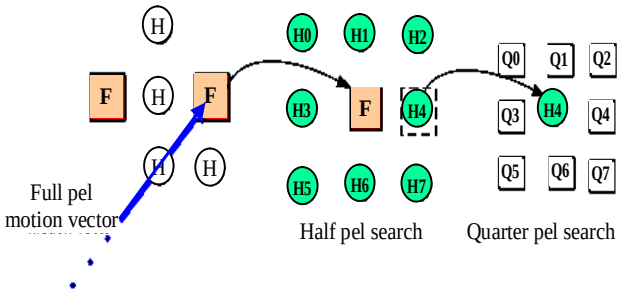

Figure 4. Fractional accuracy pixel search.

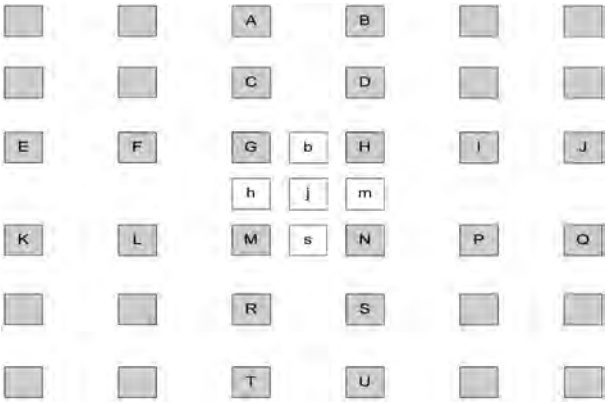

Figure 5. Half pel interpolation process.

Hence, half pel interpolation, as any filtering process is a very time consuming task and needs a lot of data load and store. Similarly, quarter pel interpolation is using bilinear filter to generate quarter pixels. Although the simplicity of the filter, this process also needs a lot of timing since it is applied to a large number of data.

In conclusion, the main complex modules in our proposed algorithm are the motion search, half pel interpolation and quarter pel interpolation. In our architecture, we will use hardware accelerators for these modules for better performance for our ASIP.

4.2. Functional Unit Selection

In our proposal, 3 hardware accelerators are used: SAD calculator, half pel interpolator and quarter pel interpolator.

The SAD calculator will be used to handle all SAD computation process including data load from internal memory and SAD calculation. The result is stored in a general purpose register.

Half pel interpolator module is used to interpolate half pixels according to the standardized filter. This module loads data from internal memory and interpolates pixels. Due to the complexity of interpolation, half pixels are stored in an internal memory to be used in further possessing tasks such as quarter pel interpolation or even half pixels. Finally, quarter pel interpolator loads data from internal memory and applies bilinear filter to generate quarter pixels. In order to avoid storing quarter pixels in memory, a SAD calculator is integrated in this module: reference pixels are loaded and quarter pel resolution SAD is computed. In motion compensation process, these pixels are re-computed since their computation is not as complex as half pixels.

In addition to the hardware accelerators for video processing, an Arithmetic and Logic Unit is used in the solution in order to accumulate SADs, generate pixel locations and memory addresses.

4.3. Instruction Set Selection

4.3.1. Video Instructions

- **SAD4Pix(DestReg,Curr_Pix_Addr,Ref_Pix_Addr,Pitch):** this instruction is used to compute SAD of 4 pixels based on current and reference pixel location and Pitch value. The choice of the 4 pixels size is based on the fact that the smallest partition allowed is 4×4; so to avoid using SAD instructions for all partitions, we call this instruction as much as the current partition contains 4 pixel lines. Since we adopt RISC (Reduced instruction Set Computer) architecture, current and reference pixel locations as well as Pitch value are stored in Special Purpose Registers (SPR). These registers are used only for video instructions since they need more than 2 input operands. Output of this instruction is stored in a General Purpose Register (GPR), DestReg in order to be accumulated to constitute the required SAD. The choice of the SAD computation size offers the flexibility to the user to choose block lines to be compared. In fact, we can compute only some specific lines in order to minimize the processing (for example odd lines or even lines).
- **Interp4HafPix(RefPixAddr,Pitch):** interpolates 4 half pixels and stores the result in internal memory. Input operands include the reference pixel address which refers to the first full pixel from which we start interpolation and a pitch value that is used for data load in case of vertical interpolation. This value is used to give the programmer the flexibility of modifying the search window size. These operands are loaded from SPRs while output interpolated pixels are stored in half pel memory since there is no need to store them in registers. In our motion estimation algorithm, after calling this instruction to interpolate half pixels of 1 MB, SAD4Pix instruction can be called in order to compute SAD in half pel resolution. For this reason, the pitch value is used in this instruction since the loading step in half pel memory is equal to 2. Hence, we avoid the use of 2 SAD instructions (one for full pel SAD and the other for half pel SAD).
- **Interp4QpixSAD(DestReg,Ref_pix,Curr_pix,Pitch):** used to interpolate 4 quarter pixels and compute quarter pel resolution SAD. We have chosen to separate half pel interpolation from quarter pel interpolation in order to give the user the flexibility to stop the search at any resolution according to the complexity of the algorithm. However, quarter pels are not stored and the corresponding SAD is immediately computed. In fact, quarter pels are no longer used by the system except the best match that is used for motion compensation where the best matching pixels are used. So, to avoid using huge memory size corresponding to store all interpolated pixels, we made the choice not to store them and to recompute the best matching pixels when required in motion compensation since their re-computation is easy as op-

posed to half pels. This instruction returns the SAD of the current position and the ALU decides for the best one to be used in motion compensation. Input operands to this instruction, reference and current pixels positions as well as pitch value are stored in SPRs. The output is stored in GPR, DestReg to be processed by the ALU for further decisions.

4.3.2. Memory Instructions

Memory instructions are used to transfer data between memory and registers or inter register transfer. Four instructions are used for this purpose:

- **MOVSG(Src,Dest)** is used to move data from specific to general purpose register. The operands of this instruction are formed by the addresses of registers to be manipulated.
- **MOVGS(Src,Dest)** is used to perform the inverse operation performed by MOVSG.
- **LOAD(SrcAddr,DestReg**) is used to load data from data memory to general purpose register. SrcAddr is the source address of data to be loaded while DestReg in the destination register ID.
- **STORE(SrcReg,DestAddr)** is used to store the content of a general purpose register in memory. The operands are SrcReg corresponding to the source register ID and DestAddr is the destination memory address.

4.3.3. Arithmetic and Logic Instructions

The main goal of these instructions is the accumulation of SAD values computed for each 4 pixels, computing pixel addresses, compare MB SADs and provide data for conditional jump. ALU instructions are processing only data from general purpose registers. We defined 3 arithmetic instructions:

- ADD, SUB and MUL are used respectively for addition, subtraction and multiplication operations. These instructions have 3 operands: the first one is the destination register ID containing the operation result while the 2 remaining operands are the IDs of registers containing source data to be processed.
- **SHIFT(SrcReg1,SrcReg2,SrcReg3)** is used for shifting data contained in SrcReg1 by the number of bits contained in SrcReg2. The shift direction is indicated by SrcReg3.

4.3.4. Control Instruction

The instruction JUMP introduces a change in the control flow of a program by updating the program counter with an immediate value that corresponds to an effective address. The instruction has 2 bits condition field (cc) that specifies the condition that must be verified for the jump: in if case the outcome of the last executed arithmetic is negative, positive or zero. Not only this instruction is important for algorithmic purposes, but also for improving code density, since it allows a minimization of the number of instructions required to implement a ME algorithm and therefore a reduction of the required capacity of the program memory.

4.4. Architecture of the Proposed ASIP

4.4.1. Data Word Length

Data word length is a tradeoff between performance and complexity. In fact, the data word length corresponds to the instruction word length which is stored and manipulated by the processor. Hence, in case of longer instruction word length, we have the possibility of using more instructions and more registers which will accelerate the processing since memory access will be reduced. However, the instruction decoder will be more complex as well as the interconnection between components; therefore, the processor area will be larger.

In our proposal, we have only 12 instructions which can be coded on 4 bits. In order to simplify the hardware architecture, we have chosen to use 16 bits to code all instructions. So, 12 bits can be used to address the register file.

4.4.2. Register File Size

Since the instruction length is 16 bits and 4 bits are used to code instructions, the 12 remaining are used to code the different registers used. Since arithmetic instructions are using 3 GPPs, we will code each register on 4 bits, so 16 GPPs can be used in our architecture. On the other side, video instructions are using both GPPs and SPPs. So, 8 bits only can be used to code 3 registers in the instruction call: each register is addressed on 2 bits. So, 4 SPPs are used. At this stage, we can see the importance of the use of GPPs and SPPs: if we use only one register type, when calling video instruction, 12 bits are used to code 4 registers: 3 bits are used per register as a consequence. Therefore, only 8 registers are used in this case while in our design we are using 20 registers with the same instruction length. **Table 1** presents the different

Table 1. Instruction set architecture of the proposed ASIP.

Instrution	15 12	11 10	9 8 7	6 5	4 3	2 1 0
SAD4Pix	0000	RestReg	R1	R2	R3	-
Interp4HafPix	0001	-	R1	R2	-	
Interp4QpixSAD	0010	DestReg	R1	R2	R3	-
MOVSG	0010	-		Src	DestReg	
MOVGS	0011	SreReg				Dest
LOAD	0100	#addr			DestReg	
STOR	0101	SreReg	#addr			
ADD	0110	DestReg	SreReg1		SreReg2	
SUB	0111	DestReg	SreReg1		SreReg2	
MUL	1000	DestReg	SreReg1		SreReg2	
SHIFT	1001	SreReg1	SreReg2		SreReg3	
JUMP	1010	CC	#addr			

instructions with the corresponding codes, operands with their corresponding size.

4.4.3. Micro Architecture

Figure 6 presents the micro architecture of the proposed ASIP.

The solution is composed of an instruction fetch module to load instructions from program memory, instruction decoder to enable the several functional units and a register file to store processed data. Video functional units are connected to the internal data memory and the ALU. Data load from external memory to internal memory is handled by a direct memory access controller.

5. Implementation Solution and Results

The proposed ASIP was implemented and synthesized on Virtex II Pro FPGA.

5.1. Memory Management

In our motion estimation algorithm, the search region area is fixed to 31 × 23 pixels. We note that we need to extend this search region by 16 pixels in both sides (right and bottom) since the last right-bottom position must be displaced of a (15, 12) vector from the centre. Furthermore, to interpolate boundary pixels, an extension of three pixels is needed for each side. **Figure 7** describes the search area with the several extensions.

Hence, the total search area has to be 53 × 45; so 2385 pixels have to be loaded from external to internal memory. Internal memory is designed to be 2 × 18 Kb block RAM integrated in Virtex II FPGA. We note also that a further 1 × 18 Kb block RAM is also needed to store the current MB. Internal memory is 8 bits width for implementation constraints: since we adopt exhaustive search, the whole reference area is parsed in order to search for the best matching MB; so, if we load more than one pixel from reference area, we will be faced to an alignment problem. To avoid such problems, we have chosen to load one pixel in each cycle assuming that this procedure is more consuming in time. Data load to internal memory is ensured by Direct Memory Access controllers which handles the transfer process while the CPU is running. When transfer is finished, an interrupt signal is mentioned.

Synthesis results of the DMA controller shown in **Table 2** presents that this module using roughly 10% of the available FPGA resources and can be run at 205 Mhz clock frequency.

5.2. SAD Engine

This engine is used to compute the SAD of 4 pixels. This module loads reference and current pixels from the internal memory and performs the SAD of 4 pixels in one call. The SAD module can be used in the SAD computation of the full pel or half pel search.

As described in **Figure 8**, the SAD engine is providing the output after 9 cycles from the start signal. The output is finally returned to the register file. We note that TMS320C64 DSP is providing SAD of 4 4 × 4 blocks

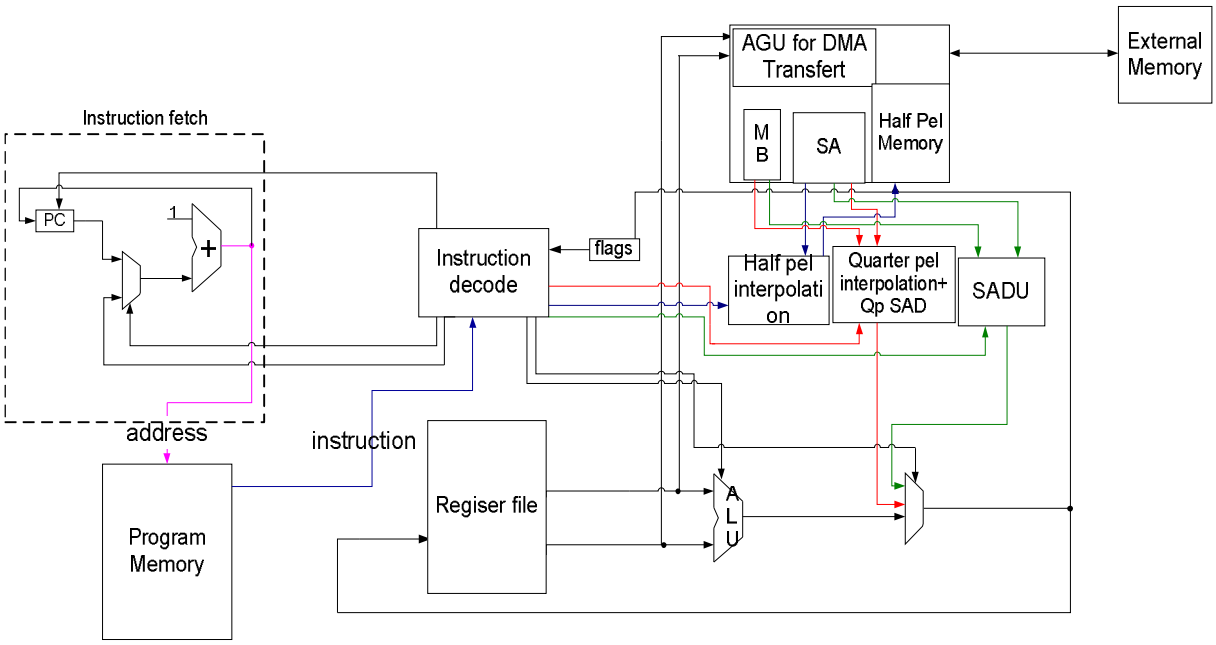

Figure 6. Architecture of the proposed ASIP.

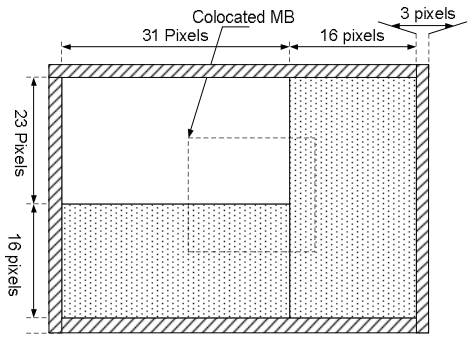

Figure 7. Search area organization.

Table 2. Synthesis results of DMA controller.

Device utilization summary	
Number of Slices	190 out of 1408 13%
Number of Slices Flip Flops	178 out of 2816 6%
Number of 4 input LUTs:	300 out of 2816 10%
Number of GCLKs	1 out of 16 6%
Timing Summary:	
Minimum period/Maximum Frequency	4.877 ns/205.025 MHz
Minimum input arrival time before clock	5.294 ns
Maximum output required time after clock	4.968 ns
Maximum combinational path delay	No path found

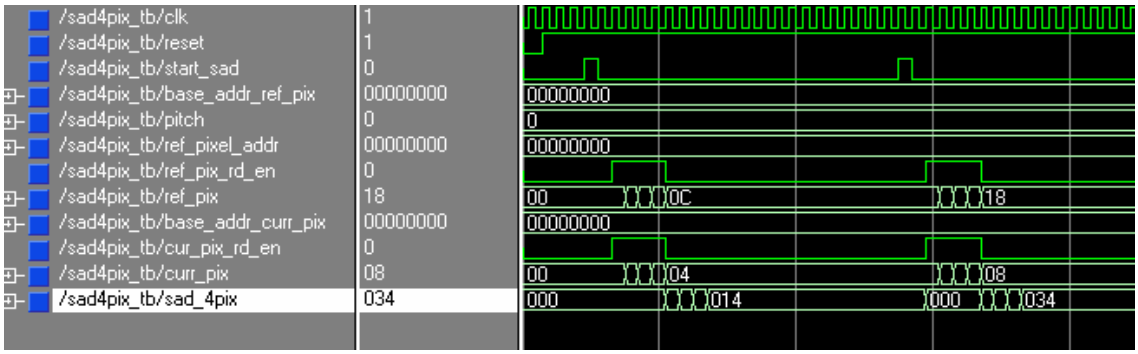

Figure 8. Timing diagram of SAD engine.

(split_sad8 × 8) in 200 cycles in the best case: when all data paths are fully used [10] while our system can provide the same result after 144 cycles without using pipeline.

5.3. Half Pel Interpolator

In our implementation, the proposed algorithm is derived by minimizing the number of memory access. The formulas to compute half-pixel interpolations are proposed by using the symmetry of the 6-tap FIR filter coefficients, resulting in significant reduction of the multiplications [11].

This engine is providing 4 interpolated pixels in each call. Input pixels are stored in 6 registers; the size of each one is 32 bits as described in **Figure 9**:

We note that pixels P3 to P6 form a line of a selected 4 × 4 block to be interpolated. The output pixels are H0 to H3. A Single Instruction Multiple Data scheme is adopted in our implementation. In this mode, adders and multipliers are applied simultaneously to the pixels of registers in order to get all interpolated pixels at the same time. All control signals are provided by an FSM.

We note that the interpolation takes 15 cycles including the load process from internal memory. Synthesis results are shown in **Table 3**.

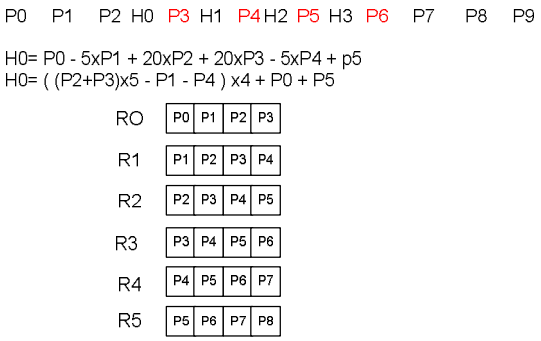

Figure 9. Input registers for halfpel interpolation.

Table 3. Synthesis results of half pel interpolator.

Device utilization summary	
Number of Slices	354 out of 1408 25%
Number of Slices Flip Flops	460 out of 2816 16%
Number of 4 input LUTs:	343 out of 2816 12%
Number of MULT18X18s	4 out of 12 33%
Number of GCLKs	1 out of 16 6%
Timing Summary:	
Minimum period/Maximum Frequency	5.504 ns/181.689 MHz
Minimum input arrival time before clock	4.679 ns
Maximum output required time after clock	3.638 ns
Maximum combinational path delay	3.802 ns

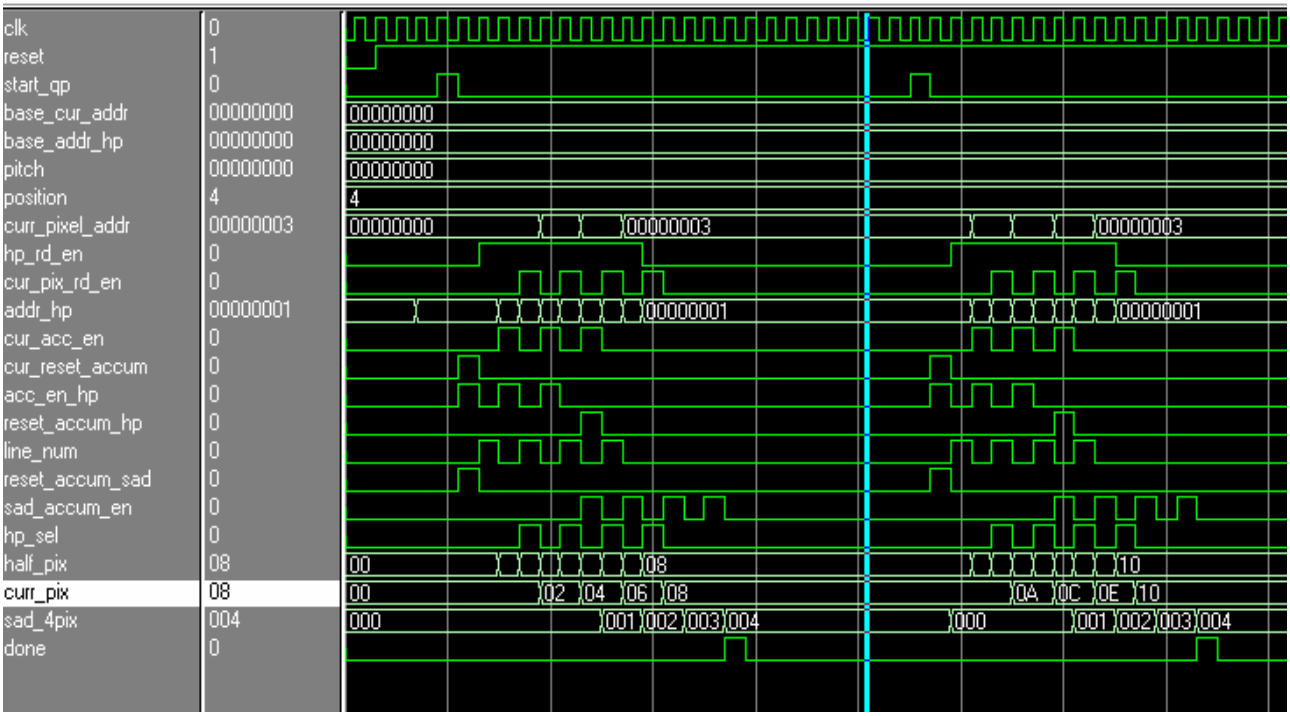

Figure 10. Timing diagram of Quarte pel interpolator.

5.4. Quarter Pel Interpolator

When receiving Interp4QpixSAD(Ref_pix,Curr_pix,Pitch) instruction, quarter pel interpolation and SAD computation are started. First, pixels loaded from half pel memory are fed into the interpolator module, then, the resulting quarter pixels are transmitted to the SAD module to be compared to the current pixels. We note that QP interpolator interpolates and generates the SAD of 4 pixels in each call.

Quarter pel SADs are returned after 14 cycles as shown in the timing diagram shown in **Figure 10**.

6. Conclusions

This paper has presented efficient instructions for implementing motion estimation process using most of the key features standardized in H.264. First, we analyzed the complexity of typical H.264 encoder. From this step, we concluded that ME is a bottle neck for the implementation. Then, we presented and analyzed an algorithm for ME. Based on the analysis, we proposed efficient accelerators for some modules which need most of the processing time. Based on the suggested hardware architecture, we fixed the instruction set architecture providing to users large coding flexibility ensuring scalability and multi-standard support. Proposed ASIP was implemented on Virtex II pro FPGA with a total area use about 61% of the FPGA Slices and 43% of the total LUTs. The implemented modules can be run on 172 MHz clock.

7. References

[1] Q. Y. Shi and H. F. Sun, "Image and Video Compression for Multimedia Engineering: Fundamentals, Algorithms, and Standards,"2nd Édition, CRC Press, Boca Raton, 2008.

[2] Draft 3rd Edition of ISO/IEC 14496-10 (E), Redmond, WA, USA, July 2004.

[3] F. Kossentini and A. Jerbi, "Exploring the Full Potential of H.264," *NAB*, 2007.

[4] S. D. Kim, J. H. Lee, C. J. Hyun and M. H. Sunwoo, "ASIP Approach for Implementation of H.264/AVC," *Journal of Signal Processing Systems*, Vol. 50, No. 1, 2008, pp. 53-67.

[5] P. Harm, *et al.*, "Application Specific Instruction-Set Processor Template for Motion Estimation in Video Applications," *IEEE Transactions on Circuits and Systems for Video Technology*, Vol. 15, No. 4, April 2005, pp. 508-527.

[6] M. Kumar, M. Balakrishnan and A. Kumar, "ASIP Design Methodologies: Survey and Issues," 14*th International Conference on VLSI Design*, Bangalore, 2001.

[7] I. Werda and F. Kossentini, "Analysis and Optimization of UB Video's H.264 Baseline Encoder if Texas Instru-

ment's TMS320DM642 DSP," *IEEE International Conference on Image Processing*, Atlanta, October 2006.

[8] S. Yang, *et al.*, "A VLSI Architecture for Motion Compensation Interpolation in H.264/AVC," 6*th International Conference on ASIC*, shanghai, 2005.

[9] W. Geurts, *et al.*, "Design of Application-Specific Instruction-Set Processors for Multi-Media, Using a Retargetable Compilation Flow," *Proceedings of Global Signal Processing* (*GSPx*) *Conference, Target Compiler Technologies*, Santa Clara, 2005.

[10] M. A. Benayed, A. Samet and N. Masmoudi, "SAD Implementation and Optimization for H.264/AVC Encoder on TMS320C64 DSP," 4*th International Conference on Sciences of Electronic, Technologies of Information and Telecommunications* (*SETIT* 2007), Tunisia, 25-29 March 2007.

[11] C.-B. Sohn and H.-J. Cho, "An Efficient SIMD-based Quarter-Pixel Interpolation Method for H.264/AVC," *International Journal of Computer Science and Security*, Vol. 6, No. 11, November 2006, pp.85-89.

Int. J. Communications, Network and System Sciences, **2010, 3, 462-465**
doi:10.4236/ijcns.2010.35061 Published Online May 2010 (http://www.SciRP.org/journal/ijcns/)

Scientific Research

Microstrip Low-Pass Elliptic Filter Design Based on Implicit Space Mapping Optimization

Saeed Tavakoli, Mahdieh Zeinadini, Shahram Mohanna
Faculty of Electrical and Computer Engineering, the University of Sistan and Baluchestan, Zahedan, Iran
E-mail: *Tavakoli@ece.usb.ac.ir*
Received February 21, 2010; *revised March* 27, 2010; *accepted April* 28, 2010

Abstract

It is a time-consuming and often iterative procedure to determine design parameters based on fine, accurate but expensive, models. To decrease the number of fine model evaluations, space mapping techniques may be employed. In this approach, it is assumed both fine model and coarse, fast but inaccurate, one are available. First, the coarse model is optimized to obtain design parameters satisfying design objectives. Next, auxiliary parameters are calibrated to match coarse and fine models' responses. Then, the improved coarse model is re-optimized to obtain new design parameters. The design procedure is stopped when a satisfactory solution is reached. In this paper, an implicit space mapping method is used to design a microstrip low-pass elliptic filter. Simulation results show that only two fine model evaluations are sufficient to get satisfactory results.

Keywords: Implicit Space Mapping Optimization, Microstrip Low-Pass Elliptic Filter, Surrogate Model

1. Introduction

Considering the development of computer-aided design methods, optimization has become a widely used technique in design of microwave circuits. A typical design problem is to choose the design parameters to get the desired response. The space mapping (SM), introduced in [1], is a powerful technique to optimize complex models. The aim of this technique is to make a shortcut using a cheaper but less accurate model, coarse model, to gain information about the optimal parameter setting of the expensive but accurate model, fine model. To obtain the optimal design for the fine model, the SM establishes a mapping between the parameters of the two models iteratively [1,2]. In some cases, this mapping is not explicit and it is hidden in the coarse model. The implicit space mapping (ISM) [3], described below, addresses this issue.

First, the coarse model is optimized to obtain design parameters satisfying the design objectives. Second, an auxiliary set of parameters in the coarse model, which always remain fixed in the fine model, is calibrated to match coarse and fine models' responses. This step is known as the parameter extraction step. Examples of the auxiliary parameters are physical parameters, such as relative dielectric constant, and geometrical parameters, such as substrate height. The coarse model with updated values of auxiliary parameters is known as the surrogate, calibrated coarse, model. Considering the re-calibrated auxiliary parameters fixed, then, the calibrated coarse model is re-optimized to obtain a new set of design parameters. These design parameters are given to the fine model to evaluate its performance [4]. The design procedure is stopped when a satisfactory solution is reached.

In this paper, an optimization procedure based on ISM technique is applied to a microstrip low-pass elliptic filter. Agilent ADS and ADS Momentum [5] are employed to simulate coarse and fine models, respectively.

2. Implicit Space Mapping Approach

The design objective is to calculate an optimal solution for the fine model, as follows

$$x_f^{\,*} = \arg\min_{x_f} \Omega\left(R_f\left(x_f\right)\right) \tag{1}$$

where Ω is a suitable objective function. The fine model's response, R_f, is, for example, $\left|S_{11}\right|$ at selected frequency points. $x_f^{\,*}$ is the optimal fine model parameters to be determined. It can be found using the following iterative procedure

$$x_f^{\,k+1} = \arg\min_{x_f} \Omega\left(R_s\left(x_f, p^K\right)\right) \tag{2}$$

where R_s refers to the surrogate model's response. To

solve Equation (1), a two-step procedure is employed. In the first step, the auxiliary parameters are calibrated so that the surrogate and fine models' responses become similar enough. The auxiliary parameters are calculated using the following equation

$$p^k = \arg\min_P \left\| R_f\left(x_f{}^K\right) - R_s\left(x_f{}^K, p\right) \right\| \quad (3)$$

where p^0 refers to the initial auxiliary parameters. Considering the re-calibrated auxiliary parameters fixed, then, the new surrogate model is re-optimized to obtain a new set of design parameters, x_f^{new}, in the second step. If the fine model's response for this new set of design parameters satisfies the design specifications, the algorithm is stopped. Otherwise, it re-calculates the auxiliary parameters for the current design parameters [4,6].

3. Microstrip Low-Pass Elliptic Filter

Low-pass filters are components, which are used to eliminate unwanted harmonics. Low-pass elliptic filters can provide a fairly sharp cut-off frequency [7]. In this paper, ISM technique is applied to the optimization problem of a low-pass elliptic filter with a cut-off frequency of 7 GHz. The structure of this filter is illustrated in **Figure 1**.

The coarse model is composed of empirical models of simple microstrip elements, as shown in **Figure 2**. The design specifications are as follows:

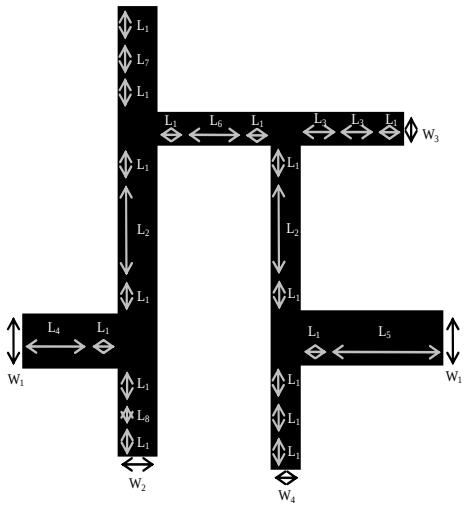

Figure 1. Microstrip low-pass elliptic filter structure.

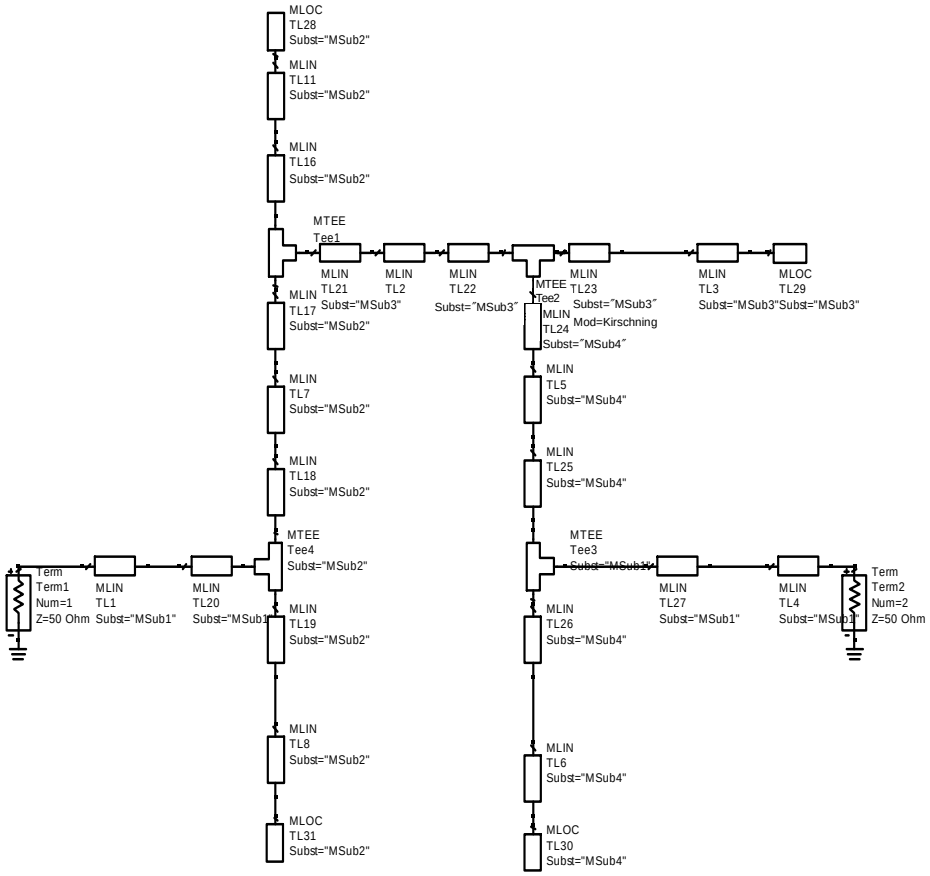

Figure 2. Coarse model simulated by ADS.

$$\begin{aligned} &|S12| \geq 0.964, 0.001\,\text{GHz} \leq \omega \leq 7\,\text{GHz} \\ &|S12| \leq 0.0025, 11.65\,\text{GHz} \leq \omega \leq 11.7\,\text{GHz} \end{aligned} \quad (4)$$

The filter structure is made of a perfect conductor on the top of a substrate with a relative dielectric constant of 10 and a height of 635 μm, backed with a perfect conductor ground plane. When designing a coarse model in ADS, its parameters could be tunable. This tuning capability allows one to graphically see how the parameters affect the responses. As a result, design parameters for the design procedure and parameter extraction step can appropriately be chosen. We set $L_4 = 1693\,\mu\text{m}$, $L_5 = 2403\,\mu\text{m}$ and $L_8 = 18\,\mu\text{m}$ because ADS tuning process shows that these parameters do not have significant effects on design specifications. Now, the design parameters and auxiliary parameters are given by $x_f = [W_1, W_2, W_3, W_4, L_1, L_2, L_3, L_6, L_7]$ and $p = [h_1, h_2, h_3, h_4, \varepsilon_{r1}, \varepsilon_{r2}, \varepsilon_{r3}, \varepsilon_{r4}]$, respectively, where h_i and ε_{ri} refer to the height and relative dielectric constant for each microstrip line having a width of W_i.

In the parameter extraction step, we use ADS quasi-Newton optimization algorithm to match the fine and surrogate models' magnitude of scattering parameters. The optimal coarse model is obtained using the ADS gradient optimization algorithm. The main advantage of implicit space mapping optimization technique is that, in this example, the design algorithm requires only one iteration, *i.e.*, two fine model simulations. The coarse and fine models' responses for the initial and final design parameters are demonstrated in **Figure 3** and **Figure 4**, respectively.

Table 1 shows the initial and final values of design parameters. The original and final values of auxiliary parameters are given in **Table 2**.

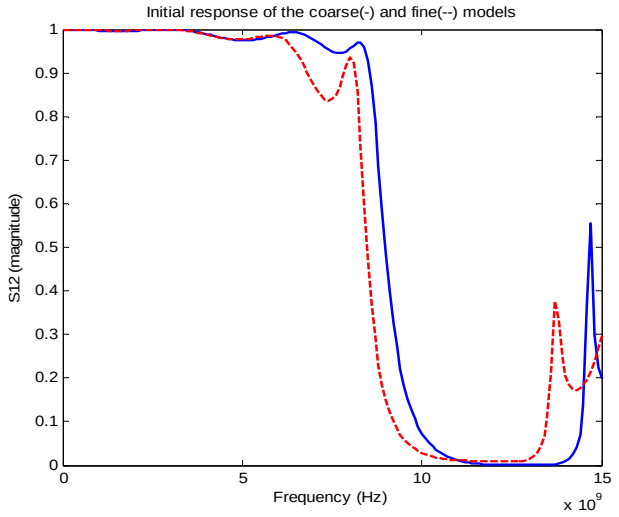

Figure 3. Coarse and fine models' responses for initial solutions.

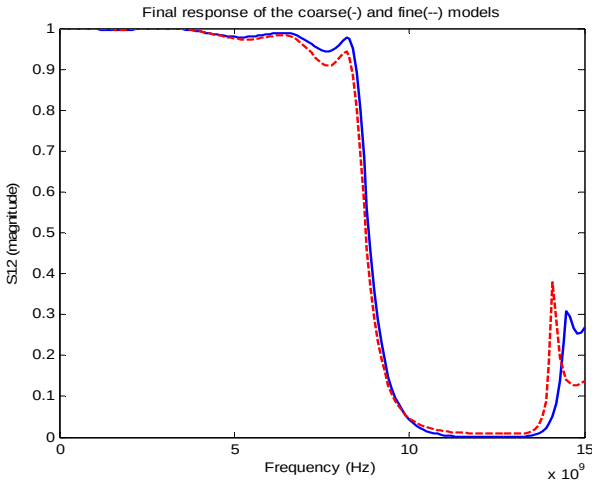

Figure 4. Coarse and fine models' responses for final solutions.

Table 1. Design parameters.

Design parameters	Initial values	Final values
W_1 (μm)	638.215	559.408
W_2 (μm)	421.246	437.354
W_3 (μm)	351.031	336.444
W_4 (μm)	333.715	343.167
L_1 (μm)	690.834	647.674
L_2 (μm)	1536.79	1443.19
L_3 (μm)	811.063	820.294
L_6 (μm)	1646.5	1705.57
L_7 (μm)	774.116	766.248

Table 2. Auxiliary parameters.

Auxiliary parameters	Original values	Final values
h_1 (μm)	635	610.787
h_2 (μm)	635	764.68
h_3 (μm)	635	625.413
h_4 (μm)	635	781.898
ε_{r1}	10	10.3323
ε_{r2}	10	10.8587
ε_{r3}	10	10.6504
ε_{r4}	10	11.6629

4. Conclusions

Using implicit space mapping method, the design parameters for a microstrip low-pass elliptic filter were determined. It was shown that this technique led to de-

creasing the number of fine model evaluations. First, the coarse model was optimized to obtain design parameters satisfying the design objective. Second, auxiliary parameters were calibrated in the coarse model to match coarse and fine models' responses. Third, the improved coarse model was re-optimized to obtain a new set of design parameters. Finally, the resulting design parameters were given to the fine model to evaluate its performance. The design procedure was repeated by the time a satisfactory solution was obtained. Simulation results showed that only two evaluations of the fine model were sufficient to get satisfactory results for the given case-study application.

5. References

[1] J. W. Bandler, R. M. Biernacki, S. H. Chen, P. A. Grobelny and R. H. Hemmers, "Space Mapping Technique for Electromagnetic Optimization," *IEEE Transactions on Microwave Theory and Techniques*, Vol. 42, No. 12, 1994, pp. 2536-2544,.

[2] J. W. Bandler, Q. S. Cheng, S. A. Dakroury, A. S. Mohamed, M. H. Bakr, K. Madsen and J. Søndergaard, "Space Mapping: the State of the Art," *IEEE Transactions on Microwave Theory and Techniques*, Vol. 52, No. 1, 2004, pp. 337-361.

[3] J. W. Bandler, Q. S. Cheng, N. K. Nikolova and M. A. Ismail, "Implicit Space Mapping Optimization Exploiting Preassigned Parameters," *IEEE Transactions on Microwave Theory and Techniques*, Vol. 52, No. 1, 2004, pp. 378-385.

[4] S. Koziel, Q. S. Cheng and J. W. Bandler, "Space Mapping," *IEEE Microwave Magazine*, Vol. 9, No. 6, December 2008, pp. 105-122.

[5] "Agilent Advanced Design System (ADS)," Ver. 2008A, Agilent Technologies, Santa Rosa, CA, 2008.

[6] J. W. Bandler, Q. S. Cheng, D. H. Gebre-Mariam, K. Madsen, F. Pedersen and J. Søndergaard, "EM-based Surrogate Modeling and Design Exploiting Implicit, Frequency and Output Space Mappings," *IEEE MTT-S International Microwave Symposium Digest*, Philadelphia, 2003, pp. 1003-1006.

[7] M. C. V. Ahumada, J. Martel and F. Medina, "Design of Compact Low-Pass Elliptic Filters Using Double-Sided MIC Technology," *IEEE Transactions on Microwave Theory and Techniques*, Vol. 55, No. 1, January 2007, pp. 121-127.

Int. J. Communications, Network and System Sciences, **2010, 3, 466-471**
doi:10.4236/ijcns.2010.35062 Published Online May 2010 (http://www.SciRP.org/journal/ijcns/)

Particle Swarm Optimization Based Approach for Resource Allocation and Scheduling in OFDMA Systems

Chilukuri Kalyana Chakravarthy[1], Prasad Reddy[2]
[1]*Department of Computer Science and Engineering, Maharaj Vijayaram Gajapathi Raj College of Engineering, Vizianagaram, India*
[2]*Department of CS&SE, Andhra University, College of Engineering, Visakhapatnam, India*
E-mail: *kch.chilukuri@gmail.com, prof.prasadreddy@gmail.com*
Received March 9, 2010; *revised April* 10, 2010; *accepted May* 11, 2010

Abstract

Orthogonal Frequency-Division Multiple Access (OFDMA) systems have attracted considerable attention through technologies such as 3GPP Long Term Evolution (LTE) and Worldwide Interoperability for Microwave Access (WiMAX). OFDMA is a flexible multiple-access technique that can accommodate many users with widely varying applications, data rates, and Quality of Service (QoS) requirements. OFDMA has the advantages of handling lower data rates and bursty traffic at a reduced power compared to single-user OFDM or its Time Division Multiple Access (TDMA) or Carrier Sense Multiple Access (CSMA) counterparts. In our work, we propose a Particle Swarm Optimization based resource allocation and scheduling scheme (PSORAS) with improved quality of service for OFDMA Systems. Simulation results indicate a clear reduction in delay compared to the Frequency Division Multiple Access (FDMA) scheme for resource allocation, at almost the same throughput and fairness. This makes our scheme absolutely suitable for handling real time traffic such real time video-on demand.

Keywords: OFDMA, Resource Allocation, Scheduling, Quality of Service, Delay

1. Introduction

TDMA and FDMA used for distributing subcarriers in OFDM systems form static subcarrier management schemes. While in OFDM-TDMA, one of the users is assigned all the subcarriers for the entire scheduling interval, in the OFDM-FDMA, each user is assigned predetermined number of subcarriers. However, neither of these techniques is time or frequency efficient: TDMA is a time hog and FDMA is a bandwidth hog. OFDMA is a multi-user OFDM that allows multiple access on the same channel (a channel being a group of evenly spaced subcarriers, as discussed above). WiMAX uses OFDMA, extended OFDM, to accommodate many users in the same channel at the same time. In OFDMA, the OFDMA subcarriers are divided into subsets of subcarriers, each subset representing a subchannel (see **Figure 1**). Dynamic subcarrier allocation schemes which consider the instantaneous channel conditions have been the main area of research interest recently. The resource allocation is usually formulated as a constrained optimization problem, to either 1) minimize the total transmit power with a constraint on the user data rate [1,2] or 2) maximize the total data rate with a constraint on total transmit power [3-5]. The first objective is appropriate for fixed-rate applications, such as voice, whereas the second is more appropriate for bursty applications, such as data and other IP applications.

In the downlink, a subchannel may be intended for different receivers or groups of receivers; in the uplink, a transmitter may be assigned one or more subchannels. The subcarriers forming one subchannel may be adjacent or not. The standard indicates that the OFDM symbol is divided into logical subchannels to support scalability,

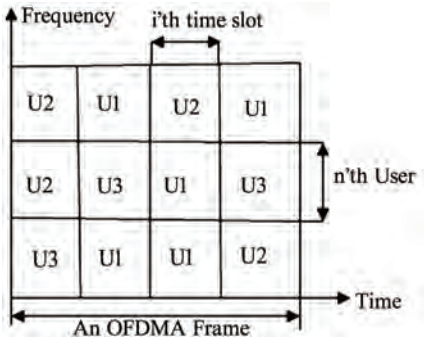

Figure 1. OFDMA frame structure.

multiple access and advanced antenna array processing capabilities. The multiple access has a new dimension with OFDMA where in a downlink or an uplink user will have a time and a subchannel allocation for each of its communications.

The main motivation for adaptive subcarrier allocation in OFDMA systems is to exploit multiuser Diversity. In a *K*-user system in which the subcarrier of interest experiences i.i.d. Rayleigh fading—that is, each user's channel gain is independent of the others, as the number of users' increases, the probability of getting a large channel gain increases. Further, it was observed that majority of the gain is achieved from only the first few users. Adaptive modulation is the means by which good channels can be exploited to achieve higher data rates.

WiMAX systems use adaptive modulation and coding in order to take advantage of fluctuations in the channel. The basic idea is quite simple: Transmit as high a data rate as possible when the channel is good, and transmit at a lower rate when the channel is poor, in order to avoid excessive dropped packets. While Lower data rates are achieved by using a small constellation, such as QPSK, and low-rate error-correcting codes, such as rate convolutional or turbo codes, the higher data rates are achieved with large constellations, such as 64 QAM, and less robust error correcting codes; for example, rate convolutional, turbo, or LDPC codes. However, a key challenge in AMC is to efficiently control three quantities at once: transmit power, transmit rate (constellation), and the coding rate.

In theory, the best power-control policy from a capacity standpoint is the so-called waterfilling strategy, in which more power is allocated to strong channels and less power allocated to weak channels [6]. In practice, the opposite may be true in some cases. For example, in regions of low gain, the transmitter would be well advised to lower the transmit power, in order to save power and generate less interference to neighboring cells [7].

As mentioned earlier, OFDMA thus facilitates the exploitation of frequency diversity and multiuser diversity to significantly improve the system capacity. In a multiuser System, the optimal solution is not necessarily to assign the best subcarriers seen by a single chosen user since the best subcarrier of one user is also the best subcarrier for another user who has no other good subcarriers. Hence, a different approach should be considered for scheduling the best user. We consider the problem where K users are involved in the OFDMA system to share N subcarriers. Each user allocates non overlapping set of subcarriers Sk where the number of subcarriers per user is J(k). The allocation module of the transmitter assigns subcarriers to each user according to some QoS criteria. QoS metrics in the system are rate and BER. Each user's bit stream is transmitted using the assigned subcarriers and adaptively modulated for the number of bits assigned to the subcarrier. The power level of the modulation is adjusted to meet QoS for given fading of the channel (see **Figure 2**).

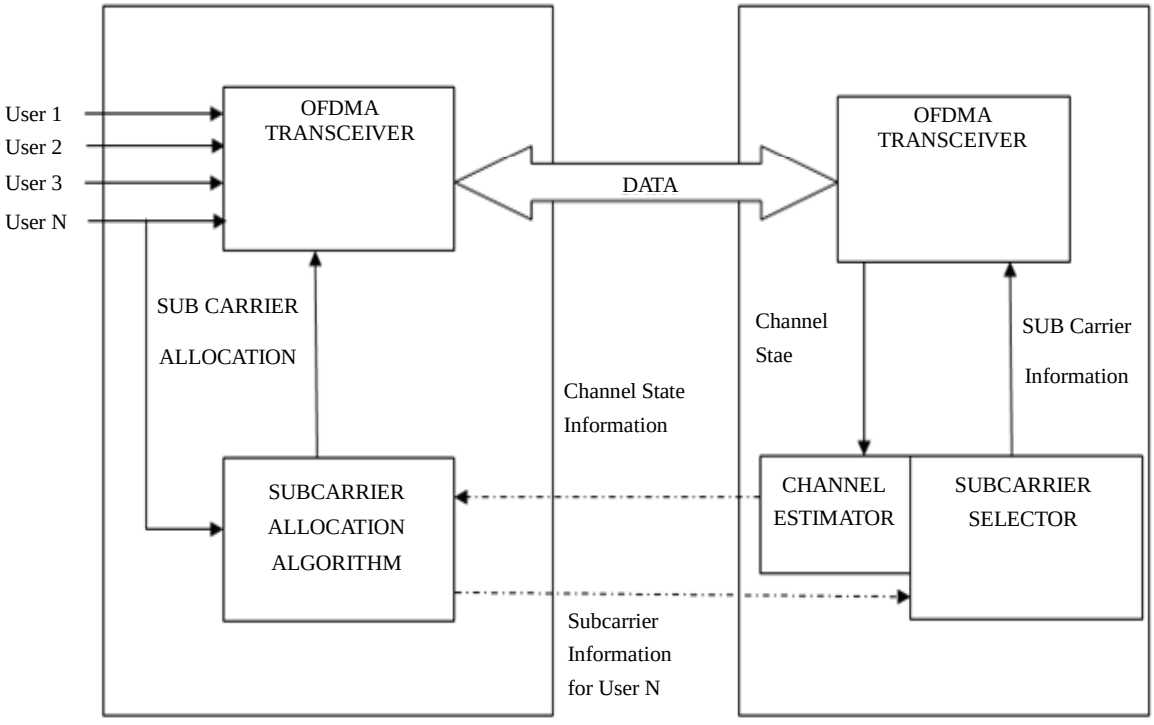

Figure 2. Downlink OFDMA System architecture.

If $\gamma_{k,n}$ is the indicator of allocating the nth subcarrier to the kth user, the transmission power allocated to the nth subcarrier of *k*th user can be expressed as $P_{k,n} = f_k(C_{k,n}, BER_k)/\alpha^2_{k,n}$ where $f_k(C_{k,n})$ is the required received power with unity channel gain for reliable reception of *c* bits per symbol. Therefore, the resource allocation problem with an imposed power constraint can be formulated as

$$\max C_{k,n}, \gamma_{k,n} \; R_k = \sum_{n=1}^{N} C_{k,n}\gamma_{k,n} \quad \text{for all } k$$

$$\text{subject to} \quad P_r = \sum_{k=1}^{K}\sum_{n=1}^{N} \frac{f_k(C_{k,n}, BER_k)}{\alpha^2_{k,n}} \; \gamma_{k,n} \le P_{\max}$$

The limit on the total transmission power is expressed as $P_{\max}$ for all $n \in \{1, \ldots, N\}$, $k \in \{1, \ldots, K\}$ and $C_{k,n} \in \{1, \ldots, M\}$. The proposed method uses the Particle Swarm Optimization for resource allocation and scheduling in a multiuser scenario, considering the rate, power and the subcarrier allocation constraints.

2. Particle Swarm Optimization

Particle Swarm Optimization (PSO) is motivated from the simulation of social behavior of animals'. It was introduced by Eberhart & Kennedy in 1995. In PSO, potential solutions (particles) move dynamically in space. PSO is similar to the other evolutionary algorithms in which the system is initialized with a population of random solutions. A list of Genetic algorithms is given in [8-12]. Each potential solution, call particles, flies in the D-dimensional problem space with a velocity which is dynamically adjusted according to the flying experiences of its own and its colleagues. The location of the ith particle is represented as $X_i = (x_{i1}, \ldots, x_{id}, \ldots, x_{iD})$. The best previous position (which giving the best fitness value) of the ith particle is recorded and represented as $P_i = (p_{i1}, \ldots, p_{id}, \ldots, p_{iD})$, which is also called pbest. The index of the best pbest among all the particles is represented by the symbol g. The location Pg is also called gbest. The velocity for the ith particle is represented as $V_i = (v_{i1}, \ldots, v_{id}, \ldots, v_{iD})$. The particle swarm optimization concept consists of, at each time step, changing the velocity and location of each particle toward its pbest and gbest locations. The particle swarm optimization concept consists of, at each time step, changing the velocity and location of each particle toward its pbest and gbest locations according to the equations $v_{id} = \mathrm{w} \times v_{id} + \mathrm{c1} \times \mathrm{rand}() \times (p_{id} - x_{id}) + \mathrm{c2} \times \mathrm{rand}() \times (p_{gd} - x_{id})$ and $x_{id} = x_{id} + v_{id}$ respectively.where w is inertia weight, c1 and c2 are acceleration constants [13] which is responsible for keeping the particle moving in the same direction, and rand() is a random function in the range [0, 1]. For the first equation, the first part represents the inertia of pervious velocity; the second part is the "cognition" part, which represents the private thinking by itself which causes the particle to move to regions of higher fitness; the third part is the "social" part, which represents the cooperation among the particles [14]. Thus the social component causes the particle to move to the best region the swarm has found so far.

The PSO algorithm consists of just three steps, which are repeated until some stopping condition is met [15]:

1) Evaluate the fitness of each particle

2) Update individual and global best fitnesses and positions

3) Update velocity and position of each particle

Further, velocity clamping is used to prevent the particle to move too much away from the search space, the limits being confined to $[-V_{\max}, V_{\max}]$ if the search space spans from $[-P_{\max}, P_{\max}]$[16].

3. The Proposed System

In this work, we propose a Particle Swarm Optimization (PSO) Approach combined with Credit based scheduling to guarantee QOS in WiMAX.

Formal definition of our scheduling model:

$$\text{Minimize } Z_k = \left(\sum_{1 \le k \le K} \left| \frac{\sum_{i=1}^{N} r_i x_{ik}}{x_{ik}} - D \right|^P \right)^{1/P}$$

$$\text{Subject to } \sum_{i=1}^{N} t_i x_{ik} \le u, 1 \le k \le K \qquad (1)$$

and

$$\sum_{i=1}^{N} p_{ij} x_{ik} \le m_j, 1 \le j \le M, 1 \le k \le K; \qquad (2)$$

where terms 1 and 2 refer to the time and power constraints during scheduling respectively.

x_{ik} are decision variables, where $1 \le i \le N$ and $1 \le k \le K$, x_{ik} is 1 if a subcarrier has been allocated, 0 otherwise. The decision of whether to grant the subchannel to the subcarrier is based on whether the subcarrier lies within the range of existing subcarriers for a subchannel. A criteria such as rejection of the subcarrier if it is directly adjacent to a previously allocated subcarrier within the same subchannel and acceptance if not so is used. This results in an improvement of SINR. *N* is the total number of subcarriers per user and *K* total number of users, r_i is the rate of each allocated subcarrier, *D* is the target rate for each user, t_i is the allocation time for the subcarrier, *u* is the allowable deadline for a user, p_i is the power allocation for each subcarrier, m is the maximum power allocation for user. C_i is the maximum allowable credits for a user. We define different penalty factors as follows:

Penalty factor for violating time constraint

$$\alpha = \sum_{k=1}^{k}\left(\max\left(0, \sum_{i=1}^{N} t_i x_{ik} - \mathrm{U} \right)\right)$$

Penalty factor for violating power constraint

$$\beta = \sum_{k=1}^{K}\sum_{j=1}^{M}\left(m_j - \sum_{i=1}^{N} p_{ij} x_{ik} \right)$$

$$\gamma = \sum_{k=1}^{K} \max\left(\delta_{\min} - \sum_{i=1}^{N} x_{ik}, 0 \right) + \max\left(0, \sum_{i=1}^{N} x_{ik} - \delta_{\max} \right)$$

In addition, in the third equation, we also define a constraint on the user using a large portion of a subcarrier repeatedly because this will deny opportunities to other users over this subchannel. We refer to such users as 'selfish users'. We initially assign some credits δ_k to each user *k*, which are incremented when each user gains additional subcarriers and decremented when the user loses them. We define credit thresholds $\delta_{\min}$ and $\delta_{\max}$ such that $\delta_{\min} \le \delta_k \le \delta_{\max}$ and γ is the penalty factor for violating the credit usage.

The fitness function of each user can be evaluated as: Minimize $H(x) = Z_k + w_1\alpha + w_2\beta + w_3\gamma$, where w_1, w_2, w_3 denote the weights for the penalty terms. For generation of the initial swarm, the particle gives more preference to items that have a closer rate to the target rate.

The mapping of the velocities to the probabilities can be carried out by the sigmoid function $S(V_{ij}) = 1/(1+e^{-v_{ij}})$ where positive velocities drive the bit towards 1 value while negative velocities towards the 0 bit values (see **Figure 3**).

The particle generation is based on the selection rule $|r_i - D|$ is minimum subject to $S(v_{ij}) = 1$ .Hence it gives more selection probability to users that have closer rate to the target rate and are represented by particles with positive velocities (see **Figure 4**).

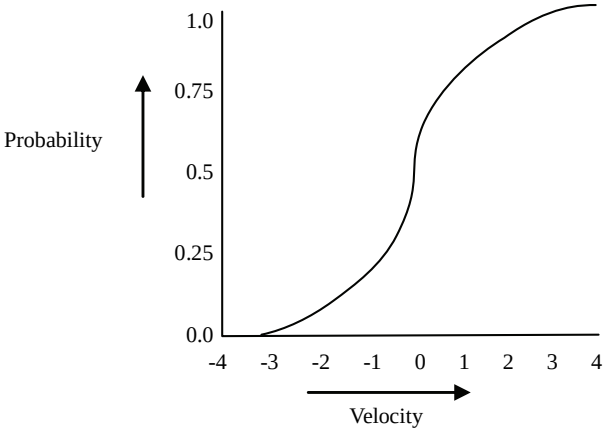

Figure 3. Sigmoid function for probability-velocity mapping.

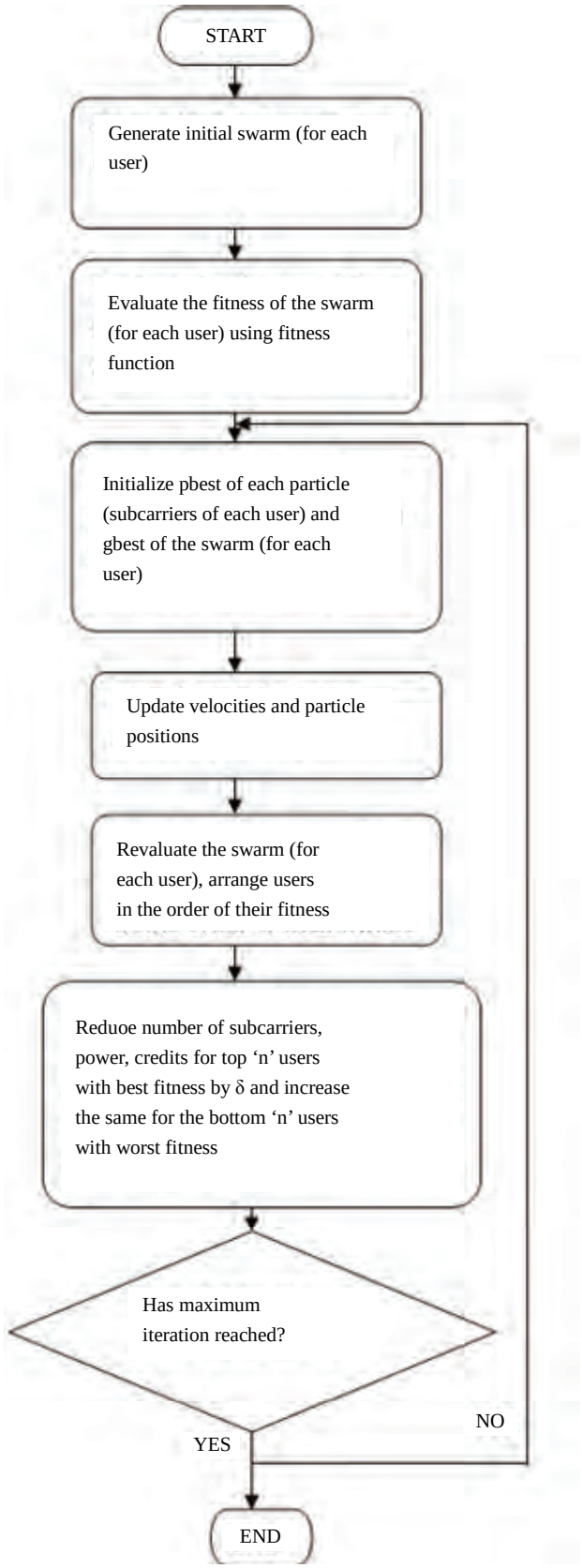

Figure 4. Subcarrier allocation and scheduling in PSORAS.

4. The Simulation Model and Results

We consider the downlink of an OFDMA system with N subchannels and K users. The time axis is divided into frames. A frame is further divided into S time slots, each of which may contain one or several OFDM symbols. The duration of a frame is set to be 5 ms, thus we can assume that the channel quality remains constant within a frame, but may vary from frame to frame. In our simulation, there are 1024 subcarriers, 1 to 50 users in the IEEE 802.16 OFDMA system. Each user transmits 80 bits in an OFDMA symbol. The modulation type in the OFDMA system is confined to QPSK, 16-QAM, 64-QAM. (see **Figures 5-7**)

Following are the simulation results for the variation in average throughput, fairness index and the average delay with the number of users. The results clearly indicate a reduction in the delay with the proposed swarm based approach compared to the Naïve allocation of subcarriers, *i.e.* allocation on availability basis in FDMA without considering variation in channel conditions. The results have been evaluated for different sets of target rates and target powers for the subcarriers and the priorities of users are varied after every 5 ms based on the calculated fitness. The throughput fairness index has been calculated as $\tau_n = (Th_{\max} - Th_{\min}) / Th_{\min}$, where $Th_{\min}$ and $Th_{\max}$ are the minimum and maximum values of throughput of each user over 'n' frames measured in bits.

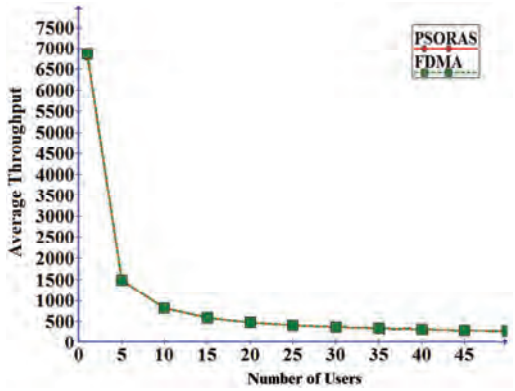

Figure 5. Number of users Vs. Average Throughput.

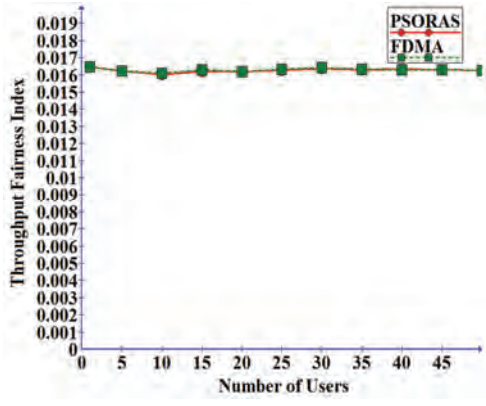

Figure 6. Number of users Vs. Throughput Fairness Index.

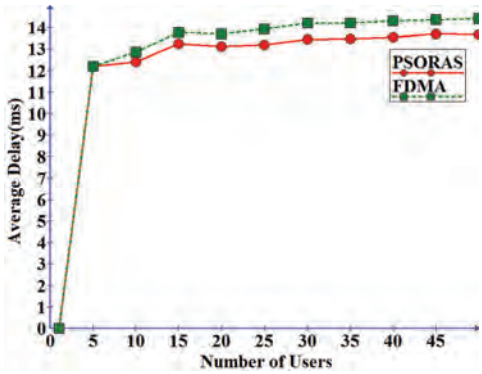

Figure 7. Number of users Vs. Average Delay.

5. Conclusions

Swarm optimization is increasingly finding its place in multiuser downlink MIMO scheduling, smart Antenna array systems etc. In our work, we have proposed a PSO-based fair Resource allocation and scheduling algorithm for the IEEE 802.16 System. We have compared our results with the static FDMA algorithm and have found it offers better delay characteristics with increasing number of users while still maintaining the fairness and throughput utilization. This makes the proposed scheme absolutely useful for real-time applications.

6. References

[1] D. Kivanc, G. Li and H. Liu, "Computationally Efficient Bandwidth Allocation and Power Control for OFDMA," *IEEE Transactions on Wireless Communications*, Vol. 2, No. 6, 2003, pp. 1150-1158.

[2] C. Wong, R. Cheng, K. Letaief and R. Murch, "Multiuser OFDM with Adaptive Subcarrier, Bit, and Power Allocation," *IEEE Journal on Selected Areas in Communications*, Vol. 17, No. 10, 1999, pp. 1747-1758.

[3] J. Jang and K. Lee, "Transmit Power Adaptation for Multiuser OFDM Systems," *IEEE Journal on Selected Areas in Communications*, Vol. 21, No. 2, 2003, pp. 171-178.

[4] G. Li and H. Liu, "On the Optimality of the OFDMA Network," *IEEE Communications Letters*, Vol. 9, No. 5, 2005, pp. 438-440.

[5] C. Mohanram and S. Bhashyam, "A Sub-optimal Joint Subcarrier and Power Aallocation Algorithm for Multiuser OFDM," *IEEE Communications Letters*, Vol. 9, No. 8, 2005, pp. 685-687.

[6] G. Manimaran and C. Siva Ram Murthy, "A Fault-Tolerant Dynamic Scheduling Algorithm for Multiprocessor Real-Time Systems and Its Analysis," *IEEE Transactions on Parallel and Distributed Systems*, Vol. 9, No. 11, 1998, pp. 1137-1152.

[7] R. Chen, J. G. Andrews, R. W. Heath and A. Ghosh, "Uplink Power Control in Multi-Cell Spatial Multiplexing Wireless Systems," *IEEE Transactions on Wireless Communications*, Vol. 6, No. 7, 2007, pp. 2700-2711.

[8] A. J. Page and T. J. Naughton, "Framework for Task Scheduling in Heterogeneous Distributed Computing Using Genetic Algorithms," 15*th Artificial Intelligence and Cognitive Science Conference*, Ireland, 2004, pp. 137-146.

[9] A. J. Page and T. J. Naughton, "Dynamic Task Scheduling Using Genetic Algorithms for Heterogeneous Distributed Computing," *Proceedings of the* 19*th IEEE/ACM International Parallel and Distributed Processing Symposium*, Denver, 2005, pp. 1530-2075.

[10] A. S. Wu, H. Yu, S. Jin, K.-C. Lin and G. Schiavone, "An Incremental Genetic Algorithm Approach to Multiprocessor Scheduling," *IEEE Transactions on Parallel and Distributed Systems*, Vol. 15, No. 9, 2004, pp. 824-834.

[11] A. Y. Zomaya and Y.-H. Teh, "Observations on Using Genetic Algorithms for Dynamic Load-Balancing," *IEEE Transactions on Parallel and Distributed Systems*, Vol. 12, No. 9, 2001, pp. 899-911.

[12] E. S. H. Hou, N. Ansari and H. Ren, "A Genetic Algorithm for Multiprocessor Scheduling," *IEEE Transactions on Parallel and Distributed Systems*, Vol. 5, No. 2, 1994, pp. 113-120.

[13] R. Eberhart and Y. Shi, "Particle Swarm Optimization: Developments, Applications and Resources," *IEEE International Conference on Evolutionary Computation*, Seoul, 2001, pp. 81-86.

[14] J. Kennedy, "The Particle Swarm: Social Adaptation of Knowledge," *IEEE International Conference on Evolutionary Computation*, Indianapolis, 1997, pp. 303-308.

[15] F. van den Bergh, "An Analysis of Particle Swarm Optimizers," PhD Thesis, University of Pretoria, 2001.

[16] J. Blondin, "Particle Swarm Optimization: A Tutorial," September 2009.

Int. J. Communications, Network and System Sciences, **2010, 3, 472-476**
doi:10.4236/ijcns.2010.35063 Published Online May 2010 (http://www.SciRP.org/journal/ijcns/)

Interoperability of Wireless Networks with 4G Based on Layer Modification

Dilshad Mahjabeen[1], Aminul Haque Mohammed Sayem[1], Anis Ahmed[2], Shahida Rafique[2]
[1]*Electrical and Electronics Engineering, Stamford University Bangladesh, Dhaka, Bangladesh*
[2]*Applied Physics, Electronics and Communication Engineering, University of Dhaka, Dhaka, Bangladesh*
E-mail: *dil_shadman@yahoo.com*
Received February 26, 2010; *revised March* 21, 2010; *accepted April* 23, 2010

Abstract

Fourth generation wireless communication systems feel the necessity of transparent and seamless user roaming with end-to-end connectivity. These systems also demand higher data rate, higher mobility support and QoS guarantees due to rapid development of wireless and mobile networks. These requirements open potentials for the operators to increase their service portfolio and for the users to experience context-rich and personalized services. Consequently the interoperability between different wireless network platforms emerges as a crucial necessity. Here focus is given to the significance of the network interoperability aspect based on layered approach and its role in the development towards 4G. This paper also gives an overview of the major 4G features and differentiating characteristics from other generations.

Keywords: 4G, Interoperability, Reconfigurability, Cooperativeness, Cross Layer

1. Introduction

Different generations of wireless communication improve the facilities for users day by day. The generations are classified into three groups namely 1G, 2G and 3G. 1G was completely analog and used for only voice transmission [1]. 2G networks were built mainly for voice services and slow data transmission. The cellular services combined with GPRS became 2.5G. This generation provides services such as Wireless Application Protocol (WAP) access, Multimedia Messaging Service (MMS) and for Internet communication services such as email and World Wide Web access. Although 2G is very popular and successful but it lacks single worldwide radio band technology standard as well as inefficient use of spectrum resources for bursty data. 3G networks represent the natural evolution from previous standards. In this case the networks enable network operators to offer users a wider range of more advanced services while achieving greater network capacity through improved spectral efficiency. 3G networks offer a greater degree of security than 2G predecessors. This generation (3G) allows simultaneous use of speech and data services and higher data rates. The services provided by 3G are wide-area wireless voice telephone, video calls, and wireless data, all in a mobile environment [2]. However 3G performances may not be sufficient to meet needs of future high quality applications. 3G does not provide mobility and service portability since it is based on primarily a wide-area concept. For this facility hybrid network (wireless LAN concept and cell or base-station wide area network design) is required. We need all digital packet networks that utilize IP in its fullest form with converged voice and data capability. And this great opportunity will be fulfilled by 4G wireless communications. In this paper we mainly deal with interoperability—the most important and special characteristic of 4G wireless communications. Section II describes the characteristics of 4G and the motivation for 4G other than 3G. This section also differentiates 4G from other generations. Section III focuses how 4G based on layered modification provide interoperability. Section IV describes about the role of cross layer at interoperable issue by 4G.

2. Journey towards 4G from 3G

The limitations of previous generation lead to improved generation. Their characteristics vary depending on some demanding features. Some of the differentiating characteristics are given in **Table 1**. The first generation of cellular networks consisted of analog systems capable of carrying only voice. 2G were packet switched transferring voice only**.** 3G is basically a circuit switched cellu-

lar network and so they have their own gateway to interpret IP from the back bone network. They also have their own protocol and interfaces for communication within themselves. To make this problem end, the only solution is 4G networks. Moreover, 3G is lacking from the followings: limitation of spectrum allocation, challenging gradually increasing bandwidth and high data rate for multimedia service, difficulty to roam across distinct service environment, lack of end environment, and lack of end to end continuous transmission mechanism [3]. To face these challenges, the new level of mechanism, 4G communications is introduced.

4G is an all IP packet switched network. This generation is the upgrade strategy in world of wireless communications. 4G system is expected to provide a comprehensive and secure IP based solution with facilities like voice, data and streamed multimedia. The key characteristics of 4G are global mobility, service portability, scalability and seamless handoff. It will be very friendly to comprehensive like "Anytime, Anywhere, Anyhow and Always-on" basis and at much higher data rates compared to previous generations. This will secure IP based solution with facilities like voice, data and streamed multimedia. Another special characteristic of 4G is the interoperability with existing wireless standards [4]. This generation provides integration across different network topologies *i.e.*, hybrid network architecture that integrates wireless wide area networks wireless.

3. Interoperability

With the rapid development of various wireless communication systems worldwide, there are also gradual changes in users' expectation and demand. Consequently the corresponding wireless networks work many fold at their capacity limits. So there is every chance of emergency crisis and/or disasters at the peak and crucial period. Thus interoperability can offer network providers with a possibility to switch between alternative wireless access networks. The basic theme of interoperability will yield the necessity of (user transparent) reconfigurability and

Table 1. Comparison of different generations.

Properties	2G	3G	4G
Network Architecture	LAN,	Wide area cell-based	Hybrid -
Driving Architecture	Only voice	dominantly voice; also data	Converged data and voice over IP
Switching	Packet switched	Circuit and Packet	All digital with packetized voice
Radio Access	FDMA, TDMA, CDMA	WCDMA, CDMA2000, IWC-136	MC-CDMA, OFDMA
Database	HLR,VLR, EIR, AuC	EHLR, VLR, EIR, AuC	EHLR, VLR, EIR, AuC
Data rates	9.6 to 384 kbps	Up to 2 Mbps	100Mbps
Roaming	Restricted	Global	Global
Compatible	Not compitable to 3G	Compitable to 2G, 2G+ and blu-tooth	Compatible to 3G
Handsets	Dual mode TDMA and CDMA Voice and data terminals	Multiple mode voice, data, vedio terminals	Multiple mode voice, data streamed video at higher data rates.
Applica-tions	SMS, Internet	Internet, SMS	Internet, MMS, Mutimedia, HDTV, M TV
Bandwidth	25 MHz	5-20 MHz	100 MHz
Frequency Band	Tri Band800, 900,1800,1900 MHz	Dependent on country (1800-2400 MHz)	Higher frequency bands (2-8 GHz)
Component design	Optimized antenna design	Optimized antenna design, multi-band adapters	Smarter Antennas, software multiband and wideband radios
FEC tech	Convolutional coding	Convolutional rate 1/2, 1/3	Concatenated coding scheme
IP	No IP Connection	A number of air link protocols, including IP 5.0	All IP (IP6.0)

cooperativeness in various communication systems tunneling towards the 4G journeys.

3.1. Reconfigurability

The reconfigurable interoperability can be done at the network level, the user level or both. This will be very helpful for both the network providers and the users' perspective. The reconfigurable interoperability will provide selection between alternative wireless access networks. The selection could be based on several reconfigurable interoperability issues such as:

- Channel state;
- Outage probability;
- Vertical handover probability;
- Users' QoS requirements;
- Context awareness;
- Load sharing and distribution between different spatially coexisting wireless networks;
- Efficient spectrum sharing;
- Preferred gateway selection and network discovery and
- Congestion control.

The mechanism of reconfigurability refers not only to the physical layer, but span across the entire protocol stack (including cross-layer optimizations). The reconfigurable interoperability of the heterogeneous 4G system will lead to more efficient end-to-end connectivity and service delivery in heterogeneous environments, easier worldwide roaming and dynamic adaptation to regional contexts, enhanced personalization and richer services. At the network level, the reconfigurable interoperability will offer network providers with a possibility to choose between alternative wireless accesses networks at minimal cost. At the user level, the interoperability of the heterogeneous 4G systems will provide more efficient end-to-end connectivity and service delivery in heterogeneous environments, easier global roaming and dynamic adaptation to regional contexts, enhanced personalization and enriched services [5].

3.2. Cooperativeness

3G specify the PHY and MAC of the radio link. This alone is not adequate to build an interoperable broadband wireless network. Interoperable networks involve the following issues:

- End-to-end service such as IP connectivity;
- Session management;
- Security;
- QoS;
- Mobility;
- Connectivity issues;
- Self organization;
- Authentication, Authorization, and Accounting.

Cooperativeness comes to ensure these issues. This means connectivity between all the entities of a network in a consistent manner across all access technologies for any service. In 4G, a cooperative network (CoNet) consists of three distinct layers such as application, connectivity and access that form logically separate subsystems. Each of the layers can be further divided into different sub layers as shown in the **Figure 1**. The layers should have well defined interfaces and be functionally independent of each other for an approach is required to ensure easy adaptation of heterogeneous access technologies, related technology changes, and flexible support for rapid service innovation. Actually the connectivity layer plays an important role for cooperation across various realizations of networks, which in turn ensures the interoperability. This layer will be independent of the various transport technologies used to link the nodes of the network together. Finally, the user will enjoy seamless roaming across different access technologies and administrative domains without any manual user intervention [6].

One of the 4G's major goals is integration, which offers seamless interoperability of different types of wireless networks with the wire line backbone. Some of the available attempted heterogeneous interoperable integrated architecture are: a loosely-coupled, Mobile IPv6 (MIPv6)-based GPRS/WLAN/LAN heterogeneous network, implementation of IPv6-based mobility-enabled network architecture with Authentication, Authorization, Accounting and Charging (AAAC) services and support for Quality of Service (QoS) [7].

3.3. Access Network

From the point of view of access network, 3G access

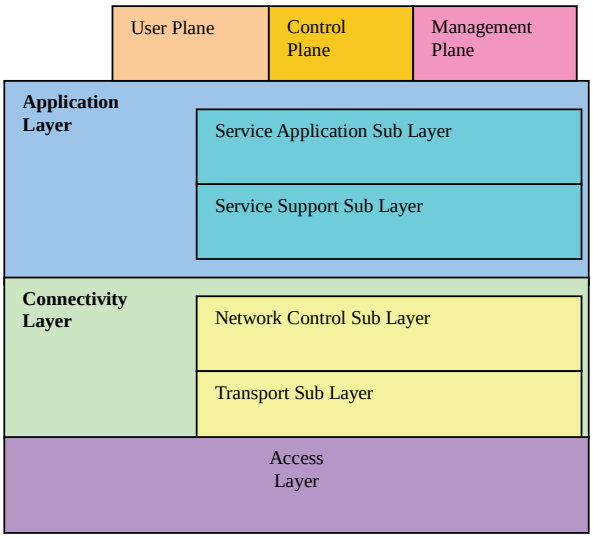

Figure 1. Layers of 4G providing interoperability.

network uses WCDMA, cdma 2000. But these are complicated and require more protocol for system structure coverage. On the other hand, 4G access network uses the OFDMA, 3 × RTT and MIMO antennas. Also hybrid multiple access technique is used for high speed mobile or nomadic user, data or voice traffic, call centre or boundary conditions [8]. But the abovementioned access techniques currently do not interoperate LAS CDMA (Large area synchronized CDMA) access technique solves this problem. LAS CDMA will be compatible with all current and future standards and there is a relatively easy transition from the existing system to LAS CDMA. Link air emphasizes that LAS CDMA will accommodate all the advanced technology planned for 4G. LAS CDMA will also further improve the prevailing the techniques like WCDMA, 3 × RTT [1].

4. Cross Layer

In wireless network, interoperable systems provide coordination among layers. Cross-layer design or "cross-layering" provides functionalities associated with the original layers to allow coordination, interaction and joint optimization of protocols crossing different layers. In order to provide improvement in terms of some performance metric, the cross-layer approach to system design derives from the interaction among protocols operating at different layers of the protocol stack. The main advantage deriving cross layering paradigm is the modularity in protocol design, which enables interoperability and improved design of communication protocols. An example of cross layer approach for interoperability is shown in **Figure 2**.

MAC-PHY Cross Layer: The physical layer transmits power, which can be tuned by the Medium Access Control (MAC) layer to increase the range of transmission.

NET–MAC Cross Layer: Network layer could use MAC layer events like handoff to reduce Mobile-IP hand-off latency for seamless connectivity.

NET-MAC-PHY Cross Layer: This layer provides seamless connectivity and enhanced transmission range [9].

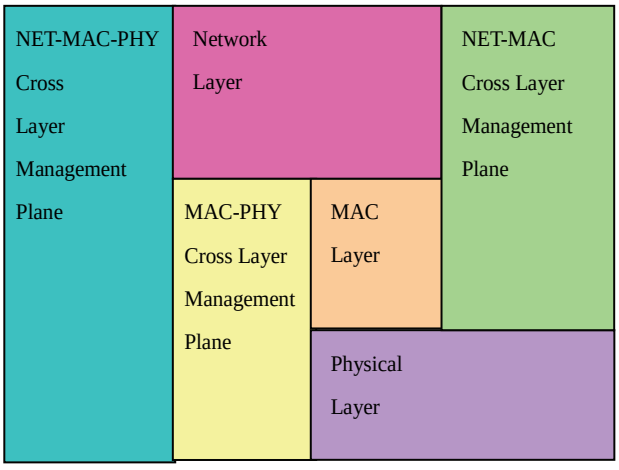

Figure 2. Cross-Layer approach for Interoperability.

5. Conclusions

For higher data rates, higher mobility support and seamless communication 4G utilizes a common platform that will unify a variety of evolving access technologies, uninterupted internetworking and interoperability solutions and adaptive multimode user terminals. Reconfigurable, co-operative and cross layer architecture based on layered approach for interoperability are mentioned here. The co-net architecture also provides end to end services, security and self organization. More over using multiple descriptions coding at application layer combined with orthogonal frequency division multiplexing at the link level provides robustness against hostile wireless channels. Negotiation between application, data link control and physical layer is exploited to increase user quality of service in terms of picture signal to noise ratio and bandwidth efficiency. 4G networks suffer from the lack of Layer 2 QoS provisioning in heterogeneous networks, mainly due to the non-uniform nature of the QoS models and service interfaces among different wireless technologies. Other problem is the lack of coordination of L3 QoS with L2 QoS and mobility. All these problems can be solved by introducing QoS abstraction layer in between layer 2 and 3 in the control plane which will be discussed in our next paper.

6. References

[1] "Emerging Wireless Technologies: A Look into the Future of Wireless Communications-Beyond 3G". http://www.safecomprogram.gov/NR/rdonlyres/5C74C631-ACF6-433F-B313-C

[2] D. I. Axiotis, F. I. Lazarakis and C. Vlahodimitro, "Mobility and Traffic Parameters for Simulating Interoperating UMTS and HIPERLAN/2 MTMR Enabled Networks," *The* 57*th IEEE Seminual Vehicular Technological Conference*, Jeju,Vol. 4, 2003, pp. 2745-2749.

[3] S. Hussain, Z. Hamid and N. S. Khattak, "Mobility Management Challenges and Issues in 4G Heterogenous Networks," ACM, New York, USA, 2006.

[4] "Evolution of wireless connection". http://4G-wirelessevolution.tmcnet.com/topicsmostigov/my/mosti/images/stories/DICT/policy

[5] L. M. Gavrilovska and V. M. Atanasovski, "Interoperability in Future Wireles Communications Sytems: A Roadmap to 4G," *Microwave Review*,Vol. 13, No. 1, 2007, pp. 19-28.

[6] "Cooperative Networks of 4G". www-scf.usc/edu/~ssaraf/ EE555.pdf

[7] L. Gavrilovska, V. Atanasovski, V. Rakovic, O. Ognenoski and A. Momiroski, "Providing Interoperability in Heterogeneous Environments towards 4G," *ELMAR*, 50*th International Symposium*, Zadar, Vol. 1, 2008, pp. 223-226.

[8] L. D. Uomo and E. Scarrone, "All-IP 4G Network architecture for Efficient Mobility and Resource Management," 5*th International Symposium on Wireless Personal Multimedia Communications*, Honolulu, Vol. 2, 2002, pp. 591-595.

[9] D. Kliazovich, M. Devetsikiotis and F. Granelli, "Formal Methods in Cross Layer Modeling and Optimization of Wireless Networks," In: Kotsopoulos, S. and Ioannou, K. Ed., *Handbook of Research on Heterogeneous next Generation Networking*: *Innovations and Platforms*, 2009, pp. 1-24.

Int. J. Communications, Network and System Sciences, **2010, 3, 477-482**
doi:10.4236/ijcns.2010.35064 Published Online May 2010 (http://www.SciRP.org/journal/ijcns/)

Research on Access Network Intrusion Detection System Based on DMT Technology

Lingxi Wu, Jie Zhan, Qiange He, Shuiyan He
Hunan University of Science and Technology, Xiangtan, China
E-mail: *lxwhsy@126.com*
Received January 19, 2010; *revised March* 1, 2010; *accepted April* 7, 2010

Abstract

Analysis is done on the inter-carrier interference (ICI) that caused by multi-carrier communication system frequency offset. The application model of DFT/IDFT in ADSL access network is analyzed further; the hardware detection and software analysis scheme of the system are proposed for the accessing network. Experiments have proved that monitoring system can filter the network data flow and carry on statistical and analysis, achieving real-time monitoring.

Keywords: DMT, ICI, Intrusion Detection, DFT/IDFT

1. Introduction

The Discrete Multi-Tone DMT () technology has been applied successfully on the ADSL (Asymmetric Digital Subscriber Line) transmission system, and has developed the broadband transmission system that based on Twist-Pair. The problems of network detection and monitoring will be inherent in the development of network, yet the rapid development of the network has been ahead of the real-time monitoring. To solve it, data detection system based on DMT technology has been studied systematically, and data acquisition equipment has been devised, which can achieve filtering analysis and statistics of the network data stream with no influence on the user and the phone company end of the line.

2. Multi-carrier Communication System Modeling

QAM (Quadrature Amplitude Modulation) is the basis of DMT, Model use multiple QAM constellation diagram encoders, and each constellation diagram encoder use a different carrier frequency, The DMT code element that were formed by summing all the carries transmitted through the channel. If the receiver can separate sine waves from cosine waves on different frequencies, each wave can be decoded independently, the method of encoded and decoded are consist with the QAM signals; to ensure no interference from f_1 to f_n sub-channel, we must make sure that a sine and cosine wave in one sub-channel are orthogonality with any other sub-channels, and its formula is as follow [1,2]:

$$\int_0^T \cos(n\omega t)\cos(m\omega t)dt = 0$$

$$\int_0^T \cos(n\omega t)\sin(m\omega t)dt = 0$$

$$\int_0^T \sin(n\omega t)\sin(m\omega t)dt = 0$$

n and m are unequal integers, and ω is the base rate.

By the expression of orthogonality, we concluded the each sub-channel frequency must be an integral multiple of base frequency, and the code element period T is reciprocal of the base frequency or an integral multiple of the reciprocal of the base frequency. Two situations would appear: First, the frequency offset is an integral multiple of sub-carrier; second, the frequency offset is not an integral multiple of sub-carriers; both of two situations will make system characteristics deteriorate. Assuming the number of carrier is limited, **Figure 1** is a block diagram of a DMT communication system model [3], and according to the system, we make the following discussion:

During the 'i' symbol cycle, Assuming the original data symbol is $\{a_{0,i}, a_{1,i}, \ldots, a_{n-1,i}\}$, after IDFT calculate, we can get:

$$b_{k,i} = \frac{1}{N}\sum_{l=0}^{N-1} a_{l,i} \exp\left(\frac{j2\pi lk}{N}\right) \quad (1)$$

Therefore, we can get the output signal x(t) as follow:

$$\mathrm{x}(t) = \exp(j2\pi f_c t)\sum_{k=0}^{N-1} b_{k,i}\, p\left(t - \frac{kT}{N}\right) \quad (2)$$

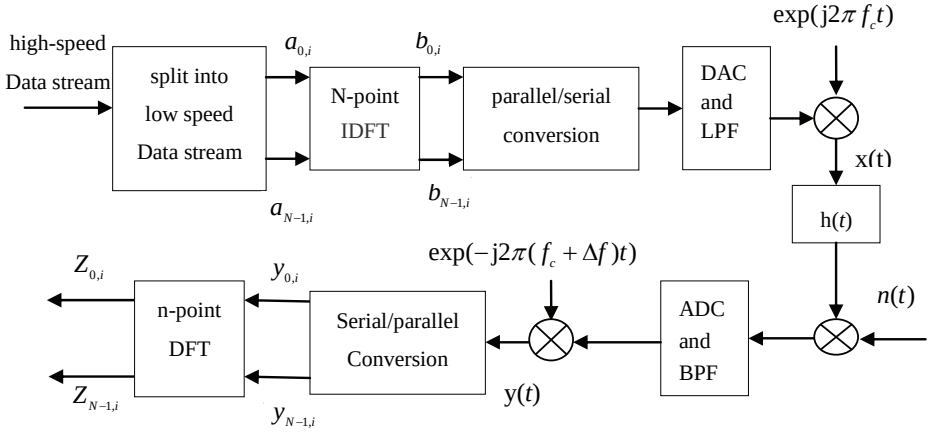

Figure 1. Multi-carrier communication system modeling.

f_c represent the carrier frequency, $p(t)$ represent the impulse response of low-pass filter used in the transmitter system, but there is the frequency deviation Δf at the receiving end, after down-conversion and low-pass filter the $y(t)$ signal is :

$$y(t) = \exp(j2\pi f_c t + \theta_0)\sum_{k=0}^{N-1} b_{k,i} q\left(t - \frac{kT}{N}\right) \tag{3}$$

$q(t)$ represent the combination impulse response get by multiplying low-pass filter of the transmitter and band-pass filter of the receiver, θ_0 is the phase difference between receiver local oscillator and RF carrier. If $q(t)$ can meet the Nyquist criterion at the moment kT/N, then we sample $y(t)$ at the same time.

We can get:

$$y_{k,i} = \exp(j\theta_0) b_{k,i} \exp\left(\frac{j2\pi\Delta f k T}{N}\right) \tag{4}$$

According to the DFT formula,

$$Z_{m,i} = \sum_{k=0}^{N-1} y_{k,i} \exp\left(-\frac{j2\pi km}{N}\right), (m = 0,1,\ldots,N-1) \tag{5}$$

Substituting (1) and (4) into (5), we can get:

$$Z_{m,i} = \frac{1}{N}\exp(j\theta_0)\sum_{l=0}^{N-1} a_{l,i}\sum_{k=0}^{N-1}\exp\left(\frac{j2\pi k(l-m+\Delta fT)}{N}\right) \tag{6}$$

According to the sum formula $\sum_{k=0}^{N-1} u^k = \frac{1-u^N}{1-u}$, (1-6) can be simplified:

$$Z_{m,i} = \frac{1}{N}\exp(j\theta_0)\sum_{l=0}^{N-1} a_{l,i}\left[\frac{1-\exp\left(j2\pi(l-m+\Delta fT)\right)}{1-\exp\left(\frac{j2\pi(l-m+\Delta fT)}{N}\right)}\right] \tag{7}$$

From:

$$\begin{aligned} 1-\exp(j2\varphi) &= [\exp(-j\varphi)-\exp(j\varphi)]\exp(j\varphi) \\ &= -j2\sin\varphi\exp(j\varphi) \end{aligned} \tag{8}$$

Make: $\varphi_1 = \pi(l-m+\Delta fT)$

$$\varphi_2 = \frac{\pi(l-m+\Delta fT)}{N},$$

(8) can be express as follow：

$$\begin{aligned} Z_{m,i} &= \frac{1}{N}\exp(j\theta_0)\sum_{l=0}^{N-1} a_{l,i}\left(\frac{-j2\sin\varphi_1\exp(j\varphi_1)}{-j2\sin\varphi_2\exp(j\varphi_2)}\right) \\ &= \frac{1}{N}\exp(j\theta_0)\sum_{l=0}^{N-1} a_{l,i}\frac{\sin\varphi_1}{\sin\varphi_2}\exp(j(\varphi_1-\varphi_2)) \end{aligned}$$

$$Z_{m,i} = \exp(j\theta_0)\sum_{l=0}^{N-1} a_{l,i} c_{l-m} \tag{9}$$

Among of them,

$$c_{l-m} = \frac{1}{N}\frac{\sin(\pi(l-m+\Delta fT))}{\sin\left(\frac{\pi(l-m+\Delta fT)}{N}\right)}\exp\left(j\pi\frac{(N-1)(l-m+\Delta fT)}{N}\right) \tag{10}$$

$$c_0 = \frac{1}{N}\frac{\sin(\pi\Delta fT)}{\sin\left(\frac{\pi\Delta fT}{N}\right)}\exp\left(j\pi\Delta fT\frac{N-1}{N}\right) \tag{11}$$

c_0, c_1, …, c_{n-1} are complex weighting coefficients, corresponding to input data symbols $a_{0,i}, a_{1,i}, \cdots, a_{n-1,i}$, then we can get the symbols transmitted in mth sub-channel as follow (N is the number of coefficients):

$$\begin{aligned} Z_{m,i} &= \exp(j\theta_0)\sum_{l=0}^{N-1} c_{l-m} a_{l,i} \\ &= \exp(j\theta_0) c_0 a_{m,i} + \exp(j\theta_0)\sum_{\substack{l=0 \\ l\neq m}}^{N-1} c_{l-m} a_{l,i} \end{aligned} \tag{12}$$

The first item of the formula is data symbol of weighted mathematical expectation, the second item is the ICI caused by Δf. If $\Delta f = 0$, then $Z_{m,i} = \exp(j\theta_0)\, a_{m,i}$, ($m = 0, 1,\ldots,N-1$). Note: Each complex symbol will be influenced by the phase deviation factor θ_0. If $\Delta f \neq 0$, the inter-channel interference (ICI) will occur. **Figure 2** shows the relationship between the real part, imaginary part, modulus of the complex weighting coefficient and the sub-carrier number N in case of the two kinds of $\Delta f\ T$. When the frequency deviation increases, the stable zone quickly narrows, the modulus value rapidly increases, indicating ICI increases significantly

3. ADSL System Based on Multi-carrier Technology

According to the model [3,4], assume T is the cycle, we derive the waveform expression that added up sine and cosine waves :

$$S(t) = \begin{cases} X_n \cos(n\omega t) + Y_n \sin(n\omega t) & 0 \le t \le T \\ 0 & else \end{cases} \quad (13)$$

The waveform shows the influence that a single sub-channel n operate on DMT code element, according to Nyquist theorem, sampling the signal, sampling frequency is $2Nf$, sampling value is:

$$\begin{aligned} S_K &= X_n \cos(n\omega \frac{k}{2Nf}) + Y_n \sin(n\omega \frac{k}{2Nf}) \\ &= X_n \cos(\frac{\pi nk}{N}) + Y_n \sin(\frac{\pi nk}{N}) \quad 0 \le k \le 2N-1 \end{aligned} \quad (14)$$

Make the Discrete Fourier Transform (DFT) to these $2N$ points as follow:

$$\begin{aligned} S_m &= \sum_{k=0}^{2N-1} \left[X_n \cos(\frac{\pi nk}{N}) + Y_n \sin(\frac{\pi nk}{N}) \right] e^{-j2\pi mk/2N} \\ &= \sum_{k=0}^{2N-1} \left[X_n \frac{e^{jn\pi k/N} + e^{-jn\pi k/N}}{2} + Y_n \frac{e^{jn\pi k/N} - e^{-jn\pi k/N}}{2j} \right] \\ &\quad e^{-j\pi mk/N} \\ &= \begin{cases} N(X_n - jY_n) & m = n \\ N(X_n + jY_n) & m = 2N\text{-}n \\ 0 & else \end{cases} \end{aligned} \quad (15)$$

From (14) and (15), we conclude that the output can be mapped to a complex number by making DFT to the signal, the value of encoder X-axis (cosine amplitude) represents the real part of the complex number, the value of Y-axis (sine amplitude) represents the imaginary part of the complex number, then it is a way to generate DMT code element. If make Inverse Fourier transform to S_m, we can deduce S_k:

$$\begin{aligned} S_K &= \frac{1}{2N} \sum_{m=0}^{2N-1} S_m e^{j2\pi mk/2N} \\ &= \frac{1}{2} \left[(X_n - jY_n) e^{j\pi mk/N} + (X_n + jY_n) e^{j\pi(2N-n)k/N} \right] \\ &= \frac{1}{2} \left[(X_n - jY_n)(\cos(\frac{\pi nk}{N}) + j \sin(\frac{\pi nk}{N})) \right. \\ &\quad \left. + (X_n + jY_n)(\cos(\frac{\pi nk}{N}) - j \sin(\frac{\pi nk}{N})) \right] \\ &= X_n \cos(\frac{\pi nk}{N}) + Y_n \sin(\frac{\pi nk}{N}) \quad 0 \le k \le 2N-1 \end{aligned} \quad (16)$$

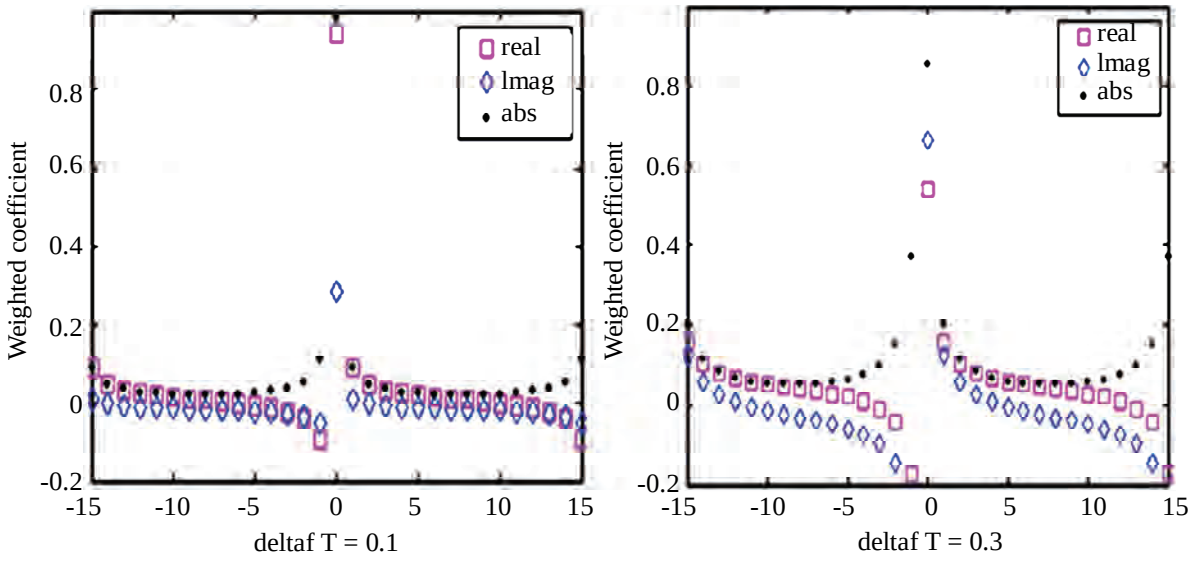

Figure 2. Carrier frequency deviation and synchronization features.

The DMT modem can be achieved with DFT and IDFT. From (13) it can be derived the complex number $N(X_n - jY_n)$ to the n th sub-channel, express that a complex number can represents a sub-channel of DMT, N sub-channels have N complex numbers, plus N conjugate complex numbers $(X_n + jY_n)$, we can get $2N$ complex numbers, from (14) ,we can get S_k through making IDFT to $2N$ complex numbers. So we can get DMT modulation, demodulation program, this program has been applied to ADSL modem. In the ADSL, ATU-C downstream modulator uses 256 windows, which is 256 complex numbers, the interval of windows is 4.1325 kHz. Frequency range is from 4.3125 kHz to 1.104 MHz, according to code analysis, the IDFT of downstream DMT can be expressed as:

$$S_K = \sum_{m=0}^{511} S_m e^{j\pi mk/256}, \ k = 0,\ldots,511 \tag{17}$$

S_m is the complex number value or expanded conjugate complex number made by QAM constellation encoding for each sub-carrier, S_k is the time-domain sample sequence after DMT modulation, and the time-domain waveform can be generated after parallel-serial conversion and DAC.

The upstream DMT modulation of ATU-R uses 32 windows, 32 complex numbers represent the coding results of each sub-channel constellation, the audio interval is 4.3125 kHz, frequency range from 4.3125 kHz to 138 kHz. According to the code analysis that the DMT of IDFT in the upstream can be expressed as:

$$S_K = \sum_{m=0}^{63} S_m e^{j\pi mk/64}, \ k = 0,\ldots,63 \tag{18}$$

4. Research on Intrusion Detection System

The principle is shown in **Figure 3**. The structure of collector mainly consists of the DSLAM Simulation Module [5-7], Modem Simulation Module and Data Interface Module and so on. The end of ADSL Modem accesses to the DSLAM simulation module of data acquisition equipment, the end of Telecommunications Bureau accesses to the ADSL Modem Simulation Module of data acquisition. After the upstream signals input DSLAM

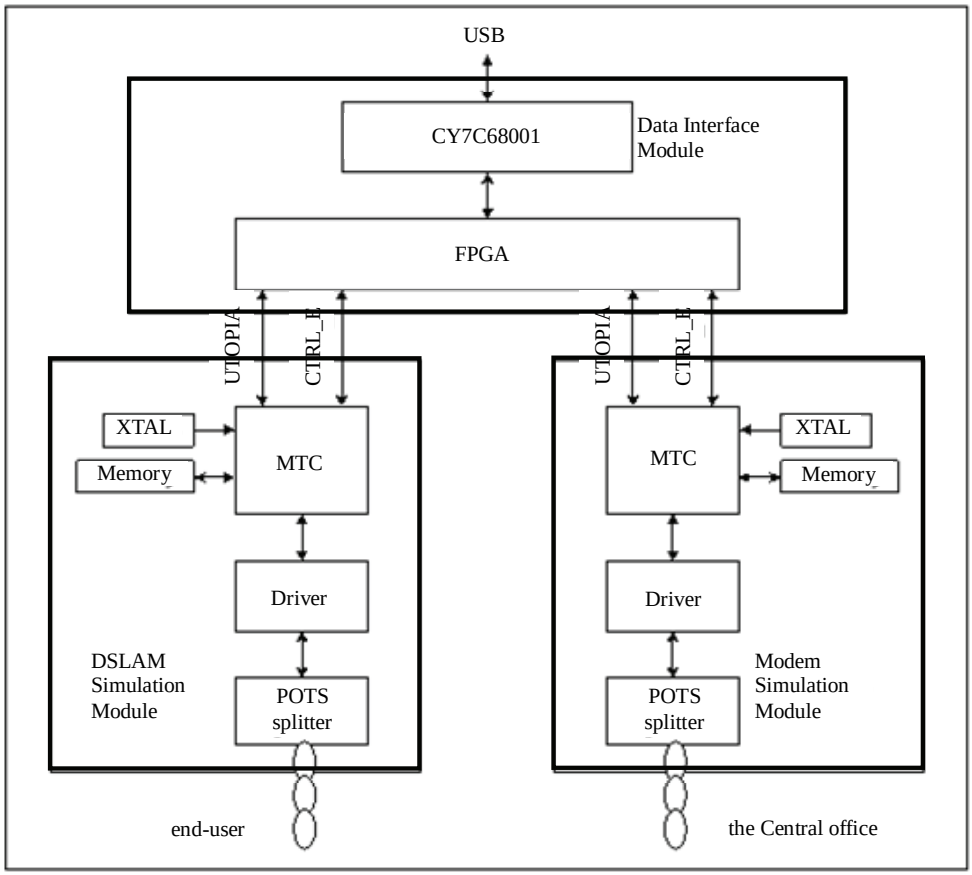

Figure 3. Hardware block diagram of data acquisition system.

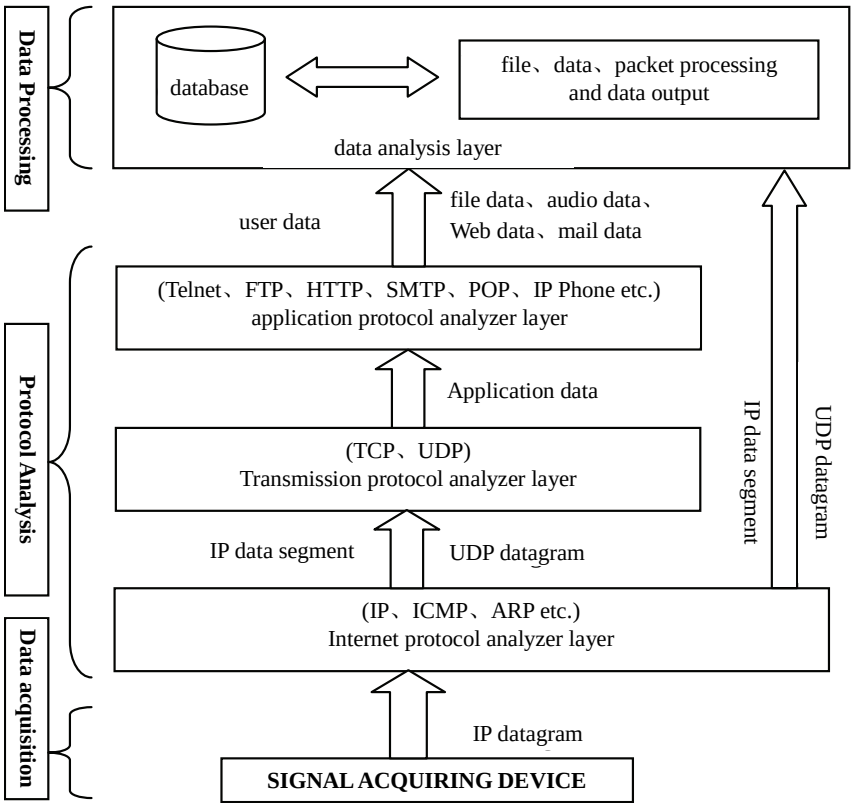

Figure 4. System software descriptions.

simulation module, we complete DMT demodulation and send the demodulated signal to the interface module, then send to the computer by USB interface. Meanwhile, the upstream signal is also sent to the ADSL Modem Simulation Module, complete the transmission of upstream data to Telecommunications Bureau. After downstream signals input the ADSL Modem Simulation Module, we complete DMT demodulation and send the demodulated signal to the interface module, and then send to the computer through USB interface. Downstream signal is also sent to DSLAM Simulation Module, and complete the transmission of downstream signal to the user. The normal signals of consumer are connected directly with the dedicated POTS access between the two simulation modules. So, the device joined Telecommunications Bureau and user ADSL Modem, it will not affect the user's normal voice and data communications, both of them are not aware of the existence of the device. Through the UTOPIA interface [8,9], we extract the cell, and encapsulate the cell to get USB packets, and transmit to the computer through the USB interface to analyses the data, the process includes two parts (data processing and protocol analyzer), in order to restore the data effectively and accurately from the obtained data, we must make out the software , according to the system request the software hierarchy is shown in **Figure 4**.

5. Conclusions

The distance of data transmission on the Twist-Pair is limited, and the variety of circuit characteristics will affect the status of circuit connection which may cause normal users can't explore the Internet, Meanwhile network data transferring is bidirectional and the upstream and downstream data transferring are asymmetry that makes a great deal of difference from other wired or wireless audio and video signal transmission. In this paper, the data acquisition system is a data receiving system. In process of the upstream and downstream data processing, there are several technical difficulties in data extraction, separation, storage, etc, and our program can solve these problems well. It brings new solutions to the data acquisition system for detecting network data transmission and eliminating network failure, particularly it can solve the problems of monitoring the real-time.

6. Acknowledgements

This paper is supported by Natural Science Foundation

of Hunan Provincial, China (Grant No. 07JJ6128).

7. References

[1] W. Stallings, "Data and Computer Communications," Prentice Hall Upper Saddle River, New Jersey, 2000.

[2] T. Pollet and M. Moeneclaey, "Synchronization of OFDM Signals," *IEEE Globecom'*95, Singapore, Vol. 3, November 1995, pp. 2054-2058.

[3] H. V. Poor, "Iterative Multiuser Detection," *IEEE Singal Processing Magazine*, Vol. 21, No. 1, 2004, pp. 81-88.

[4] "ITU-T Recommendation G.992.3, Asymmetric digital subscriber line transceivers2 (ADSL2)," July 2002.

[5] J. Heinanen, "RFC1483: Multi-protocol Encapsulation over ATM Adaptation Layer 5," RFC Editor, United States, 1993.

[6] L. X. Wu, Z. P. Huang, G. L. Tang and L. Y. Pan, "Design and Realization of Data Acquisition Access Circuit Based on ATM Network," *Telecommunication Engineering*, Vol. 44, No. 6, 2004, pp. 107-110.

[7] AFE-20154 Data Sheet rev.1- June 1999.

[8] L. X. Wu and T. F. Jiang, "Research and Aealization of Real-time Data Acquisition System Based on ADSL Access Network," *Engineering Journal of Wuhan University*, Vol. 39, No. 6, 2006, pp. 113-116.

[9] "CY7C68001 EZ-USB SX2™ High-Speed USB Interface Device," Cypress Semiconductor Corporation, July 2003, pp. 1-50.

Int. J. Communications, Network and System Sciences, **2010, 3, 483-487**
doi:10.4236/ijcns.2010.35065 Published Online May 2010 (http://www.SciRP.org/journal/ijcns/)

Scientific Research

Synchronization in Wireless Networks for Practical MIMO-OFDM Systems

Muhammad Khurram Kiyani[1], Muhammad Usman Ahmed[2], Asim Loan[1]
[1]*Department of Electrical Engineering, UET, Lahore, Pakistan*
[2]*Department of Computer Sciences, LUMS, Lahore, Pakistan*
E-mail: {*khurramkiyani, muahmed*}*@gmail.com, aloan@uet.edu.pk*
Received February 21, 2010; *revised March* 24, 2010; *accepted April* 25, 2010

Abstract

In this paper a frequency offset estimation technique for Wireless Local Area and Wireless Metropolitan Area Networks is presented. For frequency offset estimation, we have applied a low-complexity frequency offset estimator for simple AWGN channels to fading channels for MIMO-OFDM systems. Simulation results have shown that the performance of the proposed estimator is better than the low complexity frequency offset estimator designed for AWGN channels.

Keywords: Synchronization, Multiple Input Multiple Output, Orthogonal Frequency Division Multiplexing, Wireless Local Area Networks, Wireless Metropolitan Area Networks, Stanford University Interim Channels

1. Introduction

A lot of research has been carried out in carrier frequency offset estimation for Single Input Single Output (SISO) Orthogonal Frequency Division Multiplexing (OFDM) systems but comparatively less work has been done in Multiple Input Multiple Output (MIMO) OFDM systems. In [1], timing metric for frame synchronization and frequency offset estimation in OFDM is proposed in the downlink. In [2], a coarse timing synchronization is carried out by using autocorrelation and then Carrier Frequency Offset (CFO) is estimated by performing precise autocorrelation only on samples that have been compensated for coarse timing synchronization. Both [1] and [2] have sufficiently explored OFDM but they do not incorporate MIMO. However, in [3], a novel frequency synchronization scheme is presented which uses repeated pseudo-noise training sequences to correct CFO in MIMO-OFDM systems. Also, in [4], integer CFO and fractional CFO are estimated for MIMO-OFDM systems through special training sequences by solving complex or real polynomial corresponding to the cost function. Although both [3] and [4] have dovetailed MIMO with OFDM systems but they lack the practicality as they have not incorporated any particular standard. In this paper we have extended the work of Luise & Reggia- nnini (L & R), [5], by adapting their AWGN single channel frequency estimator to multipath fading channels using IEEE 802.16-2004 Standards [6], and IEEE 802.11n Standards [7]. The technique used is non-recursive as realistic MIMO scenarios entail changing channels with information being sent in bursts corresponding to the duration of the coherence time of the channel.

The remaining paper is organized as follows. Section 2 covers the details of system model. Section 3 gives the description of the proposed frequency offset estimator and Section 4 explains the results obtained through simulations. Section 5 finally gives the conclusion.

2. System Model

A frequency offset can be introduced by relative motion between the transmitter and the receiver (Doppler spread) and by the inaccuracies in the Local Oscillator (LO). Channel estimation in MIMO-OFDM system is very sensitive to any frequency offset in the down converted signal because frequency offset introduces a time dependant factor that degrades the estimation of channel response matrix *H*. Therefore accurate frequency offset estimation would result in a better channel estimate and a more robust system.

Generally, a multipath fading channel is changing therefore the transmission is done in packets with the packet length being governed by the coherence time of the channel, *i.e.*, the time for which the channel response

does not change. In packet based communications, the channel response matrix H must be estimated for each packet. This is generally done by using a training sequence known to the receiver. We have used SUI Channels, [8], here as multipath fading channels and a preamble specified in IEEE 802.16-2004 and IEEE 802.11n as a training sequence for WMAN and WLAN respectively. Our proposed algorithm estimates a constant frequency offset over a length of symbols for every packet.

In MIMO, the signal received at each receiving antenna is the superposition of the transmitted signals that from different transmit antennas. Thus, the training signal for each transmit antenna needs to be transmitted without being interfered by the others. **Figure 1** shows three transmission patterns that avoid interfering with one another: independent, scattered and orthogonal patterns. For the sake of brevity we will only discuss the independent pattern. The independent pattern transmits training signal from one antenna at a time while the other antennas are silent, thus guaranteeing orthogonality, in the time domain, between each training signal. The independent pattern is often the most appropriate for MIMO-OFDM, since the preamble is usually generated in the time domain.

To encode the training sequence we have used the independent pattern and assigned to each transmit antenna a standard training sequence. This means that at a given time only one transmit antenna is transmitting the training sequence as shown in **Figure 2**. We have also assumed that the distance between transmitting antennas is less than $\lambda/2$ and they all encounter the same channel statistics.

3. Proposed Frequency Offset Estimation Technique

The training sequence symbol is transmitted from the m^{th} transmit antenna and received on any of the receive antenna. The kth sampling index of this received symbol can be written as:

$$r(k) = h_m c_k e^{j\left[2\pi vkT+q\right]} + n(k) \quad for\, 1 \le k \le N. \quad (1)$$

In the above equation, h_m denotes the complex channel coefficient between the mth transmit antenna and a specific receive antenna, v is the frequency offset that needs to be estimated and n_k is the complex white Gaussian noise with variance N_o.

In general, there would be multiple receive antennas and each receive antenna would have a separate LO that would introduce some frequency drift; this means that frequency estimation needs to be done separately for each receive antenna. The frequency offset v could possibly be different for different sub-carriers because Doppler induced frequency shifts depend on the wavelength of the transmission. Data modulation can be removed by multiplying $r(k)$ with c_k^*, because for PSK constellations $c_k\, c_k^* = 1$ and the training sequence $z(k)$ is known(The training sequence symbols, taken from IEEE Standards 802.11n and 802.16, are assumed to be a Phase Shift Keying (PSK) constellation such as Quadrature Phase Shift Keying).

$$z(k) = r(k) \times c_k^* = h_m e^{j\left[2\pi vkT+q\right]} + n(k). \quad (2)$$

The autocorrelation of the $z(k)$ sequence is defined as:

$$R(p) \equiv \frac{1}{(N+1-p)} \sum_{k=p}^{N} z(k) z^*(k-p) \quad for\, 1 \le k, p \le N. \quad (3)$$

Substituting (2) in (3) we get the following expression for $R(p)$:

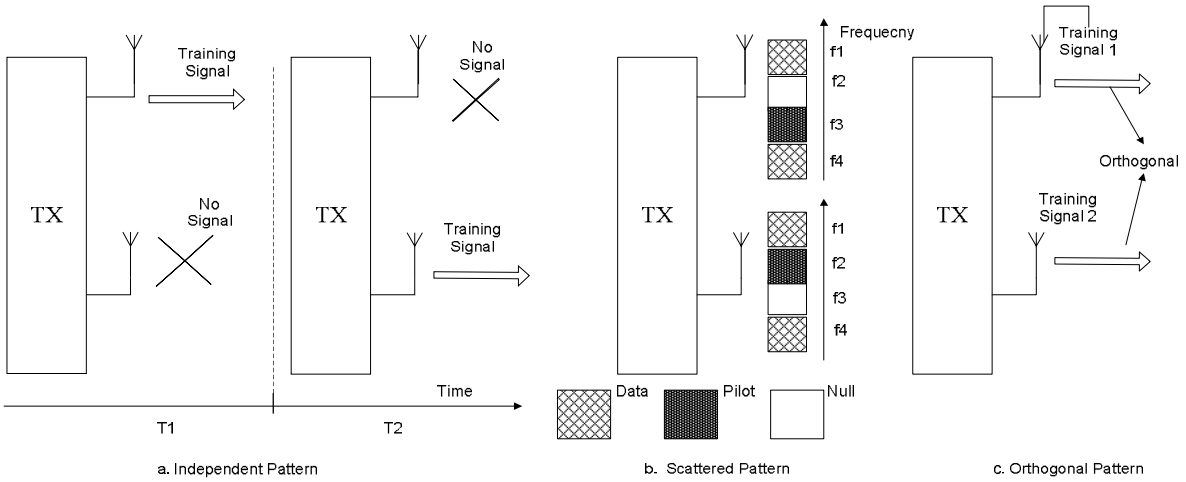

Figure 1. Three different patterns for transmitting training signals in MIMO-OFDM systems [9].

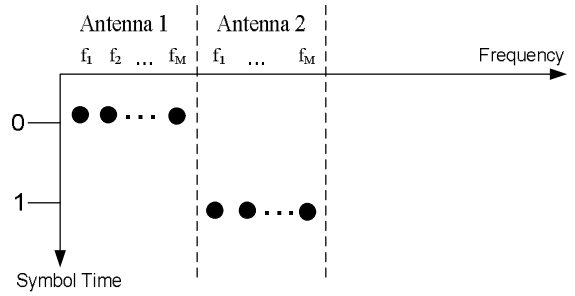

Figure 2. Space Time Encoding of the training sequence.

$$R(p) \equiv e^{j2p\,pvT} + n''(p), \tag{4}$$

where $|h_m|^2$ is normalized to be equal to 1 and $n''(p)$ represents the noise related(noise-noise and noise-signal) terms after substitution.

We can find a frequency offset estimate now using the formula of L&R given below:

$$\hat{v} = \frac{1}{p\,(N+1)T} \arg\left\{ \sum_{p=1}^{N} R(p) \right\}. \tag{5}$$

The summation of $R(p)$ in (3) serves to smooth out the noise as it is a moving average filter which is low pass and ideal for noise smoothing. In our MIMO-OFDM system we propose to go one step further and cross-correlate $R(p)$ with a training sequence transmitted from the second antenna in the next time slot with the same channel coefficient h_m as shown in **Figure 3**.The packet length is assumed to be longer than multiple time slots and the channel remains constant over a packet length.

The cross-correlations give a greater noise-averaging gain. For this case the term within the summation in Equation (3), $z(k)z^*(k\text{-}p)$ is replaced by auto correlations and cross- correlations of the symbol transmitted from first and second antenna, respectively:

$$\frac{1}{4}\begin{bmatrix} z(k)z^*(k-p) + z(l)z^*(l-p) + \\ z(k)z^*(l-p) + z(l)z^*(k-p) \end{bmatrix}. \tag{6}$$

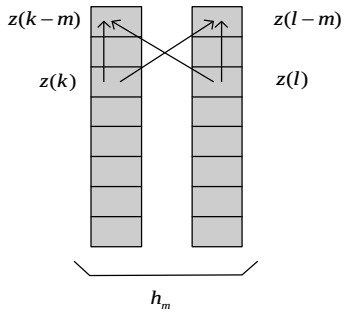

Figure 3. Auto and cross correlations of the training sequences of two transmit antennas.

For a general case of MIMO systems, N transmit antennas would results in N^2 terms in our proposed correlations.

4. Simulation Results

Here we explore the performance of proposed frequency offset estimator for multipath fading channels using Mean Square Error (MSE) as a performance metric. We have used SUI channel 1 and SUI channel 3 as multipath fading channel for our simulations. Initially we discuss the results of WLAN and then the results of WMAN will be discussed subsequently.

For WLAN we have used 5 GHz licensed band with nominal channel bandwidth of 20 MHz. The transmitted carrier frequency of both the base station and subscriber station should have accuracy better than $\pm 20 \times 10^{-6}$ as per IEEE Standards 802.11 n. The value should remain valid over a given temperature range and time of operation *i.e.*, ageing of equipment. Keeping aforementioned in view the maximum carrier frequency offset comes out to be 200 kHz. A packet size of 1KB is assumed. Unit delay of channel is assumed to be the same as OFDM sample period.

In **Figure 4** the original curves refer to estimating the frequency offset by taking autocorrelations of the $z(k)$ sequences whereas the modified curves refer to using auto and cross correlations of $z(k)$ and $z(l)$, respectively for SUI 1 channel. The curves in this figure are generated for the cases of two transmit antennas. The modified curves, as per the proposed algorithm, provide a $2 \times \log(N)$ dB noise averaging gain in AWGN conditions. However, in the presence of multipath fading, it is not possible to see the complete noise averaging gain, especially for

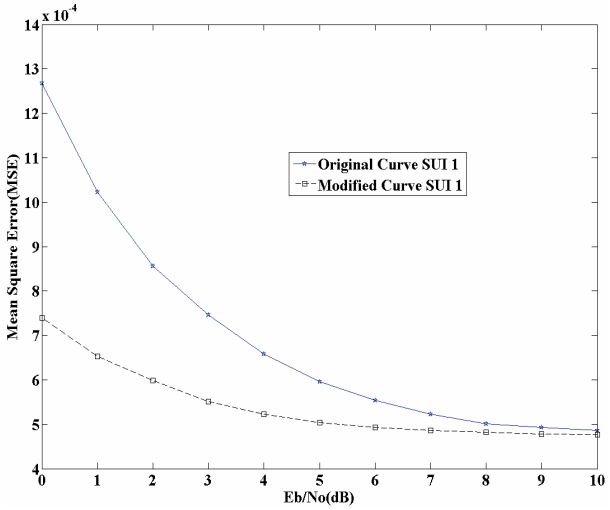

Figure 4. Performance of the proposed estimator for SUI 1 channel.

high E_b/N_0 values. This is because signal attenuation due to fades overshadows the effects of noise.

Similarly the performance of the proposed algorithm for MIMO-OFDM system for the case of SUI 3 channel is shown in **Figure 5** below. Same simulation parameters are used for both SUI 1and SUI 3 channel.

For WMAN We have used 3.5 GHz licensed band with nominal channel bandwidth of 3.5 MHz The transmitted carrier frequency of both the base station and subscriber station should have accuracy better than $\pm 10 \times 10^{-6}$ as per IEEE Standard 802.16 d and the maximum carrier frequency offset comes out to be 70 kHz. A packet size of 1 KB is assumed.

In **Figure 6** below the original curves refer to estimating the frequency offset by taking autocorrelations of the $z(k)$ sequences whereas the modified curves refer to using auto and cross correlations of $z(k)$ and $z(l)$, respectively for SUI 1 channel. The curves in this figure are generated for the cases of two transmit antennas.

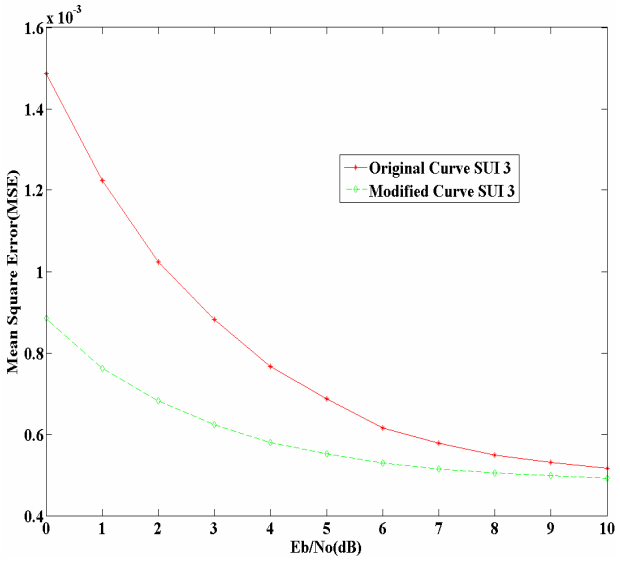

Figure 5. Performance of the proposed estimator for SUI 3 channel.

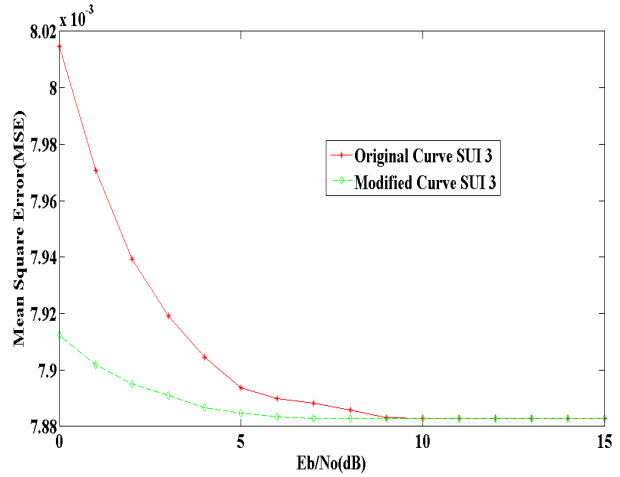

Figure 6. Performance of the proposed estimator for SUI 1 channel for WMAN.

Similarly the performance of the proposed algorithm for MIMO-OFDM system for the case of SUI 3 channel is shown in **Figure 7** below. Same simulation parameters are used for both SUI 1 and SUI 3 channels.

The salient aspects of the simulated results are analysed as under:-

1) The modified curves, as per the proposed algorithm, provide a $2 \times \log(N)$ dB noise averaging gain in AWGN conditions. However, in the presence of multipath fading, it is not possible to see the complete noise averaging gain, especially for high E_b/N_0 values. This is because signal attenuation due to fades overshadows the effects of noise.

2) It is quite evident that the modification suggested in this paper can reduce the MSE significantly for lower values of E_b/N_0. The complexity of the system may have increased but it may be traded-off for more accurate frequency offset estimation.

3) Performance of the proposed algorithm is dependent, apart from other factors, on the length of the training sequence. The training sequence used for WLAN is greater in length as compared to the training sequence of WMAN. Resultantly the results of WLAN are better as compared to WMAN especially for higher values of E_b/N_0.

4) Complete execution of the proposed algorithm requires the symbols transmitted in adjacent time slots to be received at the receiver.

5. Conclusions

In this paper an efficient frequency offset estimation

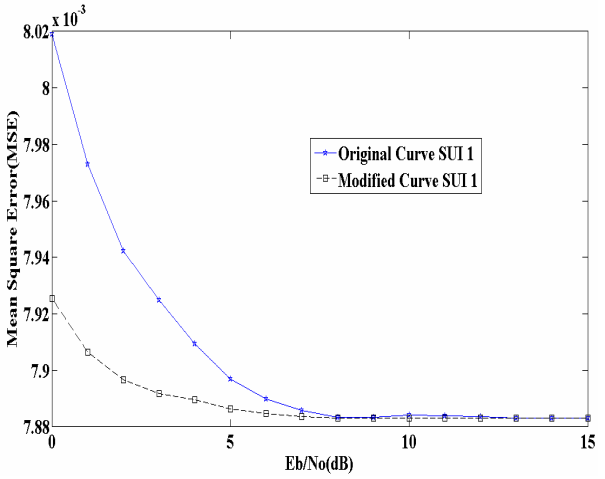

Figure 7. Performance of the proposed estimator for SUI 3 channel for WMAN.

technique for MIMO-OFDM systems in multipath environment is presented. Simulation results have shown that synchronization problems in MIMO-OFDM systems can be solved with proposed algorithm which gives good performance and tends to be limited only by multipath fading. Since our extension of the simple L & R estimator to the MIMO-OFDM case deals with data encoding and not with the final estimation step, we have preserved the optimality property of the L & R estimate.

6. References

[1] C. N. Kishore and V. U. Reddy, "A Frame Synchronization and Frequency Offset Estimation Algorithm for OFDM System and its Analysis," *EURASIP Journal on Wireless Communications and Networking*, Vol. 2006, 2006, pp. 1-16.

[2] T.-H. Kim and I.-C. Park, "Two Step Approach for Coarse Time Synchronization and Frequency Offset Estimation for IEEE 802.16d Systems," *IEEE Workshop on Signal Processing Systems*, Shanghai, 17-19 October 2007, pp. 193-198.

[3] L.-M. He, "Carrier Frequency Offset Estimation in MIMO OFDM Systems," 4*th IEEE Conference on WiCOM*, Dalian, 12-14 October 2008, pp. 1-4.

[4] Y. X. Jiang, X. H. You, X. Q. Gao and H. Minn, "Training Aided Frequency Offset Estimation for MIMO OFDM Systems via Polynomial Routing," 67*th IEEE Vehicular Technology Conference*, Singapore, 11-14 May 2008.

[5] M. K. Kiyani, M. U. Ahmed and A. Loan, "Synchronization in Fixed Broadband Wireless Access for Practical MIMO OFDM systems," 9*th IEEE Malaysian International Conference on Communications*, Kuala Lumpur, 15-17 December 2009.

[6] M. Luise and R. Reggiannini, "Carrier Frequency Recovery in All-Digital Modems for Burst-Mode Transmissions," *IEEE Transactions on Communications*, Vol. 43, No. 2-4, 1995, pp. 1169-1178.

[7] "IEEE P802.11n/D11.0 Draft Standard for Information Technology, Telecommunications and Information Exchange between Systems," *Local and Metropolitan Area Networks—Part* 11: *Wireless LAN Medium Access Control* (*MAC*) *and Physical Layer* (*PHY*) *Specifications*, 2009.

[8] K. V. Erceg, S. Hari, M. S. Smith, D. S. Baum, *et al*., "Channel Models for Fixed Wireless Applications," IEEE 802.16.3 Task Group Contributions, 1 February 2001.

[9] G. J. Andrews, A. Ghosh and R. Muhamed, "Fundamentals of WiMAX Understanding Broadband Wireless Networking," Prentice Hall Communications Engineering and Emerging Technologies Series, Prentice Hall, February, 2007.

Int. J. Communications, Network and System Sciences, **2010, 3, 488-493**
doi:10.4236/ijcns.2010.35066 Published Online May 2010 (http://www.SciRP.org/journal/ijcns/)

Scientific Research

A Cross Layer Optimization Based on Variable-Power AMC and ARQ for MIMO Systems

Shu-Ming Tseng, Wei-Shun Lei
Department of Electronic Engineering, National Taipei University of Technology, Taiwan, China
E-mail: *shuming@ntut.edu.tw, gavin_lei@unihancorp.com*
Received February 10, 2010; *revised March* 29, 2010; *accepted April* 27, 2010

Abstract

To improve spectrum efficiency (SE), the adaptive modulation and coding (AMC) and automatic repeat request (ARQ) scheme have been combined for MIMO systems. In this paper, we add variable power subject to power constraint in each AMC mode. We use KKT optimization algorithm to get the optimal transmit power and AMC mode boundaries. The numerical results show that the average SE is increased by about 0.5 bps/Hz for 2 × 2 MIMO systems with Nakagami fading with parameter m = 2 when SNR is around 15 dB and the ARQ retransmission is twice.

Keywords: Transmitter Power Control, Spectrum Efficiency

1. Introduction

The demand for high data rate and quality of service (QoS) in wireless networks requires cross layer approach [1]. The adaptive modulation and coding (AMC) are already considered for implementation in many wireless system standards. In order to improve the average spectrum efficiency (SE), a combining constant-power AMC scheme in physical layer and truncated automatic repeat request (ARQ) protocol which provides a trade-off between the average coding rate and the probability of undetected error at the data link layer (DLL) in single-input single-output (SISO) system [2].

In this paper, we add power adaptation proposed in [3] to the constant-power AMC and ARQ in MIMO systems in [4]. In the proposed adaptive-power AMC and ARQ in MIMO systems, the power can be changed to increase average SE. The packet error rate (PER) in [2,3] which is much smaller than the target PER, so we are motivated to increase the PER, make PER as close to the target PER as possible. In this way, the switching SNR level of each rate boundary of each rate shift left in the SNR axis and we move to higher mode earlier as using higher order modulation, or higher code rate and the average SE can be improved. However the leftmost part of one each SNR region can have PER exceed limit, so we need adaptive power to compensate it. In [4] the Lagrangian multipliers λ is only one. In the propose method, the Lagrangian multipliers λ is different according to each AMC mode.

Numerical results indicates that the proposed optimization algorithm which combine adaptive power AMC scheme at physical layer and truncated ARQ protocol at data link layer can increase the average SE.

This paper is organized as follows: Section 2 describes the system model. Section 3 presented our proposed scheme with adaptive power. Numerical results are presented in Section 4, and our conclusion is in Section 5.

2. System Model

We consider a SISO system which combining the AMC scheme with power control at the physical layer and the truncated ARQ module at the data link layer, as shown in **Figure 1**.

We assume channel gains remain invariant during a packet, but vary from packet to packet. Let R_n be the rate of the mode. $\overline{S}$ denotes the average transmit power, γ denotes the pre-adaptation received SNR which the receiver feed back to the transmitter, and $S_n(\gamma)$ denotes the allocated power in the AMC mode n. The AMC is performed by dividing the range of the channel SNR into N + 1 non-overlapping consecutive interval, denoted by $[\gamma_n, \gamma_{n+1}), n = 0,1,..., N,\quad \gamma_0 = -\infty,\quad \gamma_{N+1} = \infty$ and N is the number of AMC modes. No data is sent at $[\gamma_0, \gamma_1)$ SNR range which corresponds to the outage mode. Consider of power adaptation, we modify the PER expression in the mode n [2,3] as follows:

$$PER_n(\gamma)=\begin{cases}1, & 0\le\gamma<\gamma_{pn}\\ a_n\exp\left(-g_n\dfrac{S_n(\gamma)}{\bar{S}}\gamma\right), & \gamma\ge\gamma_{pn}\end{cases} \quad (1)$$

The mode dependent parameters $\{a_n, g_n, \gamma_{pn}\}$ are given in **Table 1**. The mode-switching SNR values in [2,3] (without power adaptation) can be found by assuming $S_n(\gamma)/\bar{S}=1$ and $PER_n(\gamma)=P_t$ where P_t is the target PER (0.01 usually) in (1). If considering adaptation power, we have two unknown elements, $S_n(\gamma)$ is the adaptive power inside the mode n and γ is the switching SNR to mode n. So we need to solve adaptive power under each mode first, then we can look for the mode-switching SNR values.

3. Adaptive-Power AMC

Because the AMC algorithm is the same for all SISO sub-channel, so we only discuss the AMC scheme with truncated ARQ protocol in the *i*th sub-channel in this section.

Here, we propose adaptive-power AMC to find the optimal SNR switching level that maximize SE under the PER constraint. The instantaneous PER is smaller than target PER, $PER_n^i(\gamma)\le P_t$, $\gamma_n^i\le\gamma\le\gamma_{n+1}^i$; $\forall n=1,...,N$, where P_t denotes the target PER, so average PER will lower than target PER, too. We now propose that, $PER_n^i(\gamma)=P_t$, and add power factor to make the average SE larger. From (1), we can find the power adaptation with PER constraint in mode n is

$$\frac{S_n^i(\gamma)}{\bar{S}}=\frac{1}{g_n\gamma}\ln\left(\frac{a_n}{P_t}\right)\quad \gamma_n^i\le\gamma\le\gamma_{n+1}^i \quad (2)$$

Using (2), we now have the PER constraint as follows

$$\frac{1}{g_n}\ln\left(\frac{a_n}{P_t}\right)\int_{\gamma_n^i}^{\gamma_{n+1}^i}\frac{1}{\gamma}p_\gamma(\gamma)d\gamma\le\Pr(n) \quad (3)$$

We want to find the close form of the above equation, so we first find the close form of the following: (difference from traditional, addition $1/\gamma$ factor)

$$\Pr_{pow}^i(n)\equiv\int_{\gamma_n^i}^{\gamma_{n+1}^i}\frac{1}{\gamma}p_\gamma(\gamma)d\gamma =\begin{cases}\dfrac{1}{\bar{\gamma}}\left(Ei\left(\dfrac{-\gamma_{n+1}^i}{\bar{\gamma}}\right)-Ei\left(\dfrac{-\gamma_n^i}{\bar{\gamma}}\right)\right), & m=1\\ \dfrac{m}{\bar{\gamma}}\left(\dfrac{\Gamma\left(m,\dfrac{m\gamma_n^i}{\bar{\gamma}}\right)-\Gamma\left(m,\dfrac{m\gamma_{n+1}^i}{\bar{\gamma}}\right)}{\Gamma(m)}\right), & m\ge2\end{cases} \quad (4)$$

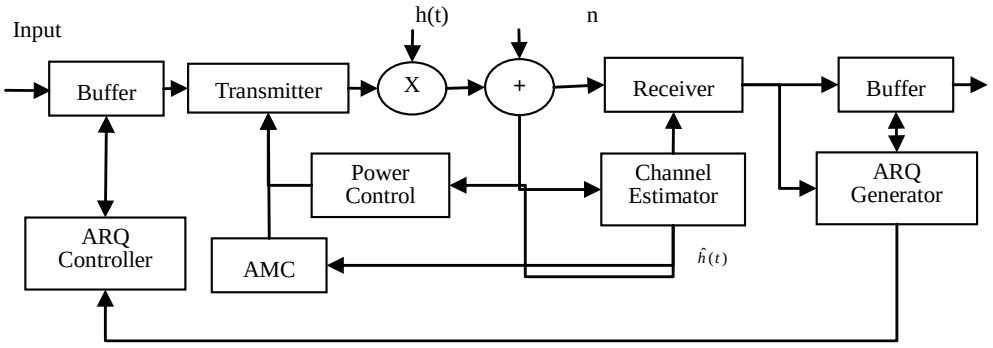

Figure 1. System model.

Table 1. Transmission modes in TM2 AMC scheme with convolutional coded M-QAM modulation.

	Mode 1	**Mode 2**	**Mode 3**	**Mode 4**	**Mode 5**	**Mode 6**
Modulation	BPSK	QPSK	QPSK	16-QAM	16-QAM	64-QAM
Coding rate	1/2	1/2	3/4	9/16	3/4	3/4
R_n **(bit/sym.)**	0.5	1	1.5	2.25	3	4.5
a_n	274.72	90.25	67.62	50.122	53.399	35.351
g_n	7.9932	3.4998	1.6883	0.6644	0.3756	0.09
γ_{pn} **(dB)**	-1.533	1.094	3.972	7.702	10.249	15.978
Con-Power	1.0677	4.1537	7.1797	11.0799	13.5891	19.5801
Adapt-Power	-1.2437	1.6448	5.8601	9.5942	11.9965	16.8863

when $Ei(x) = -\int_{-x}^{\infty} e^{-t}/tdt$ is the exponential integral function, and has no close form. The optimization program can be formulated as

$$\begin{aligned} &\text{Maximize} \quad \sum_{n=1}^{N} R_n \Pr(n) \\ &\textit{subject to} \quad \sum_{n=1}^{N} \frac{1}{g_n} \ln\left(\frac{a_n}{P_t}\right) * \Pr_{pow}^{i}(n) \le \sum_{n=1}^{N} \Pr(n) \end{aligned} \tag{5}$$

The constraint in (5) is from (3) and (4). Using the KKT solution to solve , we got that:

$$\begin{aligned} &L(\gamma_1^i, \ldots, \gamma_n^i, \lambda) = \\ &\sum_{n=1}^{N} R_n \Pr(n) + \left(\sum_{n=1}^{N} \frac{1}{g_n} \ln\left(\frac{a_n}{P_t}\right) \lambda_n \left(\Pr_{pow}^{i}(n) - \Pr(n)\right)\right. \end{aligned} \tag{6}$$

where λ are the Lagrangian multipliers. The optimal solution $(\gamma_1^{i*}, \gamma_2^{i*}, ..., \gamma_N^{i*})$ and the corresponding Lagrangian multipliers, λ_n^* must satisfy the following conditions:

1) $\dfrac{\partial L}{\partial \gamma_n}(\gamma_1^{i*}, \ldots, \gamma_n^{i*}, \lambda_1^*, ..., \lambda_N^*) = 0, n = 1, 2, \ldots, N$

2) $\sum_{n=1}^{N} \frac{1}{g_n} \ln\left(\frac{a_n}{P_t}\right) \Pr_{pow}^{i}(n) \le \sum_{n=1}^{N} \Pr(n)$

3) $\sum_{n=1}^{N} \int_{\gamma_N^i}^{\gamma_{N+1}^i} S_n^i(\gamma) p_\gamma(\gamma) d\gamma \le \bar{S}$

4) $\lambda_n^* \le 0$

5) $\gamma_n^{i*} \ge \gamma_{pn}, n = 1, 2, \ldots, N$ (7)

so that he optimal SNR switching level, $(\gamma_1^{i*}, \gamma_2^{i*}, ..., \gamma_N^{i*})$ will larger than the bound point constraint, γ_{pn}. The general form of the optimal mode switching levels can be written as

$$\begin{aligned} &\gamma_1^{i*} = -\frac{\ln(a_1 / P_1)}{g_1(\lambda_1^* - R_1)} \lambda_1^*, \\ &\gamma_n^{i*} = -\frac{\lambda_{n-1}^* g_n \ln(a_{n-1} / P_1) - \lambda_n^* g_{n-1} \ln(a_n / P_1)}{g_n g_{n-1}(R_n - R_{n-1} + \lambda_n^* - \lambda_{n-1}^*)}, n = 2, ..., N \end{aligned} \tag{8}$$

we have the optimal mode switching levels, checking the switching levels, $(\gamma_1^{i*}, \gamma_2^{i*}, ..., \gamma_N^{i*})$ satisfy the constraint in (5), and the optimal mode switching levels. Finally, the proposed algorithm is summarized in **Figure 2**.

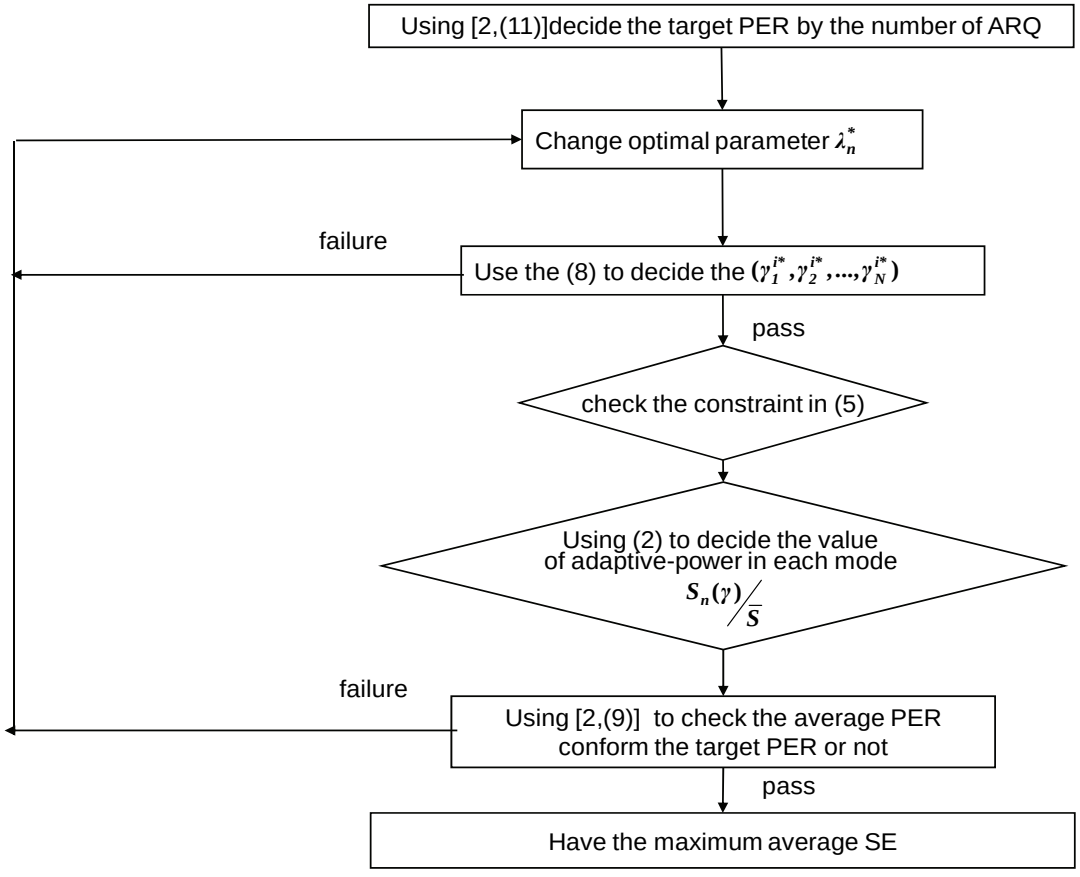

Figure 2. Flowchart.

4. Numerical Results

Here, we present numerical results for average spectral efficiency, power adaptation and PER using the optimal solution. We find the constraint in (5) when Nakagami channel $m = 1$ is a special case that $Ei(x)$ in (4) has no close-form and can't give the value of constraint in (5). So we use Nakagami channel fading parameter with m = 2 instead. We use the parameters of AMC scheme that is listed in **Table 1** from [5]. In **Figure 3**, we can see power switching in each mode and the leftmost power in each AMC mode is largest that make the average PER to conform PER constraint in each AMC mode. **Figure 2** shows the flowchart of optimal search algorithm. We use a Nakagami fading with parameter $m = 2$ 2 × 2 MIMO channel model, and assume a target PLR of $P_{loss} = 0.01$. In **Figure 4**, depict the average spectral efficiency for TM2 AMC scheme in **Table 1**, and we observed that using the truncated ARQ protocol helps increase the system SE ($N_{ARQ} = 2$ vs. $N_{ARQ} = 0$). Also in **Figure 4**, we can observe that our proposed scheme SE of $N_r = 0$ has a significant SE improvement over the one of $N_{ARQ} = 2$ in [2].

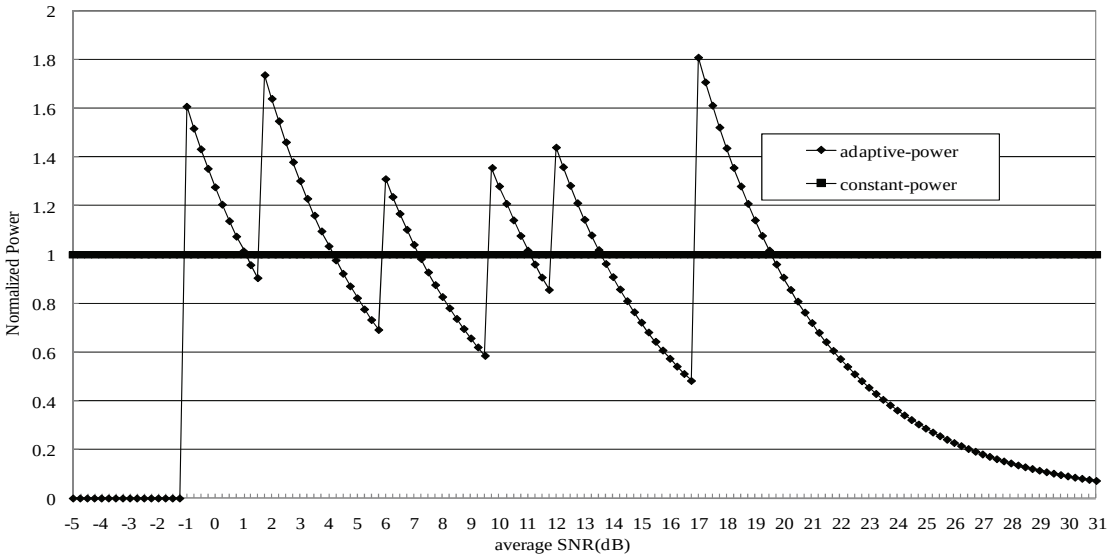

Figure 3. Adaptive power in each mode for Table 1 AMC scheme for sub-channel, target PER = 0.01.

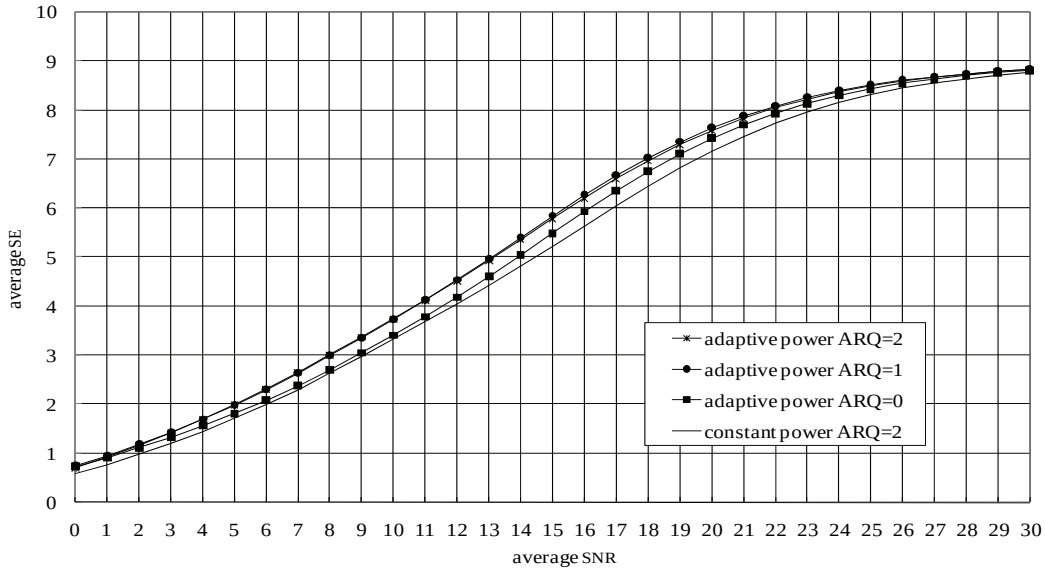

Figure 4. Table 1 AMC scheme 2 × 2 MIMO channel, target PER = 0.01.

But the maximum N_{ARQ} not always bring the best average SE, $11 \le SNR \le 21$ in **Figure 4**, we can see the average SE in 2 × 2 MIMO channel at N_{ARQ} = 2 is smaller than N_{ARQ} = 1. Because increasing N_{ARQ}, we alleviate the error bound to improve the average SE, but retransmission the same packet too many times will also degrade the average SE, so we try to balance N_r with target PER, such as $N_{ARQ} = 1$ in $P_t = 0.01$, and have the maximum average SE in our proposed system.

In **Figure 5**, we show the different combinations of two sub-channel for different SNRs in bar diagrams to the ARQ. We consider these 8 combinations and map them to integer numbers on x-axis [3]:

{1=(c_1=0,c_2=0),2=(c_1=1,c_2=1),3=(c_1=2,c_2=1)
4=(c_1=1,c_2=2),5=(c_1=2,c_2=2),6=(c_1=3,c_2=2)
7=(c_1=2,c_2=3),8=(c_1=3,c_2=3)}

where c_i is the i sub-channel.

In **Figure 5**, we can see the case 2 which have better SE than the other cases. This is consistent with the conclusions of the **Figure 4**.

Figure 6 compares the PER in [2] and the PER of our proposed scheme. We can see we increase the PER to the maximum (target PER = 0.01) at the left most of the SNR axis.

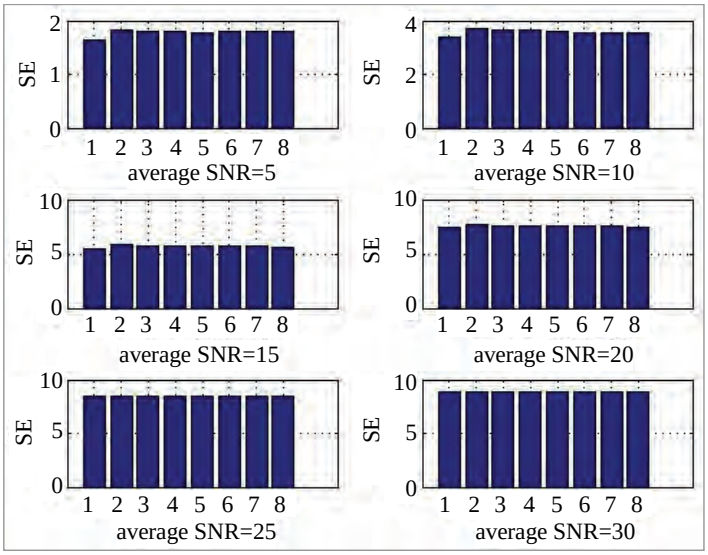

Figure 5. Different combinations of two sub-channel for different average SNRs.

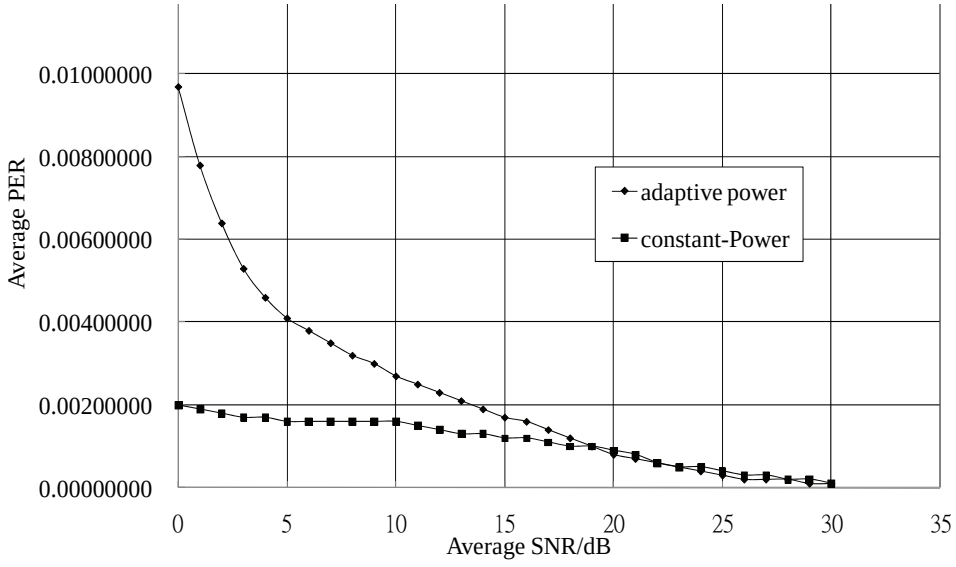

Figure 6. PER for Table 1 AMC scheme with adaptive power.

5. Conclusions

In this paper, we considered optimized rate and power adaptation at the physical layer aiming at maximizing the average SE, while satisfying a target PER constraint at the data link layer in MIMO channel. We proposed that increasing the PER makes it approach PER constraint, and the optimal mode switching level of each rate will shift to the left in the SNR axis, so we can use the higher order modulation to improve the average SE. The numerical results shows that the adaptation power within each SNR mode can improve the average spectrum efficiency by 0.4 ~ 0.7 (bits/symbol) in mid-SNR range for 2 × 2 MIMO systems, and ARQ $N_{ARQ} = 1$ is optimal for target PER = 0.01 to have the maximum average SE. We also show that each transmit antenna can have different maximum retransmission number due to independence of the sub-channels.

6. Acknowledgements

This work was presented in part in International Conference on Advanced Information Technologies (AIT2010), Taichung County, Taiwan, 23-24 April 2010. This work was supported in part by National Science Council, Taiwan, under Grant NSC 98-2221-E-027-038-MY2.

7. References

[1] X. Zhang, J. Tang, H. H. Chen, S. Ci and M. Guizani, "Cross-Layer-Based Modeling for Quality of Service Guarantees in Mobile Wireless Networks," *IEEE Communications Magazine*, Vol. 44, No. 1, January 2006, pp. 100-106.

[2] Q. Liu, S. Zhou and G. B. Giannakis, "Cross-Layer Combining of Adaptive Modulation and Coding with Truncated ARQ over Wireless Links," *IEEE Transactions on Wireless Communications*, Vol. 3, No. 5, September 2004, pp. 1746-1755.

[3] J. S. Harsini and F. Lahouti, "Optimized Link Adaptation for Wireless Packet Communications Based on Discrete-Rate Modulation and Coding Schemes," *IEEE Workshop Signal Processing Advances in Wireless Communications*, Helsinki, June 2007, pp. 17-20.

[4] A. Jafari and A. Mohammadi, "A Cross Layer Approach Based on Adaptive Modulation and Truncated ARQ for MIMO Systems," *Processing IEEE International Conference on Telecommunications and Malaysia International Conference on Communications*, Penang, May 2007, pp. 260-265.

[5] A. Doufexi, S. Armour, M. Butler, A. Nix, D. Bull, J. McGeehan and P. Karlsson, "A Comparison of The HIPERLAN/2 & IEEE 802.11a Wireless LAN Standards," *IEEE Communications Magazine*, Vol. 40, No. 5, May 2002, pp. 172-180.

Call for Papers

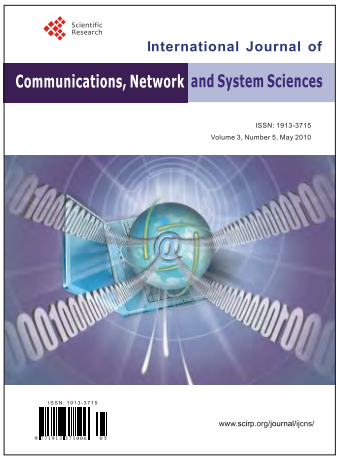

International Journal of

Communications, Network and System Sciences (IJCNS)

ISSN 1913-3715 (Print) ISSN 1913-3723 (Online)

http://www.scirp.org/journal/ijcns/

IJCNS is an international refereed journal dedicated to the latest advancement of communications and network technologies. The goal of this journal is to keep a record of the state-of-the-art research and promote the research work in these fast moving areas.

Editors-in-Chief

Prof. Huaibei Zhou	Wuhan University, China

Subject Coverage

This journal invites original research and review papers that address the following issues in wireless communications and networks. Topics of interest include, but are not limited to:

MIMO and OFDM technologies	Sensor networks
UWB technologies	Ad Hoc and mesh networks
Wave propagation and antenna design	Network protocol, QoS and congestion control
Signal processing and channel modeling	Efficient MAC and resource management protocols
Coding, detection and modulation	Simulation and optimization tools
3G and 4G technologies	Network security

We are also interested in:

- Short reports—Discussion corner of the journal:
  2-5 page papers where an author can either present an idea with theoretical background but has not yet completed the research needed for a complete paper or preliminary data.
- Book reviews—Comments and critiques.

Notes for Intending Authors

Submitted papers should not have been previously published nor be currently under consideration for publication elsewhere. Paper submission will be handled electronically through the website. All papers are refereed through a peer review process. For more details about the submissions, please access the website.

Website and E-Mail

http://www.scirp.org/journal/ijcns ijcns@scirp.org

Int. J. Communications, Network and System Sciences, **2010, 3, 425-493**
Published Online May 2010 in SciRes (http://www.SciRP.org/journal/ijcns/).

TABLE OF CONTENTS

Volume 3 Number 5 **May 2010**

